Fracture and Toughening of Brittle Structures with Designed Anisotropy

Thesis by
Neal Ryan Brodnik

In Partial Fulfillment of the Requirements for the
Degree of
Philosopher's Doctorate in Materials Science

CALIFORNIA INSTITUTE OF TECHNOLOGY
Pasadena, California

2020
Defended August 26, 2019

Neal Ryan Brodnik
ORCID: 0000-0002-4426-5997

ACKNOWLEDGEMENTS

First, I want to thank my advisers, Kathy Faber and Ravi Ravichandran, not only for their advice and assistance with this thesis work, but also for helping me grow as a researcher and scholar. I would also like to thank Kaushik Bhattacharya and Blaise Bourdin, who provided critical advice and knowledge, particularly with many of the theoretical and numerical aspects of this work. Furthermore, this thesis, like many multidisciplinary efforts, would not have been possible without the contributions of many collaborators and supporters. I would like to thank Chun-Jen Hsueh for his help with the powder grid method as well as his computational and experimental assistance in the characterization of polymer composites with variable thickness inclusions. I would also like to thank Tzu-Chieh Chou and Yu-Chong Tai for their assistance with silicon wafer fabrication for the powder grid method. I would also like to thank Stella Brach for her computational support in the design and analysis of fracture diodes. Additionally, I would like to thank Johanna Schmidt and Paolo Colombo for their help with the fabrication and testing of preceramic polymer trusses. I would also like to extend a thank you to our industry collaborators at HRL Laboratories, who provided great advice and assistance in understanding the printing and pyrolysis of photocurable siloxane resins. In addition this thesis was further assisted by several undergraduate students: Tim Ekeh, Guillaume de Luca, and Christopher Long, whose work across multiple projects was of great insight. Finally, I would like to give a particularly special thank you to Matt Johnson, who provided crucial assistance to almost every aspect of this thesis in the form of refinement of ideas, development of techniques, and implementation of experimental methods.

I gratefully acknowledge the financial support of the U.S. National Science Foundation Award No. DMS-1535083 under the Designing Materials to Revolutionize and Engineer our Future (DMREF) Program. Additionally, the development of the numerical codes used as part of this project was supported in part by a grant from the National Science Foundation DMS-1716763. Numerical simulations were performed at the Caltech high performance cluster supported in part by the Moore Foundation. Support for T. Ekeh was provided by the Caltech-Cambridge University Exchange Program. Finally, additional funding for collaboration with J. Schmidt was provided by the CARIPARO Foundation, Padova, Italy.

I would like to give my personal thanks to everyone in the Faber and Ravichandran Labs for their advice and support throughout my five years at Caltech. Also, I

thank the administrative staff in the Mechanical Engineering and Materials Science departments at Caltech, who have helped me through numerous logistical problems that I would not have been able to address on my own. I would also like to thank my fiancée, Christina, for her love and support through the many rough patches that come with pursuing a PhD. Finally, I would like to thank my parents, who have always encouraged me to challenge myself as much as I can, and particularly my father, who whose support and encouragement fostered the love for science that drives me today.

ABSTRACT

Despite good thermal and chemical properties, the use of ceramic materials in structural applications is limited by their inherently brittle nature. Efforts have been made to improve the toughness of ceramics through composite design, but recent developments in net shape processing such as additive manufacturing have significantly expanded this design space. Where composite topologies and morphologies were previously limited by material composition and thermodynamics, tools like 3D printing now allow for the design of composite structures of nearly any shape or arrangement.

This work seeks to understand how these processing advances might be utilized to improve the toughness of brittle composites by exploring how previously inaccessible anisotropic inclusion structures might influence fracture behavior. The study begins with the evaluation of printed photopolymer structures as model brittle materials. First, printed structures are used to explore how elastic contrast between inclusions and matrix can affect crack propagation and improve toughness. Here, anisotropy presents an opportunity to achieve similar toughness to isotropic structures at smaller volume fractions by virtue of topologies that only exhibit toughening only in a singular direction, but require significantly less material to do so. Next, the effect of anisotropic voids is explored as a means of controlling crack nucleation and growth. With consideration of both compliance and directional propagation, a "fracture diode" that exhibits controlled, predictable fracture 100% of the time can be realized.

After exploring brittle polymers, ceramics systems with similar toughness and higher stiffness are considered. First, a model layered system of mica is explored, where wedge splitting can be used achieve stable crack growth. This allows for the evaluation of how changes in compliance can improve the interlayer toughness without directly interacting with the crack. Finally, this study extends further into ceramics by exploring silicon oxycarbide (SiOC) truss structures and truss elements produced from 3D printed preceramic polymers. In addition to considering the material itself, changes in truss structure are explored as a means of changing deformation mode, and by consequence, failure strength. These model experiments suggest that if trusses are compatible, they can be interchanged to control failure of the bulk structure.

This study demonstrates how designed heterogeneities with anisotropic structure can be used to both enhance the toughness of brittle composites as well achieve a greater

degree of control over both crack nucleation and propagation in brittle systems where predicting failure is otherwise difficult. Looking forward, new processing tools like additive manufacturing present major opportunities for expanding the design space of brittle composites to achieve higher toughness and better fracture control than previously available. These new techniques may be able to expand the mechanical viability of ceramics, and make them better suited to mechanically demanding applications in the future.

PUBLISHED CONTENT AND CONTRIBUTIONS

For [1], N.R. Brodnik provided the development of the grid deposition method, and the fabrication of the grids and specimens for characterization. For [2], N. R. Brodnik contributed to the conception of the project, the design of the test methods, and the analysis of the mechanical testing data. For [3], N.R. Brodnik was responsible for the design, fabrication, and characterization of all printed photopolymer specimens as well as the analysis of the experimental results. For [4], N.R. Brodnik contributed to specimen design as well as the mechanical characterization and data analysis. For [5], N.R. Brodnik was responsible for the specimen design and fabrication as well as a portion of the analysis of experimental results. For [6], N.R. Brodnik performed all experimental design, specimen fabrication, mechanical testing, and data analysis.

[1] N. R. Brodnik, C. J. Hsueh, and M. T. Johnson. A nonconstraining templated powder grid for measurement of strain. *Strain*, 2018. ISSN 14751305. doi: 10.1111/str.12273.

[2] M.T. Johnson, N.R. Brodnik, T. Ekeh, K. Bhattacharya, and K.T. Faber. Obreimoff revisited: Controlled heterogeneous fracture through the splitting of mica. *Mechanics of Materials*, 136:103088, sep 2019. ISSN 0167-6636. doi: 10.1016/J.MECHMAT.2019.103088. URL https://www.sciencedirect.com/science/article/pii/S0167663618307543?dgcid=author.

[3] N. R. Brodnik, S. Brach, K. Bhattacharya, B. Bourdin, K.T. Faber, and G. Ravichandran. Fracture diodes: Directional asymmetry of fracture toughness. *In Preparation*, 2019.

[4] N. R. Brodnik, J. Schmidt, P. Colombo, and K.T. Faber. Analysis of multi-scale mechanical properties of ceramic trusses prepared from preceramic polymers. *Submitted to Additive Manufacturing*, 2019.

[5] N. R. Brodnik, C.-J. Hsueh, K. Bhattacharya, B. Bourdin, K.T. Faber, and G. Ravichandran. Guiding and trapping cracks with compliant inclusions for enhancing toughness of brittle composite materials. *Submitted to Journal of Applied Mechanics*, 2019.

[6] N.R. Brodnik and K.T. Faber. Out-of-plane mechanical characterization of acicular mullite and aluminum titanate diesel particulate filters. *International Journal of Applied Ceramic Technology*, 16(3):1173–1183, may 2019. ISSN 17447402. doi: 10.1111/ijac.13161.

TABLE OF CONTENTS

LIST OF ILLUSTRATIONS

LIST OF TABLES

Chapter 1

INTRODUCTION AND BACKGROUND

1.1 Motivation

The main focus of this work, in the broadest sense, is the improvement of the mechanical properties of brittle systems, particularly ceramics. Many ceramic systems have a great deal of potential in numerous industrial applications because of their high thermal and chemical stability. Thermal stability provides such great benefit because it allows for higher engine operating temperatures, which improves engine efficiency and reduces operating costs. This is useful not only in transportation applications, but also in power generation. Even in a well developed country like the United States, 37% of annual energy production still comes from petroleum and another 29% from natural gas, so improving the efficiency of the engines that produce this power would provide significant benefit in terms of cost reduction and output improvement.[1] The chemical stability of ceramics is also a major consideration, as they offer significantly better corrosion resistance than most structural metals and alloys. This corrosion resistance is major benefit, both in the context of operating life as well as cost. The National Association of Corrosion Engineers estimates that the annual global cost of corrosion is around 2.5 trillion US dollars, so any improvements to corrosion resistance that can be made through the implementation of ceramic components would provide significant benefits.[2]

Ceramics offer promising thermal and chemical resilience, but their widespread incorporation into technical applications has long been limited by their mechanical properties, namely a combination of low toughness and high stiffness. Low toughness means that it takes less mechanical energy to propagate a crack through a ceramic than it would through a higher toughness material, such as most metals. This problem is further exacerbated by high stiffness, which means that there is significantly greater elastic energy buildup for a given applied strain. This combination of large energy buildup and poor energy dissipation means that ceramics tend to fail catastrophically and unstably, especially when compared to more ductile metals. This limits not only the potential applications of ceramics, but also the available processing techniques, as conventional shaping techniques like machining cannot easily be used on materials that fracture so readily. Recently however, additional processing techniques have

been developed that allow for a greater degree of control over the fabrication of many different materials including ceramics. These processes, now known as additive manufacturing, allow for the fabrication of polymers, metals, and ceramics in a wide array of designs and structures. Because additive manufacturing uses element-by-element construction to produce physical recreations of digital designs, it is possible to create effectively any structure of arbitrary shape. This intersection of brittle systems and additive manufacturing is the focus of this thesis study. The objective of this work is to gain a better understanding of how the design freedom afforded by additive manufacturing might be used to improve the toughness of brittle systems through the implementation of designed composite structures, particularly ones with anisotropic design. Anisotropic design in particular has the potential to produce highly directional toughness behavior that would not be achievable with more traditional composite structures.

1.2 Fundamentals of Brittle Fracture

Griffith Theory

In order to understand the influence of composite structure on fracture properties, it is first critical to understand the fundamentals of fracture, particularly the energetics of fracture. The fundamentals of fracture were first described from an energetic standpoint by A.A. Griffith in 1921.[3] The premise of this work has become the basis of what is now referred to as the Griffith theory of fracture, and it centers on the idea of describing failure of material from the standpoint of thermodynamic equilibrium. In Griffith theory, a continuous, homogeneous, body containing a single crack of length 2C is subject to a far field load, as shown in Figure 1.1.

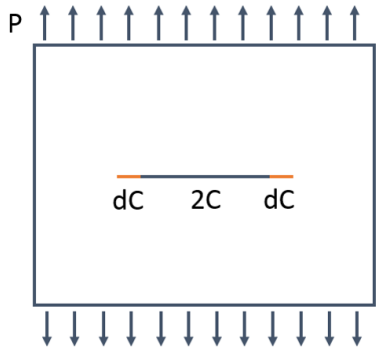

Figure 1.1: Schematic of the loading configuration used by Griffith to quantify the energetics of fracture.

For this scenario, the total energy in the system U can be broken into a sum of the

mechanical energy U_M and the surface energy U_S.

$$U = U_S + U_M \tag{1.1}$$

The surface energy is the energy associated with the formation of new surfaces due to the formation and propagation of the crack in the body. The mechanical energy is comprised of the elastic energy in the body due to the applied load U_E as well as the energy from the applied load itself U_A.

$$U_M = U_E + U_A \tag{1.2}$$

A combination of linear elastic fracture mechanics and simple potential energy arguments can readily quantify both U_E and U_A.

$$U_E = \frac{1}{2}P\delta \tag{1.3}$$

$$U_A = -P\delta \tag{1.4}$$

$$U_A = -2U_E \tag{1.5}$$

Here, P is the applied far-field load, and δ is the displacement of the body as it deforms due to the applied load. From this point, an application of the Inglis solution for the stress and strain fields in the volume elements around the crack, and integration over the body extending well beyond the crack can produce the following solution for U_M.[4]

$$U_M = \frac{-\pi C^2 \sigma^2}{E'} \tag{1.6}$$

In this solution, C is the half length of the crack, σ is the far field applied stress, and E' is E for the plane stress condition and $E/(1-\nu)$ for the plane strain condition, where E is the elastic modulus of the solid body and ν is Poisson's ratio.[5]

In this same manner, the surface energy can also be quantified in terms of material and geometric parameters, though in this case the quantification is more straightforward. For a body of unit width, the energy due to surface formation U_S can be described using the following equation

$$U_S = 2\,(2C\gamma) = 4C\gamma \tag{1.7}$$

where γ is the free energy of surface formation for the solid body. Reincorporating these into Equation 1.1 produces a complete description of the energy in the system.[5, 6]

$$U = 4C\gamma - \frac{\pi C^2 \sigma^2}{E'} \tag{1.8}$$

Finally, once the energy of the system has been described, the condition for equilibrium is set as $\frac{dU}{dC} = 0$. Differentiating and solving describes the stress at which propagation occurs in terms of the system geometry and properties of the body. This formulation became the basis off which fracture mechanics and the concept of fracture toughness were established.

Stress Intensity Factor

Griffith's description fracture toughness provides a good starting point for homogeneous, isotropic, uniform solids, but it is far from a complete description of the mechanisms of failure within a solid. An alternate description involves the concept of stress intensity factors, which are material prefactors in the stress functions that satisfy the bi-harmonic equation, which is a fourth order differential equation that accounts for the equilibrium conditions of failure, the constraints of Hooke's law, and strain compatibility.[5, 7, 8] These stress intensity factors, which have units of MPa$\sqrt{\text{m}}$, not only depend on the material being fractured, but also the loading conditions under which it failing. There are three different types of loading behavior that are labeled Mode I, Mode II, and Mode III. Mode I is in-plane opening, Mode II is in-plane shear, and Mode III is out-of-plane shear. Diagrams of each of these modes are shown in Figure 1.2

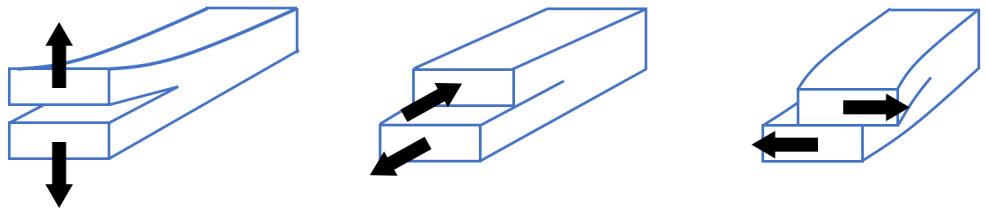

(a) Mode I (b) Mode II (c) Mode III

Figure 1.2: Schematics of the possible loading modes for failure by fracture.

Using this nomenclature, the stress field around a crack under far field loading can be described using the form[5]

$$\sigma = \frac{\text{K}_\text{M}}{(2\pi\text{r})^{\frac{1}{2}}} f(\theta) \tag{1.9}$$

where K_M is the stress intensity factor in Mode M, with M being either I, II, or III, r is the distance from the crack tip, and $f(\theta)$ is a directional cosine function that changes depending on the stress state and coordinate system. This stress intensity

factor is not only used to describe the stress state around a crack, but it is also a good method of establishing criteria for material failure. When a far field load is applied, the stress intensity factor increases, and when it exceeds some critical stress intensity factor K_C, the material will fail. This critical stress intensity factor is often referred to as fracture toughness, and it is both mode dependent, and is considered to be a property of the material system. The lowest toughness failure mode is Mode I, so K_{IC} is often used as a reference for the toughness of the material. Quantitatively, fracture toughness magnitudes give a fairly clear picture of why ceramics and other brittle systems are not as mechanically robust as many metal systems. The fracture toughness of a typical ceramic is in the range of 1-10 MPa$\sqrt{\text{m}}$, whereas the toughness of most ductile metals is in range of hundreds of MPa$\sqrt{\text{m}}$.

Nonlinear Behavior

Even with stress intensity factors, however, the description of behavior around the very tip of the crack is not straightforward to describe. This becomes apparent if one considers the form of Equation 1.9. Regardless of the value of $f(\theta)$, the magnitude of the stress rises to an infinite singularity at the tip of the crack as r approaches 0. This singularity is not a true physical singularity, but rather arises from the fact that the Irwin stress function solutions rely on linear elastic fracture mechanics, and the tip of the crack behaves nonlinearly. This nonlinearity has been addressed in different ways depending on the nature of the material being fractured. The most common approaches to addressing this are the Dugdale model and the Barenblatt model. The Dugdale model, which is most commonly used for metals and ductile systems, describes the region around the tip of the crack as a yield zone containing significant plastic deformation.[9] The Barenblatt model, which is used more commonly to describe ceramics, treats the region near the crack tip as a region of stretched atomic bonds spanning a few nanometers, and these stretched bonds apply a compressive force that slightly closes the tip of the crack, changing its shape.[10] The difference between these two models further emphasizes the disparity in toughness between metals and ceramics, as the energy dissipation from plastic formation is significantly larger than that from the separation of bonds in the cohesive zone, which further elaborates why ductile metals tend to be significantly tougher than ceramics and why additional methods of toughening ceramics through composite structures are so desirable.

J-Integral

To more completely describe the energetics of fracture in a manner that can account for both the linear elastic behavior further from the crack tip as well as the nonlinear behavior closer to the tip of the crack, J. Rice developed an integration method for evaluation of toughness from an energetic standpoint.[11] This integral, known as the J-integral, does not describe fracture toughness in the manner previously discussed, but rather describes the release rate of mechanical energy in the system due to propagation of the crack. The J-integral is shown the equation[5, 11]

$$J = -\frac{dU_M}{dC} = \int \mathcal{U} dy - \overline{T} \bullet \left(\frac{d\overline{u}}{dx}\right) ds \tag{1.10}$$

where $\mathcal{U}$ is the strain energy density, y is direction of the far field load, $\overline{T}$ is the traction vector on the curve defined in relation to the outward normal vector, $\overline{u}$ is the displacement vector, x is the direction of crack growth, and s is the contour around the crack. Although the faces of the crack itself are traction free, the value of the

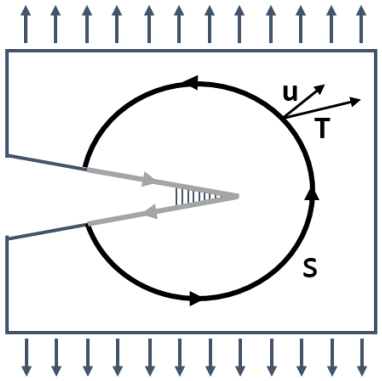

Figure 1.3: Schematic of J-integral contour around the crack tip.

J-integral with respect to the nonlinearity of the crack tip depends on the region of the solid body over which the contour is taking with respect to the tip of the crack. If the J-integral contour is taken in the near vicinity of the crack tip, it will capture the influence of the cohesion zone or plasticity zone, depending on the material system.[5] In this way, the J-integral is able to capture either the linear or nonlinear behavior of the crack, depending on its location. This contour integral can also be manipulated algebraically to create an area integral, with the only additional constraint being that the integral must be over a domain with a Lipschitz boundary.[11] As previously mentioned, this J-integral provides an energetic description of toughness, but relationships again developed by Irwin can relate this energetic description to the

critical stress intensity factors previously discussed.[7]

$$J = \mathcal{G}_C = \frac{(K_C)^2}{E'} \tag{1.11}$$

Here, E' is E for the plane stress condition and $E/(1-\nu)$ for the plane strain condition. With the use of this J-integral, a complete description of toughness can be obtained for any brittle system, even those with heterogeneous composite structures.

1.3 Composite Toughening Mechanisms for Brittle Solids

With clearly establish methods for measuring and describing the toughness of a material or composite system, it is important to understand how that toughness can be affected and increased, especially for brittle systems. In the context of microstructure, toughening mechanisms can be broken into two groups: those that toughen by changing the direction or geometry of the crack, and those that toughen by shielding the crack through interactions either in front of the crack tip or in the crack wake.[5]

Toughening by Crack Deflection

Geometric toughening effects can come in several forms, but one of the most common forms is found in the fracture of brittle polycrystalline materials. Because grain boundaries have higher energies that vary based on the orientation mismatch of the grains on either side of the boundary, it is often energetically favorable for a crack to travel at different angles along grain boundaries to take advantage of these higher energy domains. The result of this is that, depending on the orientation of loading, the crack may either twist out-of-plane or deflect in-plane to fracture in the most energetically favorable manner based on the arrangement of crystals in the material. This effect has been seen in numerous crystalline ceramics materials as including structural ceramics such as alumina.[5, 12] The influence of higher energy domains can be seen not only at grain boundaries, but also at the interfaces between dissimilar materials. When a crack arrives at the interface between dissimilar materials, if the interface is low enough toughness compared to the homogeneous materials on either side, it can often be favorable for the crack to propagate along the interface instead of travelling directly through into the second material.[13]

Geometric toughening can also manifest in composite structures with inclusions or dispersoids scattered in them. When a second phase of inclusions or heterogneities is present in a material, cracks can sometimes be forced to travel around these inclusions in order to continue propagation, depending on the residual stress state and the relative stiffness and toughness of the matrix with respect to the inclusion.

The shape and aspect ratio of these inclusions can have an influence on the extent to which the crack is deflected. The influence of inclusion shape and arrangement on the tilt and twist deflection behavior of a crack was explored for several common inclusion geometries by Faber and Evans.[14] The investigation explored how the aspect ratio, angle of orientation, and spacing of plates, rods, and spherical particles could influence the magnitude of the tilt and twist deflection angles exhibited by a propagating crack in a two-phase system. In addition to inclusion shape, spacing, and aspect ratio, the presence of residual stresses can also influence crack behavior. One of the earliest and clearest demonstrations of this was by Davidge and Green, who dispersed thoria spheres into melts of glasses with different thermal expansion coefficients.[15] As a result, when the glasses cooled, the residual stress fields around the thoria spheres would vary depending on the coefficient of thermal expansion of the glass with respect to the thoria. If the glass had a lower coefficient of thermal expansion than the thoria, the thoria spheres would have tensile residual stresses, and the crack would be attracted to the spheres, but if the glass had a higher coefficient of thermal expansion than the thoria, the spheres would be in compression, and the crack would deflect around the spheres instead.[15]

Toughening by Crack Shielding or Bridging

Going beyond geometric effects that influence crack path direction, composite systems can also be toughened by mechanisms that shield the crack and prevent propagation by either creating stress relief or a compressive closing force ahead of the crack tip or in the crack wake. These shielding mechanisms come in many different forms, and many of them involve composite structures with either multiple phases or non-homogeneous microstructure in the environment around the tip of the crack. The most common mechanisms for shielding in front of the crack tip are microcrack cloud formation, phase transformation, and the presence of a ductile or compliant second phase.[5] Microcrack clouds provide toughening by forming a dilation zone in front of the crack tip that increases compliance and reduces the overall stress available in front of the crack to drive propagation forward.[16] The most common form of phase transformation shielding is in zirconia-based systems, originally developed by Garvie et al., where a stabilizing agent, which is usually an oxide ceramic such as yttria, ceria, or magnesia, can help produce a metastable tetragonal phase that changes to monoclinic phase when exposed to the the stress fields created by crack propagation.[17] This phase change also creates an increase in volume, which produces compressive stresses that push the crack tip closed, making

propagation more difficult.

Toughening of ceramics can be achieved not only through interactions with the crack tip, but also by bridging the crack interface in the wake of propagation, which prevents the crack from opening further and slows growth.[5] This type of interface bridging technique can be achieved with whisker reinforcement, fiber reinforcement, or even with frictional effects from grains that bridge the crack interface. Many particle and fiber reinforced composites achieve higher toughness through this interface bridging mechanism. However, for many brittle fiber reinforced composites, the presence of fibers alone is not sufficient to see toughness improvement, but rather the interface between the fibers and matrix must be carefully designed to maximize toughening. If the fiber and matrix are too strongly bonded, the crack will simply fracture the fiber in the same manner as the matrix, and propagation will be relatively unhindered. Similarly, if the bonding between the matrix and fiber is too weak, the fiber will be readily debonded and pulled from the matrix, again providing little resistance to the propagating crack. However, if the interface is chosen to be sufficiently weak to allow for some debonding, but sufficiently strong to prevent complete pullout, the crack will deflect when it encounters the fiber, causing debonding, but then the fiber will ultimately have to be ruptured and pulled out in order for propagation to continue. This combination of debonding followed by rupture and pullout produces significantly higher toughening, especially in brittle systems with fiber reinforcement. The role of this carefully balanced interface on fiber mechanical response was first explored in detail by Marshall et al., and it is the reason that fiber compositions in ceramic composite systems must be carefully chosen, even though the introduction of fibers into a matrix is relatively straightforward.[18]

Limitations of Conventional Composite Toughening Space

All of the toughening mechanisms that have been discussed thus far have been explored in great detail across numerous material systems and have provided a great deal of toughness improvement for different technical ceramics. However, almost all of them share one common limitation, and it is not a material limitation, but rather a processing one. Almost all of the toughening mechanisms established rely on a combination of traditional ceramic and glass processing techniques and thermodynamics to achieve higher toughening. Polycrystalline interactions are controlled by the size and shape of grains, which are limited by the crystal structure and processing parameters during sintering or ceramic formation. Dispersoids and secondary phase particles are dispersed randomly throughout the any matrix

in which they are used, because they must be added either directly into a glass melt or via an intermixing of particles before sintering. Additionally, the shapes of different dispersoids and second phase particles is limited by crystal structure and available processing techniques, which is why most dispersoids are relatively simple shapes like spheres, plates, and rods. These limitations of randomly dispersed particles and phases whose structure is governed by crystallization or solidification thermodynamics means that the composite space is relatively constrained from the standpoint of design. On one hand, this random dispersion can be convenient. For example, the description of volume fraction of secondary phase is only meaningful when the secondary phase is randomly and uniformly distributed throughout the matrix such that the structure is effectively homogeneous. On the other hand, this is also a significant limitation because it represents an overall lack of complete processing control. Beyond uniform microstructural changes, the design of composite systems cannot be readily tailored for specific purpose. The one exception to this is fiber reinforcement, where, if the fibers are laid manually, different weave patterns can be achieved for different orientations, but even in this case, manual laying of fibers is time consuming, and the precise positions of individual fibers still cannot be readily controlled. In general, what this means is that most conventional composite theory has been built around these processing limitations, so once new processing methods are introduced, new design space becomes accessible.

1.4 Improved Processing Control Through Additive Manufacturing

On of the most promising ways that the processing space for brittle composites can be expanded is through the implementation of additive manufacturing. Traditional manufacturing techniques where a component is shaped, cut, or machined from a larger section of material would be classified as reductive manufacturing. In additive manufacturing however, each component is assembled from smaller portions of material that are combined into the exact shape of the desired part. This not only reduces waste, but allows for significantly more complex designs than traditional manufacturing would permit.

3D Printing

One of the most prevalent and widely used subsets of additive manufacturing is the field of 3D printing. Printing, in this case, is used to describe the deposition of material in a pattern dictated by a digital design. The nature of this deposition can vary widely depending on the material and process being used. The most common

forms of 3D printing are direct ink writing, binder jetting, direct laser melting, selective laser sintering, and stereolithography. Direct ink writing is exactly as its name describes, where the ink material is extruded through a nozzle and written into the desired shape based on a digital design. This is most commonly done with low melting point plastics, but can also be done with preceramic polymers, ceramic slurries, and even living cellular material.[19, 20] The biggest limitations of this technique are that it demands careful rheological control of inks to ensure extruded materials are stiff once they leave the nozzle, and the surface quality of parts formed by extrusion is dictated by the size and shape of the nozzle. Binder jetting, though less common, is similar in principle to direct ink writing. However, instead the material itself being extruded through a nozzle, the material, typically powder, is deposited layer by layer onto a bed, and binder is extruded through the nozzle to hold the powder together in select regions, forming the desired component.

Direct laser melting, also called direct metal laser sintering, is a layer-by-layer powder deposition technique similar to binder jetting, but it is typically done only with metal powders. Instead of gluing these powders together with binder, a high energy laser is used to heat up and locally melt the metal powders to form them into a single solid part.[21] With this technique, it is challenging both to avoid directionally dependent properties due to laser orientation as well as to achieve densities comparable to those seen in forged metals, but recently it has attracted great interest for its potential with nickel superalloys used in complex turbine components for aerospace and energy applications.[22] Selective laser sintering is similar in function to direct laser melting, but instead of using metal powders, it typically uses ceramic powders. The limitations of selective laser sintering are also very similar to those of direct laser melting, in that it is difficult to achieve ceramic densities comparable to those gotten with traditional powder sintering techniques.

Stereolithography The final 3D printing technique to be discussed is stereolithography, which is of particular focus because of its versatility and applicability to the materials investigated in this work. Stereolithography is a 3D printing technique that uses ultraviolet (UV) light to polymerize material in specific regions based on a pattern dictated by a digital design. In the case of laser stereolithography or two-photon polymerization, the UV light is introduced through a laser, and in the case of digital light processing, the UV light it introduced through a projector. Regardless, of the exposure method used, light-based techniques offer high resolution across multiple length scales because they can take advantage of

precise and well-controlled optical techniques originally developed for lithography patterning of silicon microdevices.[23] For this reason, components fabricated with stereolithography typically have good surface quality and feature resolution.

In addition to the optics, the material chemistry used in stereolithography is also based off systems originally developed for the patterning of silicon. Many of the earliest resins developed for stereolithography rely on acrylate polymer chemistry to form solids under UV light, similar to many of the photoresists used in traditional lithography patterning.[23] This acrylate polymerization is actually free radical polymerization, similar to that seen in many catalyst driven polymerization processes, but here the source of the free radical is a photoinitiatior that reacts with UV light of a certain wavelength range to produce free radicals. These radicals attack the acrylic endgroups of the multifunctional acrylate polymers present in the resin, causing them to polymerize into a cross-linked network. In the case of resins used in stereolithography, a photoinhibitor is also added to absorb either excess UV light or excess free radicals, depending on the polymer system being used. Finally, many resins also incorporate a compound for scavenging excess oxygen, which is known to inhibit polymerization.

Although acrylate chemistry is the basis for many of the resins used in stereolithography, it can also be used as a fabrication method for many other material systems. Through either functionalization or the incorporation of polymers with acrylate side chains, stereolithography can be used to directly fabricate components made of preceramic polymer, which can be converted into ceramics through pyrolysis, although shrinkage and the effects of volatilization of organics must be considered.[24–26] Additionally, ceramic particles can be dispersed into acrylate polymer systems at relatively high concentrations and then used for printing, with the acrylate polymers acting as a binder to hold the powders in place.[27] The challenges that arise with this approach are that the introduction of ceramic powders changes the photosensitivity and cure depth of the acrylate resin, and burnout and sintering must be carefully performed to properly remove all unwanted binder phase.[28–32] Ceramic structures can also be achieved with stereolithography by more indirect means. For example, acrylate polymer structures produced using two photon have been used as scaffolds for the fabrication of truss structures composed of alumina formed through atomic layer deposition.[33] All of these examples clearly show the potential of UV polymerization through stereolithography as a new processing method for the precision fabrication of brittle composite structures, both in acrylate polymers as well as in

ceramics.

1.5 New Toughening Methods Through Improved Processing

The significant improvements to additive manufacturing in recent years have greatly expanded the available design space for brittle composite systems by introducing a degree of control that was not previously available. Instead of having to rely on random dispersions of heterogeneities or toughening phases, it is now possible to control both the structure and position of inclusions or toughening phases. This change may seem subtle, but it is surprisingly disruptive as characterization of inclusions can no longer be driven by topology, as inclusions are no longer constrained to topological groups like spheres, plates, and rods. For this reason, different approaches need to be taken to understand how this new processing control can be fully utilized to create tougher composite materials.

Some attempts have been made to better explore the possibilities available for improving toughness through composite design with additive manufacturing, but these have been somewhat limited due to both the vastness of the design space as well as the challenges associated with properly describing brittle fracture of composite systems. From a numerical standpoint, attempts have been made to use tools like machine learning on voxel-based systems to maximize the toughness of a composite system around a known crack location.[34] However, these types of studies are somewhat limited because they fix the location of the crack in space and do not consider how the trajectory of crack propagation will change as the structure of the composite changes. In general, fracture analysis that considers the full trajectory of the crack is relatively challenging because considering all possible crack paths is very numerically intensive and the constantly changing boundary conditions due to the discontinuity created by the crack means that the system must be fully re-evaluated at every propagation step. To address this, variational approaches have been used to which treat the crack as phase field, which is then constrained to behave similarly to a discontinuity in the material.[35–37] This approach of treating the crack as a damage phase greatly reduces the computational load required to analyze fracture, and makes it much easier to analyze brittle failure in more complex structures. This variational phase field model has been used as a basis for several different fracture analyses, which have shown that composite toughness can be improved through both elastic contrast as well as toughness contrast, and that the shape and arrangement of inclusions in a structure can be chosen to dramatically minimize the volume fraction of inclusion phase needed to achieve comparable or greater toughening

than could be achieved through conventional composite processing.[38–40] Despite these promising numerical analyses, experimental verification of these potential toughening mechanisms is relatively limited. The influence of material contrast in 3D printed layered structures has been demonstrated both in the context of toughening due to the presence of elastic contrast as well as the influence of this elastic contrast and layer orientation on the renucleation and propagation of the crack through the structure.[41, 42] Beyond these studies, little has been done to investigate the effect of designed composite structure on fracture behavior in additive manufactured material systems in the context of inclusion arrangement, design, or anisotropy.

1.6 Objective

The objective of this work is to gain a better understanding of how the design freedom afforded by additive manufacturing might be better utilized to achieve higher toughness brittle composites. This work will focus on how designed structures can affect fracture behavior, what kind of material contrast is needed to achieve higher toughness, and how anisotropic structures might be used to improve toughness beyond what is possible with conventional processing techniques. This investigation will begin by using brittle photopolymers to explore the mechanisms that govern fracture in these designed composites. Chapter 2 will focus on how inclusion structures, both isotropic and anisotropic, can be used to affect the propagation behavior of a crack by means of elastic modulus contrast. Chapter 3 will extend this exploration of brittle polymers to consider how anisotropic structure can influence both crack nucleation and propagation in structures referred to as “fracture diodes”. The investigation then transitions into how similar toughening techniques might be implemented in ceramic systems, where achieving high toughness behavior is much more challenging. Chapter 4 explores the potential of heterogeneous structure in a model layered ceramic system, muscovite mica. Finally, Chapter 5 completes the extension into additively manufactured ceramics by exploring the effect of different truss structure elements on the failure mechanics of ceramics produced from preceramic polymer. Overall, the findings from this study will help inform composite design of brittle systems of different failure scenarios, which will further expand the available methods for the fabrication of tougher ceramic systems for numerous technical applications.

REFERENCES

[1] United States Energy Information Administration. Annual Energy Outlook 2019 with projections to 2050. Technical report, 2019. URL www.eia.gov/aeo.

[2] Koch Gerhardus, Jeff Varney, Neil Thompson, Dnv Gl, Oliver Moghissi, Melissa Gould, and Joe Payer. NACE Impact Report: International Measures of Prevention Application, and Economics of Corrosion Technologies Study. Technical report, 2016.

[3] A. A. Griffith. The Phenomena of Rupture and Flow in Solids. *Philosophical Transactions of the Royal Society A: Mathematical, Physical and Engineering Sciences*, 221(582-593):163–198, jan 1921. ISSN 1364-503X. doi: 10.1098/rsta.1921.0006. URL http://rsta.royalsocietypublishing.org/cgi/doi/10.1098/rsta.1921.0006.

[4] C.E. Inglis. Stresses in a plate due to the presence of cracks and sharp corners. *Trans Inst Naval Archit*, 55:219–241, 1913.

[5] Brian R. Lawn. *Fracture of brittle solids*. Cambridge University Press, 1993. ISBN 9780511623127.

[6] R. W. Hertzberg, R. P. Vinci, and J. L. Hertzberg. Dynamic Embrittlement. *Deformation and Fracture Mechanics of Engineering Materials*, 2012.

[7] G.R. Irwin. Fracture. *Handbuch der Physik*, 6:551, 1958.

[8] P.C. Paris and G.C. Sih. Stress Analysis of Cracks. In *Fracture Toughness Testing and its Applications*. 1965. doi: 10.1520/stp26584s.

[9] D. S. Dugdale. Yielding of steel sheets containing slits. *Journal of the Mechanics and Physics of Solids*, 1960. ISSN 00225096. doi: 10.1016/0022-5096(60)90013-2.

[10] G. I. Barenblatt. The Mathematical Theory of Equilibrium Cracks in Brittle Fracture. *Advances in Applied Mechanics*, 1962. ISSN 00652156. doi: 10.1016/S0065-2156(08)70121-2.

[11] James R Rice. Mathematical Analysis in the Mechanics of Fracture. Technical report, 1968. URL http://esag.harvard.edu/rice/018{_}Rice{_}MathAnalMechFract{_}68.pdf.

[12] Peter L. Swanson, Carolyn J. Fairbanks, Brian R. Lawn, Yiu-Wing -W Mai, and Bernard J. Hockey. Crack-Interface Grain Bridging as a Fracture Resistance I, Mechanism in Ceramics: I, Experimental Study on Alumina. *Journal of the American Ceramic Society*, 1987. ISSN 15512916. doi: 10.1111/j.1151-2916.1987.tb04982.x.

[13] J Cook and J E Gordon. A mechanism for the control of crack propagation in all-brittle systems. *Proceedings of the Royal Society of London. Series A. Mathematical and Physical Sciences*, 1964. ISSN 2053-9169. doi: 10.1098/rspa.1964.0248.

[14] K.T. Faber and A.G. Evans. Crack deflection processes—I. Theory. *Acta Metallurgica*, 31(4):565–576, apr 1983. ISSN 0001-6160. doi: 10.1016/0001-6160(83)90046-9. URL https://www.sciencedirect.com/science/article/pii/0001616083900469.

[15] R. W. Davidge and T. J. Green. The strength of two-phase ceramic/glass materials. *Journal of Materials Science*, 1968. ISSN 00222461. doi: 10.1007/BF00757910.

[16] A. G. Evans and K. T. Faber. Crack-Growth Resistance of Microcracking Brittle Materials. *Journal of the American Ceramic Society*, 1984. ISSN 15512916. doi: 10.1111/j.1151-2916.1984.tb18842.x.

[17] R. C. Garvie, R. H. Hannink, and R. T. Pascoe. Ceramic steel? *Nature*, 1975. ISSN 00280836. doi: 10.1038/258703a0.

[18] D. B. Marshall, B. N. Cox, and A. G. Evans. The mechanics of matrix cracking in brittle-matrix fiber composites. *Acta Metallurgica*, 1985. ISSN 00016160. doi: 10.1016/0001-6160(85)90124-5.

[19] Giorgia Franchin, Larissa Wahl, and Paolo Colombo. Direct ink writing of ceramic matrix composite structures. *Journal of the American Ceramic Society*, 100(10):4397–4401, oct 2017. ISSN 00027820. doi: 10.1111/jace.15045. URL http://doi.wiley.com/10.1111/jace.15045.

[20] Jennifer A. Lewis. Direct ink writing of 3D functional materials. *Advanced Functional Materials*, 2006. ISSN 1616301X. doi: 10.1002/adfm.200600434.

[21] Mukesh Agarwala, David Bourell, Joseph Beaman, Harris Marcus, and Joel Barlow. Direct selective laser sintering of metals. *Rapid Prototyping Journal*, 1995. ISSN 13552546. doi: 10.1108/13552549510078113.

[22] T. Vilaro, C. Colin, J. D. Bartout, L. Nazé, and M. Sennour. Microstructural and mechanical approaches of the selective laser melting process applied to a nickel-base superalloy. *Materials Science and Engineering A*, 2012. ISSN 09215093. doi: 10.1016/j.msea.2011.11.092.

[23] Paul F. Jacobs. *Rapid prototyping & manufacturing : fundamentals of stereolithography*. Society of Manufacturing Engineers in cooperation with the Computer and Automated Systems Association of SME, 1 edition, 1992. ISBN 9780872634251.

[24] Erika Zanchetta, Marco Cattaldo, Giorgia Franchin, Martin Schwentenwein, Johannes Homa, Giovanna Brusatin, and Paolo Colombo. Stereolithography of SiOC Ceramic Microcomponents. *Advanced Materials*, 28(2):370–376, jan 2016. ISSN 09359648. doi: 10.1002/adma.201503470. URL http://doi.wiley.com/10.1002/adma.201503470.

[25] Zak C Eckel, Chaoyin Zhou, John H Martin, Alan J Jacobsen, William B Carter, and Tobias A Schaedler. Additive manufacturing of polymer-derived ceramics. *Science (New York, N.Y.)*, 351(6268):58–62, jan 2016. ISSN 1095-9203. doi: 10.1126/science.aad2688. URL http://www.ncbi.nlm.nih.gov/pubmed/26721993.

[26] Johanna Schmidt and Paolo Colombo. Digital light processing of ceramic components from polysiloxanes. *Journal of the European Ceramic Society*, 38(1): 57–66, jan 2018. ISSN 0955-2219. doi: 10.1016/J.JEURCERAMSOC.2017.07.033. URL https://www.sciencedirect.com/science/article/abs/pii/S0955221917305186.

[27] Martin Schwentenwein and Johannes Homa. Additive manufacturing of dense alumina ceramics. *International Journal of Applied Ceramic Technology*, 2015. ISSN 17447402. doi: 10.1111/ijac.12319.

[28] Vladislava Tomeckova and John W. Halloran. Critical energy for photopolymerization of ceramic suspensions in acrylate monomers. *Journal of the European Ceramic Society*, 30(16):3273–3282, 2010. ISSN 09552219. doi: 10.1016/j.jeurceramsoc.2010.08.003. URL http://dx.doi.org/10.1016/j.jeurceramsoc.2010.01.027.

[29] Vladislava Tomeckova and John W. Halloran. Cure depth for photopolymerization of ceramic suspensions. *Journal of the European Ceramic Society*, 30(15): 3023–3033, 2010. ISSN 09552219. doi: 10.1016/j.jeurceramsoc.2010.06.004. URL http://dx.doi.org/10.1016/j.jeurceramsoc.2010.06.004.

[30] V. Tomeckova and J. W. Halloran. Macroporous polyacrylates from terpene-acrylate thermoreversible photopolymerizable vehicle. *Journal of Materials Science*, 47(16):6166–6178, 2012. ISSN 00222461. doi: 10.1007/s10853-012-6537-5.

[31] Vladislava Tomeckova and John W. Halloran. Porous ceramics by photopolymerization with terpene-acrylate vehicles. *Journal of the American Ceramic Society*, 95(12):3763–3768, 2012. ISSN 00027820. doi: 10.1111/j.1551-2916.2012.05444.x.

[32] Vladislava Tomeckova, Steven J. Norton, Brian J. Love, and John W. Halloran. Photopolymerization of acrylate suspensions with visible dyes. *Journal of the European Ceramic Society*, 33(4):699–707, 2013. ISSN 09552219. doi: 10.1016/j.jeurceramsoc.2012.10.015. URL http://dx.doi.org/10.1016/j.jphotochem.2012.08.008.

[33] Lucas R. Meza, Satyajit Das, and Julia R. Greer. Strong, lightweight, and recoverable three-dimensional ceramic nanolattices. *Science*, 345(6202):1322–1326, sep 2014. ISSN 0036-8075. doi: 10.1126/SCIENCE.1255908. URL http://science.sciencemag.org/content/345/6202/1322.

[34] Grace X. Gu, Chun Teh Chen, and Markus J. Buehler. De novo composite design based on machine learning algorithm. *Extreme Mechanics Letters*, 2018. ISSN 23524316. doi: 10.1016/j.eml.2017.10.001.

[35] G.A. Francfort and J.-J. Marigo. Revisiting brittle fracture as an energy minimization problem. *Journal of the Mechanics and Physics of Solids*, 46 (8):1319–1342, aug 1998. ISSN 0022-5096. doi: 10.1016/S0022-5096(98)00034-9. URL https://www.sciencedirect.com/science/article/pii/S0022509698000349.

[36] B. Bourdin, G.A. Francfort, and J-J. Marigo. Numerical experiments in revisited brittle fracture. *Journal of the Mechanics and Physics of Solids*, 48(4):797–826, apr 2000. ISSN 0022-5096. doi: 10.1016/S0022-5096(99)00028-9. URL https://www.sciencedirect.com/science/article/pii/S0022509699000289.

[37] Blaise Bourdin, Gilles A. Francfort, and Jean-Jacques Marigo. The Variational Approach to Fracture. *Journal of Elasticity*, 91(1-3):5–148, apr 2008. ISSN 0374-3535. doi: 10.1007/s10659-007-9107-3. URL http://link.springer.com/10.1007/s10659-007-9107-3.

[38] M. Z. Hossain, C. J. Hsueh, B. Bourdin, and K. Bhattacharya. Effective toughness of heterogeneous media. *Journal of the Mechanics and Physics of Solids*, 71(1):15–32, 2014. ISSN 00225096. doi: 10.1016/j.jmps.2014.06.002. URL http://dx.doi.org/10.1016/j.jmps.2014.06.002.

[39] C.-J. Hsueh. Effective toughness of heterogeneous materials. *PhD Thesis, California Institute of Technology*, 2017.

[40] E Tanné, T Li, B Bourdin, J J Marigo, and C Maurini. Crack nucleation in variational phase-field models of brittle fracture. *J Mech Phys Solids*, 110:80–99, 2018.

[41] Neng Wang and Shuman Xia. Cohesive fracture of elastically heterogeneous materials: An integrative modeling and experimental study. *Journal of the Mechanics and Physics of Solids*, 98:87–105, jan 2017. ISSN 0022-5096. doi: 10.1016/J.JMPS.2016.09.004. URL https://www.sciencedirect.com/science/article/pii/S0022509616303313.

[42] C-J. Hsueh, L. Avellar, B. Bourdin, G. Ravichandran, and K. Bhattacharya. Stress fluctuation, crack renucleation and toughening in layered materials. *Journal of the Mechanics and Physics of Solids*, 120:68–78, nov 2018. ISSN 0022-5096. doi: 10.1016/J.JMPS.2018.04.011. URL https://www.sciencedirect.com/science/article/pii/S0022509617311407.

Chapter 2

ANISOTROPIC STRUCTURE TO CONTROL PROPAGATION: SURFING LOAD EXPERIMENTS

Portions of this chapter contain content from "A non-constraining templated powder grid method for the measurement of strain" by N.R. Brodnik, C.-J. Hsueh, and M.T. Johnson, which was published in Strain in 2018 as well as from "Guiding and trapping cracks with compliant inclusions for enhancing toughness of brittle composite materials", which has been submitted to the Journal of Applied Mechanics.[1, 2] N.R. Brodnik led the design and fabrication of composite specimens for mechanical testing as well as the fabrication of grids for displacement measurement. C.-J. Hsueh led the numerical simulations for expected behavior as well as the design of the surfing load setup and the actual testing of specimens. Finally, G. De Luca is also acknowledged for his assistance in the evaluation of surfing load's suitability for the testing of ceramic systems. C.-J. Hsueh is also recognized for his assistance with the design of the simulation figures used in this work.

2.1 Introduction

The objective of this thesis work is to explore the effects of designed anisotropy on fracture properties and demonstrate how, alongside improved processing control, this anisotropic structure can improve the toughness of brittle composites. However, as was established in Chapter 1, formally characterizing the toughness of composite structures with arbitrary design is not straightforward, so careful consideration must be given to how structures are fabricated as well as how they are characterized. To address these issues, this chapter will explore how experimental design informed by numerical simulation can provide an avenue to investigate the influence of elastic contrast and anisotropic structure on fracture properties in heterogeneous composites.

The challenge of exploring fracture properties in composites with designed anisotropy arises from several different factors which must be addressed if experiments are to provide accurate data that is reflective of true material behavior. The two most significant of these factors are the location of crack-inclusion interaction events as well as the influence of elastic contrast on the strain field around the crack. The location of crack-inclusion interaction is crucial because, in the case of composite structures with discrete, macroscale inclusions with orientationally dependent design, the

traditional assumption of effectively homogeneous behavior does not hold. Therefore, the location of the inclusions with respect to overall structure must be considered during characterization. This point is particularly critical to emphasize, because it means that many of the traditional fracture characterization techniques such as compact tension, 3- and 4-point bending, and double cantilever beam testing are not feasible for evaluating the toughness of these composites, because they all rely on passive measurement of load and a particular specimen geometry for determination of fracture toughness. In cases of composites with microscale heterogeneities, this type of passive toughness characterization is still suitable so long as the spacing between heterogeneities is relatively small with respect to the size of the precrack. However, in the case of designed macroscopic inclusions and bulk composite structures, this is not the case. Consider a bimaterial beam being subjected to flexure with a single interface between the two materials that is parallel to the neutral axis of bending. If the only toughness enhancement exhibited by this composite structure is due to crack interaction with the bimaterial interface, the failure strength measured in bending will vary depending on the location of this interface with respect to the neutral axis, as shown in Figure 2.1. This variation in strength does not depend on the properties of the interface, but rather on the geometry of the specimen being tested. Logical extension of this idea clearly demonstrates how testing heterogeneous structures of arbitrary design is not sensible. For tests that determine toughness from measured strength, the strength will depend on the absolute position of the heterogeneity within the specimen, which means the test does not provide a meaningful evaluation of composite toughness as a material property. For this reason, in order to properly evaluate the toughness of composite structures with designed anisotropy, conditions of geometrically-independent, globally stable crack growth are required.

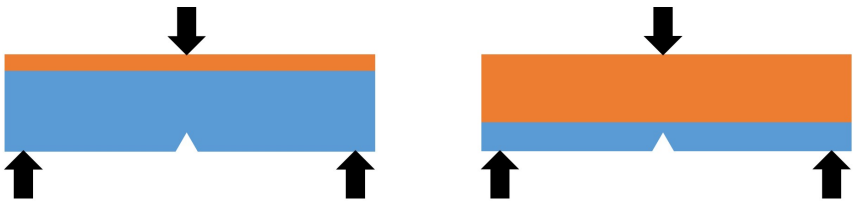

Figure 2.1: Schematic image of two bimaterial bend bars being subjected to 3-point bending. If toughening is achieved through property contrast between the two materials, these two bars will exhibit different strengths based solely on the location of the interface with respect to the neutral axis and precrack.

Beyond crack location dependence, the other challenge that must be addressed is the influence of elastic contrast on the stress field around the crack tip. In the case of dissimilar materials, it has been demonstrated that elastic contrast can have an influence on crack behavior by means of residual stresses, and the ratios of relative stiffness have an influence on how the crack behaves and whether it will pass through the interface between the two materials or be trapped along it.[3] However, the presence of elastic contrast presents another issue, because any elastic contrast in the environment around the crack tip will influence the resultant crack tip stress field as well as the analogous displacement field. Because the crack tip stress field scales with $r^{-\frac{1}{2}}$, where r is the radial distance from the crack tip, it is expected that even inclusions that are appreciably far from the tip of the crack will influence its propagation behavior, albeit less than those closer to the crack.[4] This means that in order to properly evaluate the toughness of a crack propagating through a heterogeneous system, the toughness evaluation must account for all heterogeneities present within that system. Normally this problem is addressed by treating the heterogeneous structure as effectively continuous and homogeneous and evaluating the toughness of the composite structure as a singular material. This approach works well for heterogeneous microstructures, but is not well suited to macroscopic inclusions with arbitrary spatial position for reasons that have already been established.

These two challenges together limit the scope of tests that are well suited for the mechanical characterization of composite structures with macroscale anisotropic inclusions of arbitrary design and spacing. In order for a test to provide meaningful insight, it must provide stable growth of the crack throughout the test without the aid of specimen geometry (e.g. grooves, tapers, crack channels). Additionally, in any tests performed, the mechanical behavior of the entire composite structure must be evaluated rather than calculating toughness from a load or strength measurement for a specific specimen geometry. In the case of this investigation, these two issues were addressed through the surfing load testing design and J-integral calculation done using displacement maps produced with the grid method. These two techniques together were used to investigate parameterized composite structures with both isotropic and anisotropic inclusions.

2.2 Geometrically-Independent Stable Crack Growth: Surfing Load

It has been previously established that to properly characterize composite structures of arbitrary geometry, it is necessary to have crack growth that is stable throughout

the entirety of mechanical testing and does not rely on any added specimen geometry to guide the crack. In this investigation, these requirements were achieved through a configuration referred to as surfing load. The surfing load boundary condition is a specific macroscopic boundary condition for stable crack growth originally developed by B. Bourdin and demonstrated in M. Z. Hossain et al.[5] The idea behind this boundary condition is to prescribe a Mode I opening displacement field that is localized to the area around the crack. This Mode I field is sufficiently large to propagate the crack, but there is no tensile displacement applied well in front of the crack, such that crack propagation is limited by the region over which this opening field exists. This opening field is then prescribed to travel at a steady velocity from one side of the specimen to the other. As this opening field moves, tensile stresses move along the specimen, making it energetically favorable for the crack to propagate at the same rate as the velocity of these tensile stresses. The theoretical approach for applying this type of boundary condition is discussed in detail in Hossain et al. and in the thesis of C.-J. Hsueh.[5, 6]

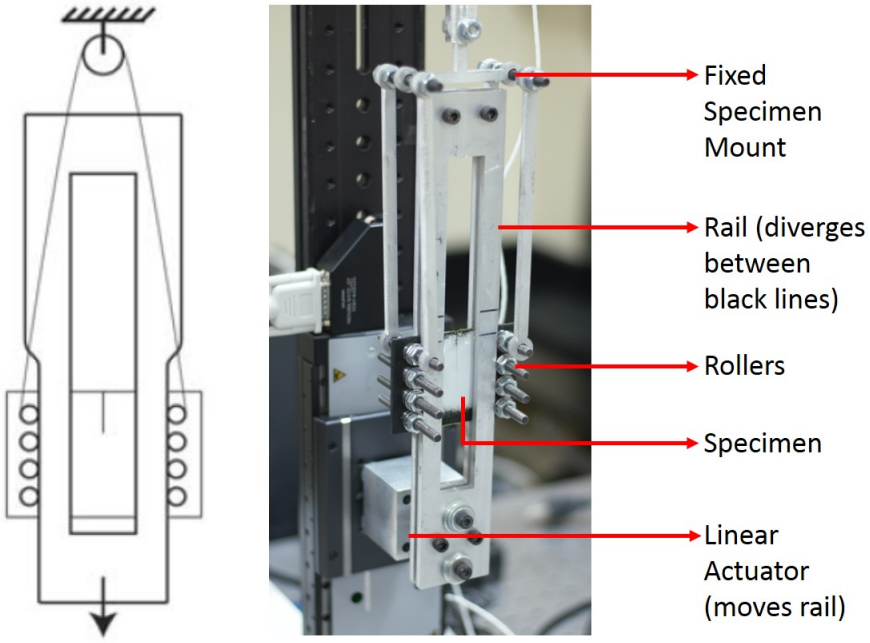

(a) Schematic Image (b) Experimental Setup

Figure 2.2: Schematic image of the surfing load design and a photograph of the analogous experimental setup. The black lines on the photographed rail surround the region of rail width divergence, which is significantly exaggerated in the schematic.

Applying this type of boundary condition is ideal for creating stable crack growth under tensile loading, as the rate of crack propagation is directly correlated with the

velocity prescribed in the boundary condition. However, applying a load with this degree of complexity in an experimental environment requires careful design. To address this, Hsueh, Bhattacharya, and Ravichandran developed a loading apparatus that can apply a boundary condition to physical samples that is very similar to the surfing load condition. A schematic of this design is shown in Figure 2.2a and the experimental equivalent is shown in Figure 2.2b. A stiff metal rail with a width increase along its outside edge is used to apply the Mode I load to the specimen during testing. This width increase is chosen to be exactly equal to the opening displacement needed to propagate a crack through the specimen. The outside edges of the specimen are constrained to the profile of the rail using a series of stiff pins surrounded by bushings and roller bearings. These pins pass through the specimen such that when the metal rail forces them outward, they pull on the material that surrounds them, forcing it open. Because the pins are kept flush to the rail and hold the sample in place, the surfing load profile is dictated by the taper along the outside of the rail, and the velocity of the Mode I opening regime is set by the velocity of the rail with respect to the sample. The number of pins chosen to apply the load was a balance between applying the surfing load as smoothly as possible and having the load fixture be stiff with respect to the specimen. In Figure 2.2, a total of 8 pins are shown passing through the specimen (4 on each side), as these were the smallest pins that were able to load the sample without flexing. In this load configuration, stable crack growth is actually maintained through the controlled failure of the specimen. The opening displacement on the outside edge of the rail is chosen to be sufficiently large to crack the specimen, and once the crack propagates due to this displacement the load drop associated with propagation is significant enough to prevent unstable crack growth.

2.3 Sample Design

Specimen Fabrication

The samples used in the surfing load design present some challenges from a fabrication standpoint, as they require arrays of holes on either end of the sample through which pins can be inserted to apply the surfing load. To address this, all samples investigated in this study were fabricated using digital light processing on an Autodesk Ember 3D Printer (Autodesk, San Rafael, CA). All specimens were printed using either a clear system known as PR48 or a black system known as PR57-K. Both polymers are urethane acrylate photopolymer blends with comparable stiffnesses and strengths. The formula for PR48 is reported in reference [7] and the formula for PR57-K is

a modification of the PR48 formulation that introduces black dyes for color and opacity. Using either polymer, the Autodesk Ember has a print voxel size of 50 x 50 x 50 microns which is well suited to printing surfing load specimens with high fidelity. The design for the surfing load specimens is shown in Figure 2.3. Surfing load specimens were printed to be 90 mm x 64 mm by 2.5 mm, with some additional thickness reinforcement present around the pinholes.

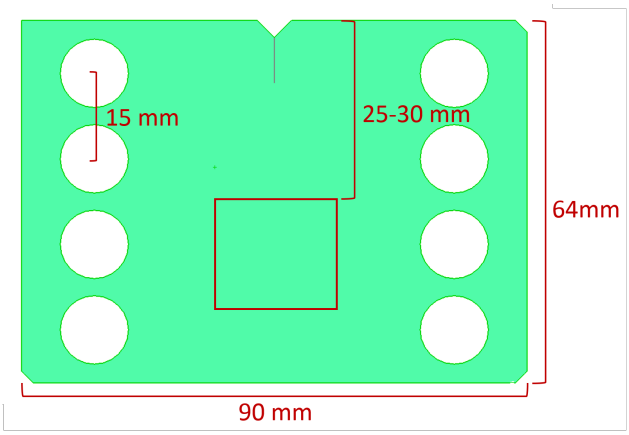

Figure 2.3: Schematic design of a surfing load specimen. Red box indicates region in which heterogeneous structures were analyzed.

It should also be noted that as previously discussed, in order for toughness characterization of heterogeneous structures to be reflective of behavior of the entire structure, all of the composite designs investigated in this study contained a relative small number of inclusions confined to a single region of characterization. This region of analysis is shown in the red box in Figure 2.3, which was placed between 25 and 30 mm down on the sample to allow for crack propagation to be fully stable before the start of analysis. Beyond this region, the sample was kept as homogeneous photopolymer. This allowed for uniform evaluation of crack interactions with inclusions and helped prevent any characterization bias that might arise due to the location of the crack with respect to the inclusions in the greater structure.

Composite Design

Once methods have been developed for continuous stable crack growth, the next step is to establish how the composite design space is going to be explored. This presents a particular challenge in the context of 3D printed composites because the design space is extremely large. To illustrate this point, traditional ceramic or metallic material design might use a parameter like volume fraction when describing the quantity of inclusions, dispersoids, pores, or toughening phases present in a particular composite

design. This volume fraction, along with a description of the size and structure of the inclusions as well as the assumption that the inclusion phase is randomly distributed, gives a clear description of heterogeneous structure within a particular composite. However, because processing techniques like additive manufacturing allow for control of the exact location of inclusions, volume fraction quickly becomes an inadequate descriptor, as there are effectively an infinite number of configurations of inclusions within a bulk structure, both uniform and nonuniform, that all have the exact same bulk volume fraction. This same principle holds with inclusion structure. In conventional composite theory, the influence of both structure and spacing of inclusions on fracture behavior has been explored for the most common inclusion shapes, including rods, spheres, and plates.[8] However, now that inclusions can be readily designed to be any shape or structure, exploring the space of possible inclusion shapes is not straightforward. Even when the the influence of inclusion shape is well understood, changes in material properties, including both stiffness and toughness, can have a dramatic effect on the behavior of the crack as it interacts with the inclusion as well as whether or not the crack becomes pinned at the interface between materials. All of these factors together make the design space for composites with designed anisotropic structures very large.

To better constrain the design space, we took the approach of parameterizing the composite structure to constrain as many geometric and material properties as was possible. Previously, layered printed structures were explored in double cantilever beam testing, but all structure and geometry in this study were effectively constrained to one dimension.[9] We chose to investigate arrays of circular inclusions in a staggered square pattern, as shown in Figure 2.4a. The inclusions were chosen to have a fixed spacing both between inclusions as well as between successive rows. The spacing d was chosen to be either 5 or 8 mm, depending on number of inclusions being included in the region of interest. Within this fixed spacing, the inclusion radius was varied to change the effective properties of the composite structure while maintaining a relatively standardized design.

In addition to a fixed arrangement with variable radius, a method was needed to vary the material properties without having unintended interfacial interactions or material incompatabilities. The main interest in this study was to explore elastic contrast, so, to provide a change in elastic contrast without creating unwanted incompatibility, the thickness of the printed material was changed at the inclusion locations, as shown in Figure 2.4b. This allows the whole composite to be printed from the same

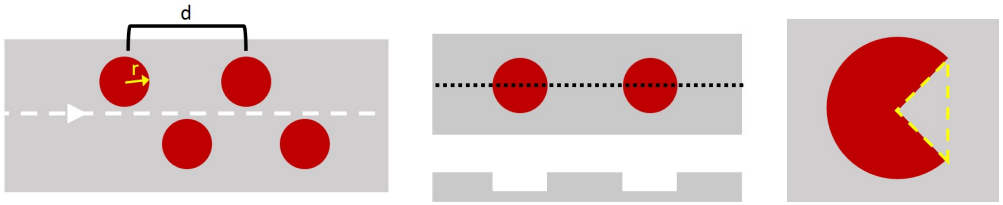

(a) Inclusion arrangment (b) Inclusion cross-section (c) Anisotropic Inclusion (right facing)

Figure 2.4: Schematic images of the parameterized composite design investigated in this study. Schematics show inclusion arrangement (a), inclusion thickness (b), and introduction of anisotropy (c). Anistropic inclusion is described as right facing to clarify directionality with respect to crack.

photopolymer. Printed samples were 2.5 mm thick, which is sufficiently thin to prevent any unwanted bending moments due to this thickness variation, and inclusion thickness was made to be 1/5 that of sample thickness. The inclusion and matrix layers were also made flush with one another on one side of the sample, as shown in Figure 2.4b to provide a single planar face for displacement mapping with the grid method. The change in thickness contrast has several effects on the relative properties of the photopolymer material. The first effect is the aforementioned reduction in effective inclusion stiffness, which is described in Equation 2.1

$$E^{inc} \propto \frac{t^{inclusion}}{t^{matrix}} \tag{2.1}$$

where E^{inc} is the effective elastic modulus of the inclusion with respect to the matrix, σ is the stress resulting from applied far field load, ϵ is strain, t^{matrix} is matrix material thickness, and $t^{inclusion}$ is inclusion thickness. Note that this is not an actual change in material properties, as the photopolymer material has a stiffness of about 740 MPa.[10] However, because the thinner inclusion regions are being characterized with respect to the thicker matrix regions, and they are both being subjected to the same far-field-loading, the inclusions will experience 5 times greater stress for the same loading. Consequently, they will effectively behave as though they have 1/5 the stiffness of the surrounding matrix. This same principle applies to effective inclusion toughness, as shown in Equation 2.2

$$\mathcal{G}_c^{inc} = \frac{(K_{Ic}^{inc})^2}{E^{inc}} \propto \frac{t^{inclusion}}{t^{matrix}} \tag{2.2}$$

where $\mathcal{G}_c^{inc}$ is the effective critical strain energy release rate and K_{Ic} is the effective fracture toughness of the inclusion with respect to the matrix. Again, similar to the stiffness, no material properties are actually changing, but because thickness variation changes the stress response to equivalent far-field loading, the relative toughnesses of the inclusion and matrix are different with respect to one another. Once the effective modulus and toughness of the inclusions are determined, these values can be incorporated into the composite design for a given geometry and unit cell arrangement. From here, the effective elastic modulus of the composite E^{eff} can be determined using a fast Fourier transform (FFT) calculation, and the effective strain energy release rate of the composite $\mathcal{G}_c^{eff}$ can be determined from the macroscopic J-integral. [6, 11–13]

Finally, once the inclusion arrangement, size, and properties have all been parameterized or constrained, the only remaining point of interest is the introduction of anisotropy. Because isotropic inclusions were chosen to be circles, anisotropy was introduced by cutting an isosceles right triangle out of the middle of the circle, to create an inclusion with directional stress concentrators as shown in Figure 2.4c. This allows for use of the same parameterization by circle radius and spacing for both isotropic and anisotropic inclusions and provides a reasonable basis of comparison.

2.4 Measurement of Toughness

Displacement Fields with Grid Method

With the surfing load method to provide stable crack growth in designed composite specimens, the next step in properly characterizing designed heterogeneous structures is developing a method of toughness evaluation that is not dependent upon the design parameters of the composite structure. As was established in Chapter 1, the J-integral developed by Rice is a promising candidate, as it provides a mathematically robust method for measuring toughness in a system and is able to capture changes in toughness that arise due to crack interactions with inclusions or other material contrast.[14] This J-integral technique is also able to measure changes in toughness as the crack propagates over time, as it does not rely on indirect strength measurements. However, in order to properly calculate the J-integral, full-field displacement measurements that do not affect mechanical response are needed throughout the fracture process.

Various types of non-contact full-field measurement methods have been implemented in experimental mechanics for well over 50 years and have proven to be extremely

useful in the characterization of material behavior. Generally, these full-field measurement techniques can be divided into two categories: interferometric techniques and geometric techniques. The former relies on interference patterns formed between a coherent light source interacting with the sample and a coherent reference light source, such as electronic speckle pattern, shearing, and moiré interferometry.[15] Interferometers can be used to track displacement along a single axis at sub-nanometer resolutions, but interferometric methods for measuring full-field displacements typically involve either a patterned surface, an intentionally roughened surface, or a material with particular optical properties, so resolutions tend to be limited to sub-micron or micron scales and only certain systems can be studied.[16–19] Although interferometric techniques can provide exceptionally high measurement resolution, even the simplest of interferometer setups is complex and sensitive to environmental effects such as vibration and sample drift, both of which are difficult to prevent in more complex setups such as the surfing load configuration.[20–23] Furthermore, displacements in interferometric techniques are deduced from measured interference patterns, so any error or experimental bias is not easily distinguished from measurement and must be carefully accounted for.[15, 16]

However, geometric techniques such as image correlation, speckle photography, digital image correlation (DIC), geometric moiré, and the grid method provide alternatives to interference-based measurement that are typically lower in accuracy, but are much more straightforward to implement and are not limited by the optical properties of the material. Of these, digital image correlation has gained particular popularity because of its simple implementation, especially compared to interferometric measurement techniques.[24, 25] Creating a pattern for DIC is very straightforward because only a random pattern of speckles is required. However, this random pattern can be optimized based on many different metrics, and the imaging analysis of these speckles can be done with a variety of methods.[21, 25–27] However, DIC does have some limitations, namely that resolution issues can be encountered when analyzing deformations that are both small and non-uniform, which are common in the fracture of brittle materials.[22] When addressing this issue, another non-interferometric technique known as the grid method acts as a compromise, in that it provides consistent measurement resolution of small and inhomogeneous strain while being relatively simple to implement.[28] The grid method is similar to DIC in that it is correlation based, however instead of using random patterns, it requires regular patterns of a known phase and pitch. By extracting the phase distributions of these regular patterns, a deformation field can be

obtained. The improved nonlinear resolution of the grid method and its robustness against noise are particularly useful in characterizing brittle fracture, as deformation during fracture is highly non-uniform and toughness calculations from full-field displacement measurements are very sensitive to noise. Introductions of numerical noise in amounts as small as 1% in DIC measurements have been shown to increase J-integral error by over 50%.[29]

The major disadvantage of the grid method compared to DIC is that the grid method relies on the deposition of a highly uniform and regular pattern as opposed to a random one.[30, 31] Some of the earliest grid mounting methods marked macro-scale grids onto samples and used the intersection points formed by the grid to track large scale displacements, such as those seen in sheet metal forming. [30, 32, 33] Macro-scale grids with pitches on the order of 0.8-1 mm have also been produced by spraying paint through a stencil.[34, 35] On the opposite end of the size spectrum, the smallest grids that have been used for full field strain analysis are sub-nanometer grids formed by the atoms in the material itself and imaged using high-resolution electron microscopy and atomic force microscopy.[36–39]

For fracture of macro-scale brittle polymer specimens such as those being considered in this study, the grids of interest have pitches somewhere between the atomic scale and the macro scale, specifically on the order of 5-150 μm. These grids are typically produced by first printing a grid with either high resolution digital printing or metal halide printing onto a polymeric substrate and then transferring the print layer from this substrate onto the sample using an adhesive such as epoxy.[40] This technique has the advantage that it can rely on high-fidelity printing techniques to produce uniform grids, and it has already been used to characterize the fracture of relatively high-toughness materials such as aluminum.[41] However, when the material being fractured has a toughness or stiffness that is very low compared to the grid itself, the epoxy layer used to adhere the grid and the print layer of the grid itself can distort the displacement information such that the displacements observed optically do not reflect the actual deformation of the specimen. This type of distortion in low toughness specimens is not surprising when one considers the sample to be a layered structure composed of the material of interest, the epoxy, and the grid print layer. Distortions of similar nature have been reported due to strain limitations in the grid layer when grids are produced using decal paper.[28, 42]

The specimens of interest in this study were made of stereolithographically printed photopolymer PR48 [7], which is a blend of multifunctional acrylate precursors.

This polymer has a modulus of about 740 MPa and a fracture toughness of about 0.2 MPa$\sqrt{\text{m}}$, giving it both low stiffness and toughness.[10, 43] This presents serious concern when mounting grid patterns using traditional epoxy mounting methods, as both the epoxy and polymer grid layers themselves can make non-negligible contributions to the effective stiffness and toughness of the specimen, distorting results, as shown in Figure 2.5.

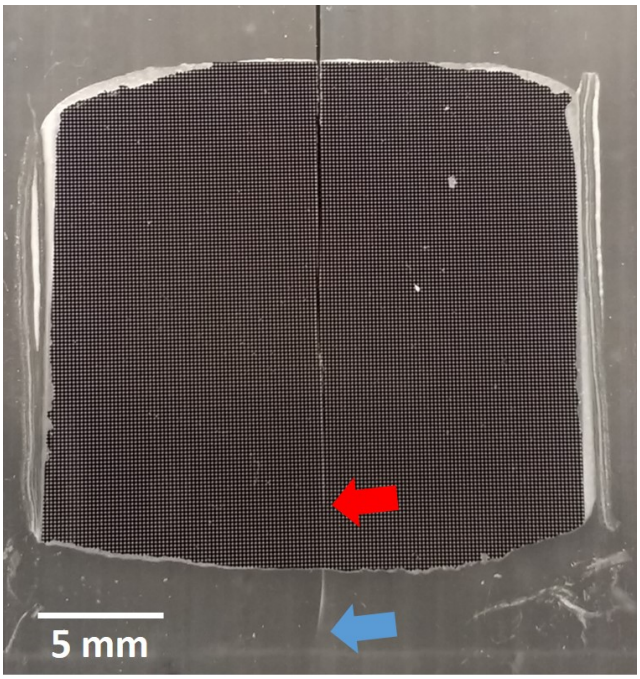

Figure 2.5: Closeup view of the region of interest on a transparent PR48 sample, with an epoxy grid mounted on the front face. Note that the presence of the grid toughens the front of the specimen so that the crack on the front side (red arrow) has not propagated as far as the crack on the backside (blue arrow), which is visible through the transparent polymer.

To limit this distortion, a new grid mounting method was developed that is suitable for displacement and fracture studies with any system compatible with photosensitive acrylic polymer. These new grids are formed by making a textured pattern of the grid on the specimen using photopolymer and then filling the spaces in this textured pattern with opaque powder pigment to achieve the needed contrast for grid method. The advantage of this implementation is that there is no need for a cured epoxy layer to create the grid pattern. Therefore, the bias of the epoxy layer is eliminated, and sample processing time is greatly reduced.

Powder Grid Method

The templates for the textured photopolymer grid pattern were made using traditional semiconductor photolithography techniques. A silicon wafer was coated with SU-8 photoresist to a thickness of 50-70 μm and then exposed through a square grid-patterned mask and subsequently developed. The result of this is a silicon wafer which has a uniform pattern of SU-8 pillars that are 50-70 μm tall and have spacing corresponding to the pitch of the grid. This resist-patterned wafer is then coated with Sylgard 184 liquid silicone and placed under rough vacuum for 30 min to allow for proper infiltration and degassing. Once infiltration is sufficient such that all trapped air is removed, the silicone is cured for 2 hr at 70 °C. Once fully cured, the silicone is separated from the resist-coated wafer to produce a silicone template mold with uniform square channels 50-70 μm deep with a pitch matching that of the silicon wafer. In this study, the grid pitch was chosen to be 120 μm based on the specifications of the camera used for imaging, but this pitch can be adjusted to be smaller or larger depending on the needs of the imaging setup.

To transfer a grid pattern onto a sample, a layer of liquid photopolymer is deposited onto the sample of interest using a transfer pipette. The photopolymers used in this study were PR48 and PR57-Y (Autodesk, San Rafael, CA). The silicone grid template is then introduced onto the liquid layer and allowed to settle under its own weight, after which the sample and silicone template are placed under rough vacuum for 10 minutes to remove all trapped air. After this rough vacuum, the samples are removed from the chamber, and any excess photopolymer is removed from around the sides of the template. The sample is then placed under UV light for 14-30 min (depending on sample thickness) to fully cure the liquid PR48 polymer into the shape of the silicone template. Because the polymer is physically constrained by the shape of the template, overexposure causing distortion of the grid pattern is not of particular concern. However, if the samples are placed in the UV oven for too long, the template can become difficult to remove from the sample, which can lead to the damage. Once polymerized, the photopolymer preferentially adheres to the specimen instead of the silicone template, so the template can be easily removed for repeated use. Once separated, both the sample and template are cleaned with isopropanol.

At this point, the surface of the sample is covered in a uniform array of pillars which correspond to the grid template, but this grid pattern has no optical contrast. To add optical contrast, the valleys between these pillars are filled with an opaque powder that is optically differentiable from the grid material. In the case of this study, the

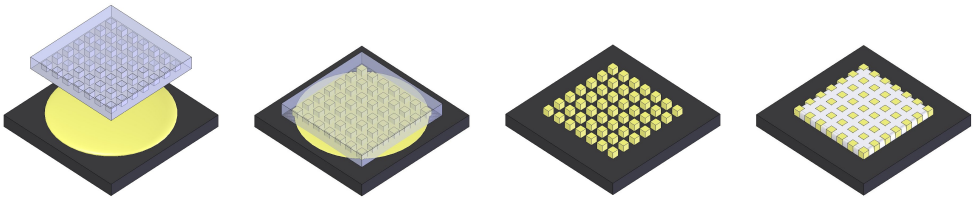

(a) Photopolymer deposition (b) Placement of template (c) UV cure/template removal (d) Powder fill-in

Figure 2.6: A schematic of the grid mounting process, shown with yellow photopolymer for clarity.

photopolymer used was translucent, so the powder chosen to fill in the valleys was Al_2O_3 with a median particle size of 350 nm (Baikowski Malakoff HP DPM [44]). The powder is either physically agitated or ground in a mortar and pestle to break up any aggregated particles and is then spread over the patterned sample face using a straight edge, taking care not to damage the array of pillars, as this will disrupt the grid regularity. Once the powder is spread, this same flat edge is used to remove any excess powder, leaving a grid pattern of white alumina on the sample. A schematic of the full process is shown in Figure 2.6.

Because the grid method only relies on the pitch and frequency of the waveform created by the applied grid, the color contrast of the grid can be varied based on the the color of the sample itself. Samples investigated in this study were either transparent or dark in color, and white powder was used to make the grid, but if a sample is brightly colored or white, a dark pigmented powder can be used to create a grid of black lines on the sample with no change in the efficacy of the grid. However, it is recommended that the powder chosen be neither carbon based nor a powder that would commonly be incorporated into lubricants, as these powders tend to smear during the spreading process, dramatically reducing imaging contrast. From a preparation time standpoint, fabrication of silicone templates for use in this method takes several hours, but templates are suitable for repeated use. Once templates are produced, the entire grid preparation process takes approximately one hour, far shorter than the epoxy cure step for traditional lithography grids, which can range from several hours to one day, depending on the epoxy.

Verification of Powder Grid Functionality

To ensure this new grid mounting method was comparable to prior grid methods and did not introduce any additional bias, some proof-of-concept testing was done to verify the functionality of these grids in controlled systems with well understood

behavior. First, some synthetic testing was performed using images of grids. These images were digitally manipulated to simulate known amounts of translation and biaxial strain, and these modified images were then evaluated using the grid method developed by Grédiac.[28] The results from the grid method measurements were then compared with the known values to ensure good fidelity. For these synthetic tests, three different grid types were compared: the powder grid developed for this investigation, a lithographically printed grid that would be used in conventional epoxy-mounted grid testing, and an idealized grid made using a superposition of two sine functions that was displayed as an intensity map. This last grid was only used for synthetic tests because it was produced digitally and does not exist in any physical form. The mathematical details of both fabrication of the digital grids as well as mathematical analysis of grid performance can be found in reference.[1] All three grids are shown in Figure 2.7.

The mean errors measured in pixels for both the biaxial strain and translation synthetic tests are shown in Figure 2.8. The fluctuating behavior seen in the translation error is a product of error arising from subpixel interpolation, and the variation in the digital grids results from aliasing effects due to imperfect subpixel interpolations of the perfect sinusoidal waves. When the three different grids are compared, the general trend is that the powder grid performs slightly worse than the lithographic and digital grids, but this is to be expected, as the powder grids themselves are fabricated using a lithographic grid as a starting template, and the fabrication process is expected to produce some additional error. However, this increase in error is still relatively small and is seen as a reasonable tradeoff to permit the use of the grid method in the fracture analysis of low toughness materials.

To verify the functionality of this new grid method in fracture studies, homogeneous PR48 specimens were fractured using the surfing load condition and characterized using the powder grid method. These specimens, which had a fracture region with dimensions of 62 mm x 36.5 mm x 1.5 mm, were printed using the same digital light processing techniques as the other surfing load samples (Ember® 3D Printer by Autodesk, San Rafael California). The powder grids developed were used to measure the displacement and strain fields, and the J-integral was then calculated from the strain field to determine the critical stress intensity factor. The stress intensity factors associated with different crack lengths are plotted in Figure 2.9. The measured critical stress intensity factor of the 3D printed polymer specimen was determined to be 0.187 ± 0.014 MPa$\sqrt{\text{m}}$. This is very similar to the previously measured value

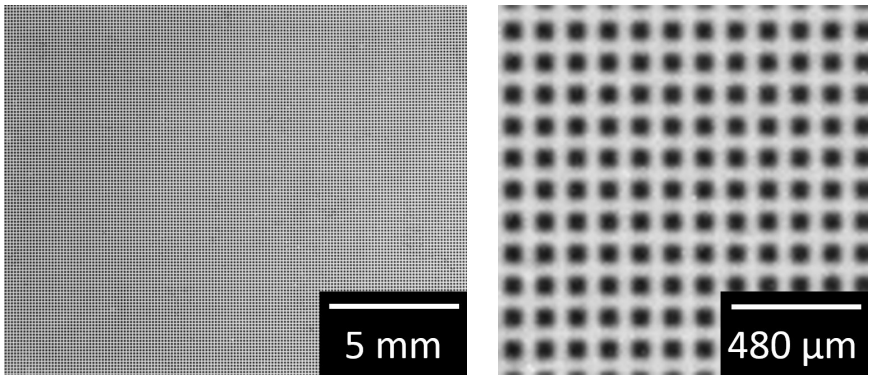

(a) Powder grids (b) Powder grids (magnified)

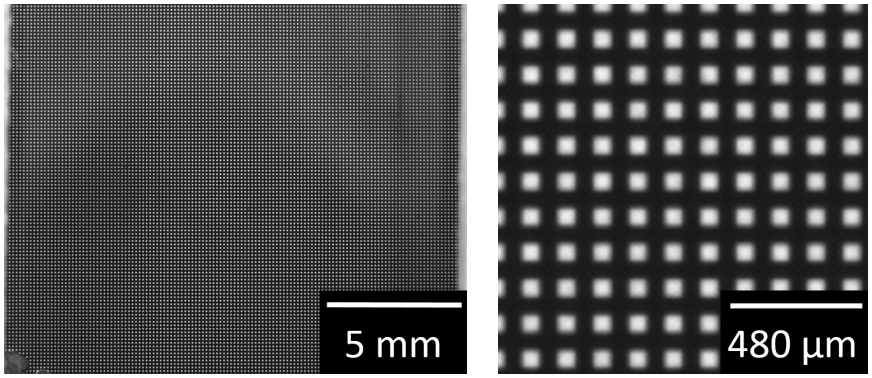

(c) Lithographic grids (d) Lithographic grids (magnified)

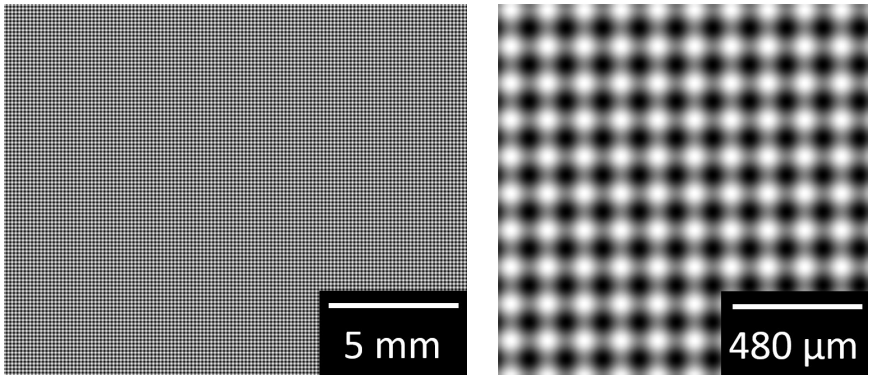

(e) Digital grids (f) Digital grids (magnified)

Figure 2.7: Grid patterns used in synthetic testing.

of 2 MPA$\sqrt{\text{m}}$, which both verifies the functionality of the powder grids as well as provides a suitable baseline of homogeneous photopolymer toughness for later experiments.

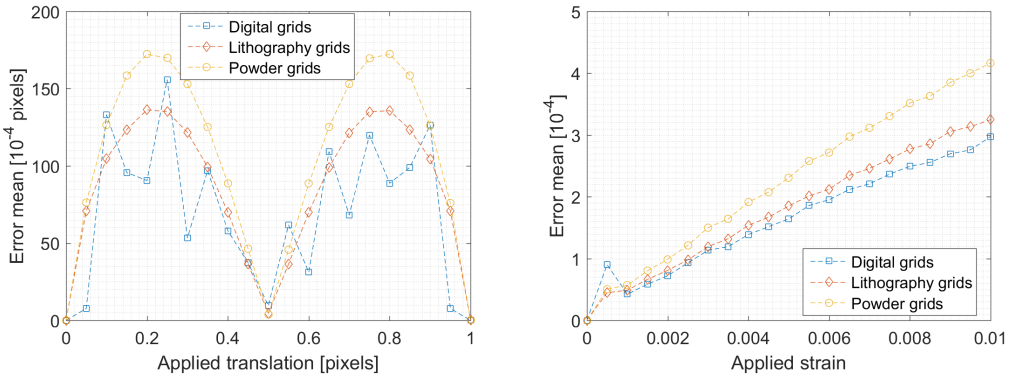

Figure 2.8: Mean errors measured from the synthetic translation and biaxial strain tests.

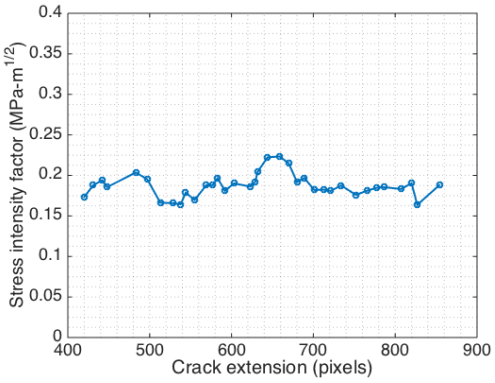

Figure 2.9: Stress intensity factor vs. crack extension for PR48 photopolymer in surfing load fracture conditions.

2.5 Results and Discussion

Numerical Simulations

With a means of fabricating and characterizing parameterized heterogeneous structures fully available, simulations of surfing load conditions were used to explore the design space in the context of effective stiffness and effective toughness. Simulations were done using the variational phase field models implemented by Bourdin.[45–47] For the same pattern of staggered circles discussed in Section 2.3, the radius of the inclusions was changed and the effective stiffness of the system was measured numerically. Then, the effective toughness was measured numerically using surfing load conditions, and the two were plotted against one another, as shown in Figure 2.10. The numerical implementation of this simulation was done by C.-J. Hsueh and is discussed in reference.[6]

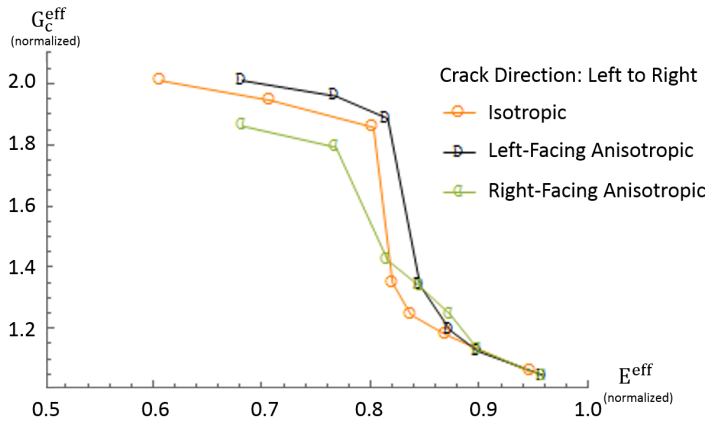

Figure 2.10: Comparison of effective stiffness and effective toughness (normalized to the matrix material) for composite structures with staggered patterns of either circular inclusions or anisotropic circular inclusions. For all cases, $E^{inclusion} = \frac{1}{5}E^{matrix}$. Crack propagation is described as left-to-right to establish directional distinction between different anisotropic inclusions.

It is important to note that because the composite structures contain macroscopic discrete inclusions, the toughness is not necessarily uniform throughout the entire structure. However, extension of tradition fracture theory indicates that it is reasonable to assume that the effective toughness of the composite structure is the peak value of the J-integral, which is related to the peak strain energy release rate.[14, 48, 49] Because there was particular interest in the effect of elastic contrast on effective toughness, initial simulations were done without any toughness contrast between the inclusions and matrix, so the only difference between the inclusion phase and matrix phase was elastic modulus, with inclusions be 1/5 as stiff as the matrix. Using this basis, the size of the inclusions was varied to change effective stiffness, and the impact on toughness was measured through the J-integral.

When explored in terms of effective stiffness, Figure 2.10 shows several interesting relationships. At the far right of the stiffness axis is the homogeneous matrix material, which has a normalized stiffness of 1 and a normalized toughness of 1. Once inclusions are introduced, the toughness increases slightly at the expense of stiffness. This increase is not actually due to direct interaction between the cracks and inclusions, but rather deflection of the crack due to attraction towards the more compliant heterogeneities. However, once inclusions are sufficiently large that $E^{Eff} \leq 0.8$ for the isotropic case, the crack is drawn into the inclusions and is pinned by the elastic contrast between inclusion and matrix. It should be noted

that in the case of the simulation, the both the inclusions and matrix are treated as homogeneous materials with uniform unit thickness, so the observed toughening is due entirely to this elastic contrast effect. This phenomenon of crack pinning at the interface where there is an increase in elastic contrast causes a dramatic increase in the effective toughness of the composite structure, and is responsible for the jump in composite toughness.

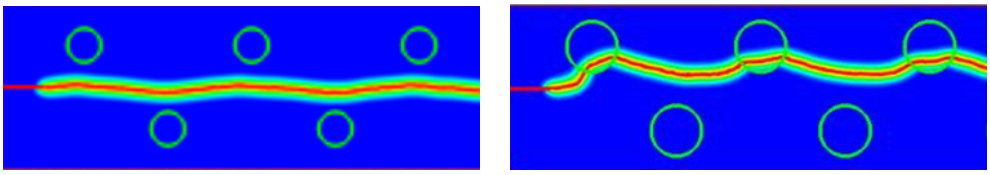

(a) Smaller inclusions (crack deflection) (b) Larger inclusions (crack pinning)

Figure 2.11: Simulations showing crack behavior with smaller and larger isotropic inclusions. For the smaller inclusions (a), $E^{Eff} = 0.95$, and only crack deflection is observed, which produces marginal toughness increase. For the larger inclusions (b) $E^{Eff} = 0.8$, and crack pinning is observed, which produces greater toughness increase.

The introduction of anisotropy has two distinct effects on the toughenss-stiffness relationship, namely it changes both the magnitude and location of the toughness increase due to crack pinning interactions. The change in magnitude of the toughness increase is directly related to the shape of the anisotropic inclusions, namely the the location of stress concentrators. For a crack that is traveling from left to right, a left facing anisotropic inclusion forces the crack to enter and exit the inclusion along the circular edge, so it effectively behaves like a circular inclusion, as shown in Figure 2.12a. For the right facing inclusions however, the stress concentrators in the inclusions make it far easier for the crack to exit the inclusion, as shown in Figure 2.12b, so the toughness improvement is not as significant in this case.

While the effect of anisotropy on the magnitude of the toughness increase is relatively straightforward, its effect on the location of the transition between crack deflection and elastic contrast crack pinning behavior is a bit more subtle, and arises due volume fraction effects. Because the anisotropic inclusions have a triangular section cut out of a circle of fixed radius, anisotropic inclusions have a smaller volume fraction of inclusion phase than isotropic inclusions of equivalent circle radius. Since effective stiffness is determined by the volume fraction of compliant inclusion phase, the anisotropic inclusions can achieve elastic contrast crack pinning behavior with a smaller reduction in effective stiffness.

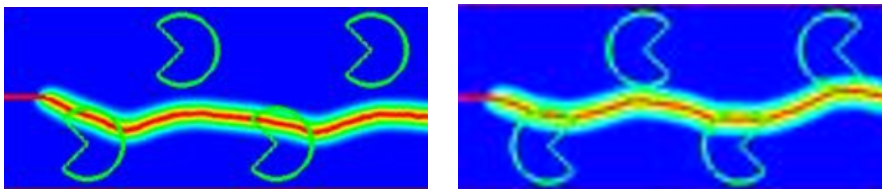

(a) Left Facing (b) Right Facing

Figure 2.12: Simulations showing effect of anisotropy on fracture. In both simulations, crack propagation is from left to right. Right facing inclusions (a) showed comparable toughness to isotropic inclusions, albeit at higher effective stiffness. Left facing inclusions (b) showed lower toughness than isotropic due to the presence of stress concentrators.

Experimental Results

In the experiments on PR48 and PR57-K, inclusions had a lower effective stiffness, similar to simulations, but also a lower effective toughness than the surrounding matrix, so analysis of behavior was not as straightforward. Even in this case however, the toughness of the composite can still be characterized using a J-integral with displacement maps from the powder gird method.

Initial experimental characterization focused solely on isotropic inclusions in an attempt to capture both deflection and elastic contrast pinning behavior as inclusion size varied. To have a more complete understanding of expected behavior, additional simulations were also carried out with inclusions that had both lower stiffness and lower toughness. A comparison between simulation and experimental results is shown in Figure 2.13.

Observation of Figure 2.13 shows several apparent differences between simulation and experiment. The most apparent difference between simulation and experiment in Figure 2.13 is that for all cases, the toughness measured in experiment is markedly higher than the toughness predicted by simulation. It is suspected that this difference arises not from inaccuracies in the simulation, but rather from unexpected behaviors arising from sample design. Changes in thickness proved to be a convenient way of introducing elastic contrast without a distinct material interface, but these thickness changes also created unintended geometric effects.

When the crack becomes pinned in the more compliant inclusions, the change in thickness also causes a reduction in crack front length. Then, when the crack reaches the end of the inclusion and propagates back into the matrix, the pinned crack front is forced to bow due to the change in geometry in order to continue propagation into the thicker matrix, evidence of which is shown in Figure 2.14. This added geometrical

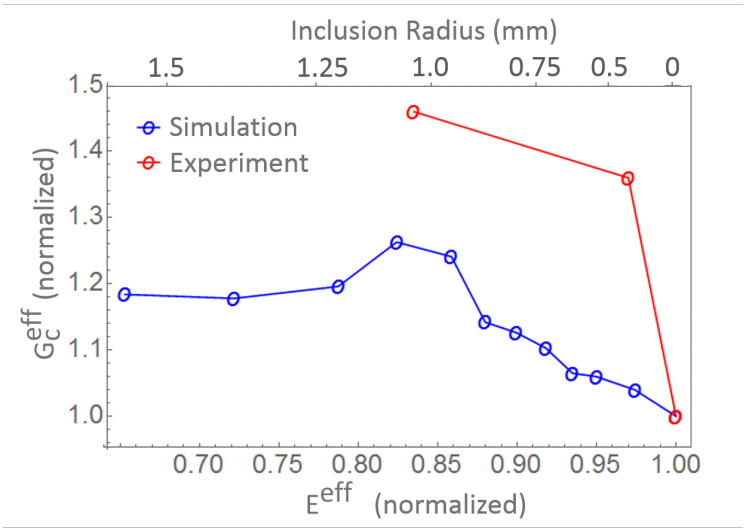

Figure 2.13: Comparison of effective stiffness and effective strength (normalized to the matrix material) for composite structures with staggered patterns off isotropic circular inclusions made by varying sample thickness. Comparison shows both expected toughness from simulation as well as toughness measured in experiment.

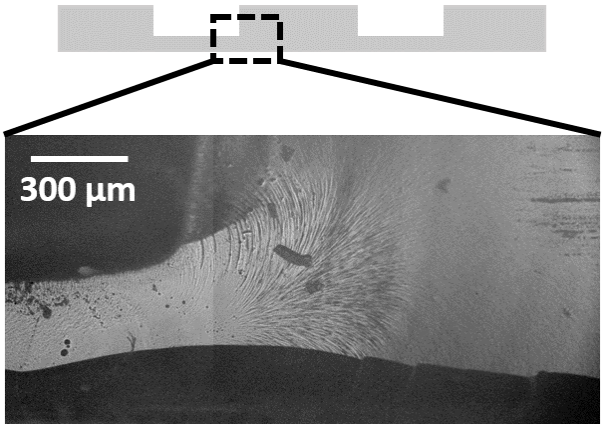

Figure 2.14: Optical micrograph showing the unintended geometrical toughening effect in the E^{Eff} = 0.83 sample. Because elastic contrast was introduced through thickness variation, the crack was forced to bow outward around the thickness change when exiting the inclusion, creating additional toughening.

bowing effect causes additional toughening beyond what would be present if the inclusions were instead the same thickness as the matrix, but a different material.

In addition to this geometric effect, there is another disparity between simulation and experiment. In the case of small inclusions where effective stiffness is higher, the toughness measured in experiment is substantially higher than predicted by

simulation, with the gap between simulation and experiment being far greater than for larger inclusions. This additional disparity arises because at small inclusion sizes, simulation predicts that the crack will exhibit only a slight deflection behavior, where it is briefly drawn toward the inclusions, but never pinned by them. However, in actual experiments, the crack was reliably pinned by inclusions regardless of size, which leads to the significantly higher toughness seen at high effective stiffness in Figure 2.13. The main cause of this difference in behavior is crack alignment. In simulation, it is straightforward to center the crack perfectly between rows of inclusions in the composite structure such that is deflects evenly as it propagates. However, doing this in experiment is not as simple. An example of this is shown in Figure 2.15, where a difference in crack position of about 300 µm is enough to produce an elastic contrast crack pinning event. This level of sensitivity to small deviations in crack position is likely why no experimental specimens exhibited crack deflection behavior without also having elastic contrast pinning.

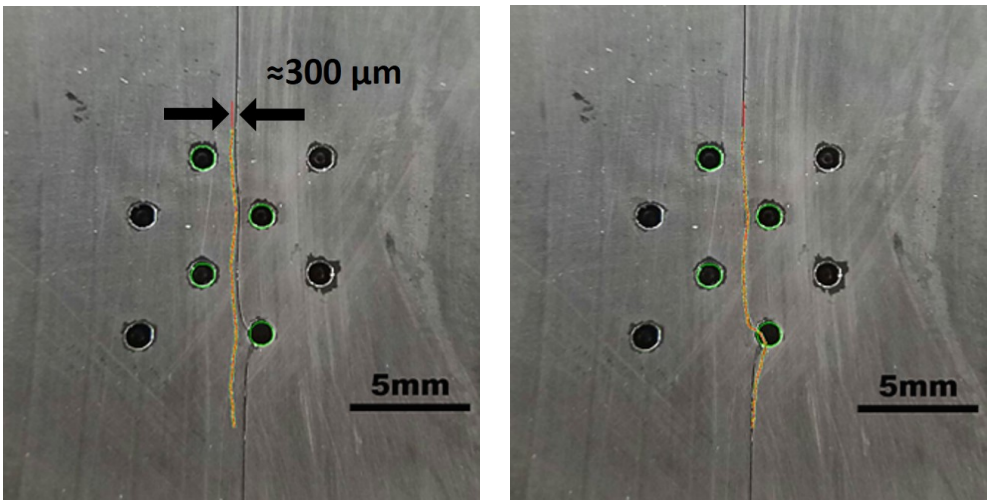

(a) Crack and simulation not aligned (b) Crack and simulation aligned

Figure 2.15: Overlay of simulation results onto experimental results for the case of E^{Eff} = 0.95 and d = 5 mm, showing the influence of crack misalignment. In (a) the simulation is perfectly centered between the inclusions, but the actual crack is misaligned by about 300 microns, so the resultant behaviors are different. Once the simulation is adjusted off-center in (b) however, simulation and experiment match one another.

It should also be noted that there are no experimental data points present for isotropic inclusions of larger radius ($E^{Eff} < 0.83$ or for any anisotropic inclusions. This is due to challenges that arose from unstable crack propagation as well as deviations between the idealized surfing load condition and the experimentally applied surfing

load. For inclusions of radius greater than r ≈ 0.75mm (E^{Eff} = 0.83), cracks have a greater tendency to rapidly and unstably propagate between successive inclusions. In the case of simulations, this is not an issue, as it is relatively straightforward to have the load travel steadily with the tip of the crack. However, the experimental setup relies on steady propagation of the crack to prevent buildup of tensile load as the sample travels along the rail. As a result, samples with inclusions of radius greater than r ≈ 0.75mm exhibited significant pinning at the first inclusion encountered followed by sudden rapid propagation through the specimen that could not readily be analyzed.

This pinning behavior followed by rapid propagation was also seen in nearly all anisotropic samples, as the presence of stress concentrators further increased the tendency for unstable crack propagation. As a result, no reliable toughness measurements were able to be made, and the anisotropic specimens could only be characterized based on crack path analysis after fracture. Even so, when the crack paths of the different anisotropic specimens are analyzed, differences are noticeable between different inclusion orientations. In the case of left-facing inclusions, the crack enters and exits through the circular arc region of the inclusion, as predicted by the simulation, which would indicate a toughening effect similar to that of isotropic circles. Alternatively, the crack path of the specimens with right-facing heterogneities follows successive stress concentrators, which would indicate a lower toughness behavior, as predicted by simulations.

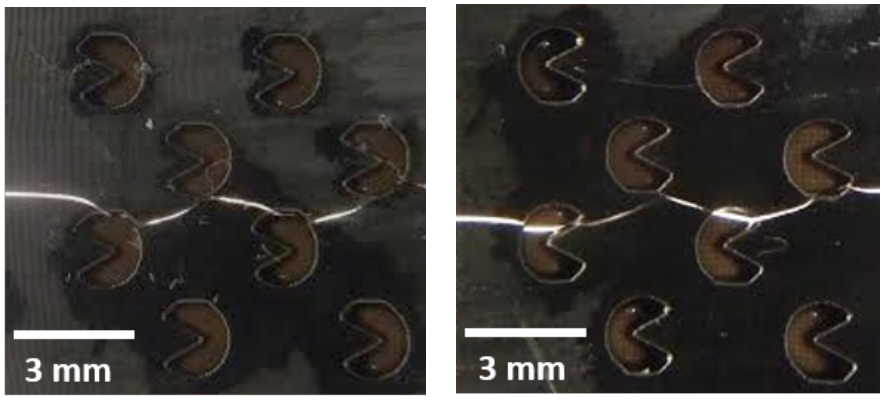

(a) Left Facing (higher toughness) (b) Right Facing (lower toughness)

Figure 2.16: Images of anisotropic composites E^{Eff} = 0.82 showing the difference in crack behavior between (a) left- and (b) right- facing heterogeneities. In both cases, crack propagation was from left to right.

2.6 Outlook

Experimental Limitations

Although experiments were able to demonstrate composite toughening for some cases of isotropic heterogneities, overall, the composite design space that could be explored was relatively limited. This was due not only to the previously discussed unstable propagation behavior, but also due to large variability seen in the measured mechanical response of the photopolymer specimens. It is suspected that this variation is not the result of the testing technique, but is rather due to limitations associated with the material itself. The PR48 photopolymer was a well-suited model material because of its brittle nature, good shape retention, and compatibility with the Ember DLP printer used for sample fabrication. However, with PR48 as well as all other acrylate photopolymers, some issues arise with material stability. Many of the acrylate photopolymer systems used in stereolithography and digital light processing are based on photochemistry originally developed for mask lithography of silicon wafers. These systems have exceptionally good definition and shape retention, but they were not designed for long term use or stability, particularly in environments containing UV light and oxygen. This is demonstrated in a study by Chiantore et al. on the photodegradation of acrylic and methacrylic polymers.[50] The study explored the degradation behavior of four different polymers: poly(methyl acrylate), poly(ethyl methacrylate), poly(ethyl acrylate), and poly(butyl methacrylate). Each polymer was subjected to both UV radiation and oxygen, and the extent of degradation was characterized by the extent of volatilization of low molecular weight groups as well as the oxidative cross linking of side chains. The general trends in decomposition behavior were that methacrylic polymers were more stable than acrylics, and polymers with smaller side groups tended to be more stable, e.g., poly(butyl methacrylate) exhibited the most rapid and extensive decomposition as well as the most cross-linking of side chains.[50] Although to date, no quantative degradation analyses of 3D printed polymers have been published, the trends in the investigation by Chiantore et al. are highly unfavorable for many 3D printing photopolymers, including the PR48 used in this study. These polymers tend to be acrylates with very large side chain groups to minimize the amount of network formation needed achieve freestanding solid.[7] This implies that these polymers are likely to be very succeptible to degradation in environments containing oxygen and UV light, which includes the environment in which surfing load tests were performed. This degradation can lead to embrittlement and significantly higher variability in mechanical properties, which makes direct comparison of strengths and toughnesses

much more difficult. Additionally, cleaning and drying processes that expose the polymer to solvents can further lead to nonuniform embrittlement, which further increases mechanical variability. Such limitations made detailed mechanical analysis of composite structures made from PR48 especially challenging.

2.7 The Potential of Anisotropic Heterogenities

Up to this point in the investigation, anisotropy has only demonstrated the potential to achieve comparable toughness to isotropic inclusions under certain loading conditions. However, the real potential of anistropic inclusions lies in the case of biased or directional loads. Both numerical simulations and crack path evaluation show strong evidence that in one particular direction, anistropic inclusions behave very similarly to isotropic ones. Additionally, numerical simulations showed that anisotropic inclusions could demonstrate similar toughness to isotropic ones at smaller volume fractions, as the removal of one portion of the circle significantly reduces the total volume occupied by the inclusion. This reduction in volume at the expense of toughness in one direction is where the potential of these anisotropic inclusions lies. If a composite is expected to experience a biased or directional load, anisotropic inclusions could be used to toughen the composite in that particular direction with significantly less impact on bulk properties. The achievable limit of this type of toughening is dictated by processing though, so the dilute limit of toughness attainable without significant modulus reduction is dictated by the resolution at which structures can be fabricated without loss of fidelity. Even so, this type of anisotropic composite reinforcement could, make it much easier to toughen extremely stiff materials with a more compliant phase without creating a dramatic loss in stiffness which would be extremely desirable in many different applications where ceramics or brittle metals are traditionally used, such as engine environments or structural applications.

Extension to Ceramics

Given the limited chemical stability of photopolymers and the potential of anistropic toughening in systems, it is logical explore the extension of these designs into ceramics systems. However, extending the surfing load configuration into ceramics proved infeasible, not because of challenges with sample fabrication, but because if difficulties with surfing load test design. For the experimental implementation of the surfing load, a diverging rail is used to prescribe the crack opening displacement to the sample, as shown in Figure 2.2. The magnitude of the divergence on this rail is

chosen based on the stiffness and fracture toughenss of the material being fractured. For the case of the brittle photopolymer PR48, the toughness of the photopolymer, 1-2 MPa$\sqrt{\text{m}}$, is comparable to that of many ceramics and glasses, but the stiffness of the photopolymer, around 740 MPa, is lower than most ceramics and glasses by at least a factor of 100. This means that in order to test ceramics using the surfing load, a rail with a diverging width about 100 times smaller than the current design would be needed. For the PR48 photopolymer, the rail used was made of 6061 aluminum (McMaster Carr, Elhurst, IL), and the divergence used was on the of 1-2 mm. Therefore, to test ceramics using this same design, a rail would need to a divergence on the order of tens of microns with very tight tolerances, and almost all slip in the pins and bearings used to move the sample along the rail would have to be removed. For this reason, the surfing load proved infeasible for use on ceramics, and other characterization techniques were explored in Chapters 4 and 5.

2.8 Summary

To gain a better understanding of the effects of designed anisotropy on crack propagation, we explored parameterized composite structures under stable crack growth conditions with full-field displacement measurement techniques. The composites were printed using PR48 photopolymer and stable crack growth was achieved using a novel controlled propagation technique known as the surfing load. Toughness analysis was achieved through the use of J-integrals performed on displacement fields obtained using the grid method on uniform grid patterns composed of photopolymer and powder to minimize their impact on fracture behavior. Composites were parameterized by fixing inclusion arrangement to be a staggered pattern of circular inclusions, and the stiffness of the structures were varied by changing the radius of these inclusions. Rather than using a second material, elastic and toughness contrast were tailored between inclusion and composite by changing the thickness of the specimen in different regions to change the relative stiffness and toughness. Finally, anisotropy was introduced into the structure by cutting an isosceles right triangle out of the circular inclusion to make an incomplete circle with stress concentrators on one side.

Numerical analysis showed that the introduction of more compliant heterogeneities increased composite toughness marginally at first, and then much more significantly, as the the elastic contrast from the inclusions became significant enough to produce crack-inclusion interaction. The initial marginal increase was related to crack deflection behavior, where the crack would be attracted to inclusions, altering

its propagation trajectory, but no actual pinning would occur. Once inclusions increased enough in size to create sufficient elastic contrast, the crack would be pinned in the inclusions, causing a significant increase in toughness. This toughness improvement due to elastic contrast was seen both in numerical simulations as well as analogous experiment, though no toughening through crack deflection was observed in experiment due to the sensitivity of the deflection behavior to small changes in crack position. In the case of anisotropy, the presence of stress concentrators on one side of the circular arc of the specimen reduced the toughness improvement from elastic contrast pinning in one direction, but the opposite direction exhibited similar toughening to the isotropic case, albeit at a smaller inclusion phase fraction. Experimental analysis of large inclusions and anisotropic inclusions was limited due to unstable growth arising from a combination of the heterogeneous structure and the limitations of the experimental surfing load condition.

Although no quantitative analysis could be performed, the potential of anisotropy is still apparent for cases of biased or directional loading. Because toughening is governed by the elastic contrast and local structure of the interface, it is possible to make anisotropic inclusions structures that mitigate crack propagation similarly to isotropic ones as long as loading is biased in one particular direction. The benefit of the anisotropy in this case is that the anisotropic heterogeneities use a significantly smaller volume fraction of inclusion phase, making them much more favorable for retention of bulk matrix properties, which is desirable in structural ceramics or ceramic systems designed for engine environments.

REFERENCES

[1] N. R. Brodnik, C. J. Hsueh, and M. T. Johnson. A nonconstraining templated powder grid for measurement of strain. *Strain*, 2018. ISSN 14751305. doi: 10.1111/str.12273.

[2] N. R. Brodnik, C.-J. Hsueh, K. Bhattacharya, B. Bourdin, K.T. Faber, and G. Ravichandran. Guiding and trapping cracks with compliant inclusions for enhancing toughness of brittle composite materials. *Submitted to Journal of Applied Mechanics*, 2019.

[3] M Y He and J W Hutchinson. Crack Deflection at an Interface Between Dissimilar Elastic-Materials. *Int J Solids Struct*, 25(9):1053–1067, 1989.

[4] Brian R. Lawn. *Fracture of brittle solids*. Cambridge University Press, 1993. ISBN 9780511623127.

[5] M. Z. Hossain, C. J. Hsueh, B. Bourdin, and K. Bhattacharya. Effective toughness of heterogeneous media. *Journal of the Mechanics and Physics of Solids*, 71(1):15–32, 2014. ISSN 00225096. doi: 10.1016/j.jmps.2014.06.002. URL http://dx.doi.org/10.1016/j.jmps.2014.06.002.

[6] C.-J. Hsueh. Effective toughness of heterogeneous materials. *PhD Thesis, California Institute of Technology*, 2017.

[7] AutoDesk. Autodesk Standard Clear PR48 Formulation. https://cdn-standard3.discourse.org/uploads/autodesk/original/1X/1b755fa09bb75aae7395f2ffccd444c68b06f3ba.pdf, 2017. [Online; accessed 10-June-2017].

[8] K.T. Faber and A.G. Evans. Crack deflection processes—I. Theory. *Acta Metallurgica*, 31(4):565–576, apr 1983. ISSN 0001-6160. doi: 10.1016/0001-6160(83)90046-9. URL https://www.sciencedirect.com/science/article/pii/0001616083900469.

[9] Neng Wang and Shuman Xia. Cohesive fracture of elastically heterogeneous materials: An integrative modeling and experimental study. *Journal of the Mechanics and Physics of Solids*, 98:87–105, jan 2017. ISSN 0022-5096. doi: 10.1016/J.JMPS.2016.09.004. URL https://www.sciencedirect.com/science/article/pii/S0022509616303313.

[10] Owen Smithyman. Ember Standard Clear - Mechanical Properties. http://forum.ember.autodesk.com/t/ember-standard-clear-mechanical-properties/71/2, 2016. [Online; accessed 10-June-2017].

[11] H. Moulinec and P. Suquet. A fft-based numerical method for computing the mechanical properties of composites from images of their microstructures. In *IUTAM Symposium on Microstructure-Property Interactions in Composite Materials*, pages 235–246. Springer, 1995.

[12] H. Moulinec and P. Suquet. A numerical method for computing the overall response of nonlinear composites with complex microstructure. *Computer methods in applied mechanics and engineering*, 157(1-2):69–94, 1998.

[13] J.C. Michel, H. Moulinec, and P. Suquet. A computational scheme for linear and non-linear composites with arbitrary phase contrast. *International Journal for Numerical Methods in Engineering*, 52(1-2):139–160, 2001.

[14] James R Rice. Mathematical Analysis in the Mechanics of Fracture. Technical report, 1968. URL http://esag.harvard.edu/rice/018{_}Rice{_}MathAnalMechFract{_}68.pdf.

[15] Michel Grédiac. The use of full-field measurement methods in composite material characterization: interest and limitations. *Composites Part A: Applied Science and Manufacturing*, 35(7-8):751–761, jul 2004. ISSN 1359835X. doi: 10.1016/j.compositesa.2004.01.019. URL http://linkinghub.elsevier.com/retrieve/pii/S1359835X04000260.

[16] Frank C Demarest. High-resolution, high-speed, low data age uncertainty, heterodyne displacement measuring interferometer electronics. *Measurement Science and Technology*, 9(7):1024–1030, jul 1998. ISSN 0957-0233. doi: 10.1088/0957-0233/9/7/003. URL http://stacks.iop.org/0957-0233/9/i=7/a=003?key=crossref.7a9b270bed78db7ab79a4909ced2fcec.

[17] Hareesh V. Tippur, Sridhar Krishnaswamy, and Ares J. Rosakis. Optical mapping of crack tip deformations using the methods of transmission and reflection coherent gradient sensing: a study of crack tip K-dominance. *International Journal of Fracture*, 52(2):91–117, 1991. ISSN 0376-9429. doi: 10.1007/bf00032372. URL https://link.springer.com/article/10.1007{\%}2FBF00032372?LI=true.

[18] Vasco Ronchi. Forty Years of History of a Grating Interferometer. *Applied Optics*, 3(4):437, apr 1964. ISSN 0003-6935. doi: 10.1364/AO.3.000437. URL https://www.osapublishing.org/abstract.cfm?URI=ao-3-4-437.

[19] H. Lee and S. Krishnaswamy. A compact polariscope/shearing interferometer for mapping stress fields in bimaterial systems. *Experimental Mechanics*, 36 (4):404–411, dec 1996. ISSN 0014-4851. doi: 10.1007/BF02328585. URL http://link.springer.com/10.1007/BF02328585.

[20] T. C. Chu, W. F. Ranson, and M. A. Sutton. Applications of digital-image-correlation techniques to experimental mechanics. *Experimental Mechanics*, 25(3):232–244, sep 1985. ISSN 0014-4851. doi: 10.1007/BF02325092. URL http://link.springer.com/10.1007/BF02325092.

[21] H. A. Bruck, S. R. McNeill, M. A. Sutton, and W. H. Peters. Digital image correlation using Newton-Raphson method of partial differential correction. *Experimental Mechanics*, 29(3):261–267, sep 1989. ISSN 0014-4851. doi: 10.1007/BF02321405. URL http://link.springer.com/10.1007/BF02321405.

[22] Bing Pan, Kemao Qian, Huimin Xie, and Anand Asundi. Two-dimensional digital image correlation for in-plane displacement and strain measurement: a review. *Measurement Science and Technology*, 20(6):062001, jun 2009. ISSN 0957-0233. doi: 10.1088/0957-0233/20/6/062001. URL http://stacks.iop.org/0957-0233/20/i=6/a=062001?key=crossref.37cf26a6947e54eb5498e67742a4e2ad.

[23] J. C. Wyant. Double Frequency Grating Lateral Shear Interferometer. *Applied Optics*, 12(9):2057, sep 1973. ISSN 0003-6935. doi: 10.1364/AO.12.002057. URL https://www.osapublishing.org/abstract.cfm?URI=ao-12-9-2057.

[24] F. P. Chiang and A. Asundi. White light speckle method of experimental strain analysis. *Applied Optics*, 18(4):409, feb 1979. ISSN 0003-6935. doi: 10.1364/AO.18.000409. URL https://www.osapublishing.org/abstract.cfm?URI=ao-18-4-409.

[25] MA Sutton, WJ Wolters, WH Peters, WF Ranson, and SR McNeill. Determination of displacements using an improved digital correlation method. *Image and Vision Computing*, 1(3):133–139, aug 1983. ISSN 02628856. doi: 10.1016/0262-8856(83)90064-1. URL http://linkinghub.elsevier.com/retrieve/pii/0262885683900641.

[26] Sven Bossuyt. Optimized Patterns for Digital Image Correlation. pages 239–248. Springer, New York, NY, 2013. doi: 10.1007/978-1-4614-4235-6_34. URL http://link.springer.com/10.1007/978-1-4614-4235-6{_}34.

[27] G.F. Bomarito, J.D. Hochhalter, T.J. Ruggles, and A.H. Cannon. Increasing accuracy and precision of digital image correlation through pattern optimization. *Optics and Lasers in Engineering*, 91:73–85, apr 2017. ISSN 01438166. doi: 10.1016/j.optlaseng.2016.11.005. URL http://linkinghub.elsevier.com/retrieve/pii/S0143816616304110.

[28] M. Grédiac, F. Sur, and B. Blaysat. The Grid Method for In-plane Displacement and Strain Measurement: A Review and Analysis. *Strain*, 52(3):205–243, jun 2016. ISSN 00392103. doi: 10.1111/str.12182. URL http://doi.wiley.com/10.1111/str.12182.

[29] J Tracy, A Waas, and S Daly. Experimental assessment of toughness in ceramic matrix composites using the j-integral with digital image correlation part i: methodology and validation. *Journal of Materials Science*, 50(13):4646–4658, 2015.

[30] Vincent J. Parks. The grid method. *Experimental Mechanics*, 9(7):27–33, jul 1969. ISSN 0014-4851. doi: 10.1007/BF02325141. URL http://link.springer.com/10.1007/BF02325141.

[31] Vincent J. Parks. Strain Measurement Using Grids. *Optical Engineering*, 21(4):633–639, aug 1982. ISSN 0091-3286. doi: 10.1117/12.7972958. URL http://opticalengineering.spiedigitallibrary.org/article.aspx?doi=10.1117/12.7972958.

[32] R Sowerby, E Chu, and J L Duncan. Determination of large strains in metalforming. *The Journal of Strain Analysis for Engineering Design*, 17(2):95–101, apr 1982. ISSN 0309-3247. doi: 10.1243/03093247V172095. URL http://journals.sagepub.com/doi/10.1243/03093247V172095.

[33] D. W. Manthey and D. Lee. Recent developments in a vision-based surface strain measurement system. *JOM*, 47(7):46–49, jul 1995. ISSN 1047-4838. doi: 10.1007/BF03221231. URL http://link.springer.com/10.1007/BF03221231.

[34] Y. Morimoto, Y. Seguchi, and T. Higashi. Strain analysis by mismatch moire method and grid method using Fourier transform. *Computational Mechanics*, 6(1):1–10, 1990. ISSN 0178-7675. doi: 10.1007/BF00373795. URL http://link.springer.com/10.1007/BF00373795.

[35] Shengnan Sun, Michel Grédiac, Evelyne Toussaint, Jean-Denis Mathias, and Narimane Mati-Baouche. Applying a Full-Field Measurement Technique to Characterize the Mechanical Response of a Sunflower-Based Biocomposite. *Experimental Mechanics*, 55(5):917–934, jun 2015. ISSN 0014-4851. doi: 10.1007/s11340-015-9988-1. URL http://link.springer.com/10.1007/s11340-015-9988-1.

[36] M.J. Hÿtch, E. Snoeck, and R. Kilaas. Quantitative measurement of displacement and strain fields from HREM micrographs. *Ultramicroscopy*, 74(3):131–146, aug 1998. ISSN 03043991. doi: 10.1016/S0304-3991(98)00035-7. URL http://linkinghub.elsevier.com/retrieve/pii/S0304399198000357.

[37] M.J. Hÿtch and T. Plamann. Imaging conditions for reliable measurement of displacement and strain in high-resolution electron microscopy. *Ultramicroscopy*, 87(4):199–212, may 2001. ISSN 03043991. doi: 10.1016/S0304-3991(00)00099-1. URL http://linkinghub.elsevier.com/retrieve/pii/S0304399100000991.

[38] Huimin Xie, Satoshi Kishimoto, Anand Asundi, Chai Gin Boay, Norio Shinya, Jin Yu, and Bryan K A Ngoi. In-plane deformation measurement using the atomic force microscope moiré method. *Nanotechnology*, 11(1):24–29, mar 2000. ISSN 0957-4484. doi: 10.1088/0957-

4484/11/1/305. URL http://stacks.iop.org/0957-4484/11/i=1/a=305?key=crossref.3625f95a7f67d2849060d7451d6024fe.

[39] Huimin Xie, Zhanwei Liu, Daining Fang, Fulong Dai, Hongjun Gao, and Yapu Zhao. A study on the digital nano-moiré method and its phase shifting technique. *Measurement Science and Technology*, 15(9): 1716–1721, sep 2004. ISSN 0957-0233. doi: 10.1088/0957-0233/15/9/007. URL http://stacks.iop.org/0957-0233/15/i=9/a=007?key=crossref.e2b1ff934d20c903ad76a862dc315266.

[40] J.-L. Piro and M. Grediac. PRODUCING AND TRANSFERRING LOW-SPATIAL-FREQUENCY GRIDS FOR MEASURING DISPLACEMENT FIELDS WITH MOIRE AND GRID METHODS. *Experimental Techniques*, 28(4):23–26, jul 2004. ISSN 0732-8818. doi: 10.1111/j.1747-1567.2004.tb00173.x. URL http://doi.wiley.com/10.1111/j.1747-1567.2004.tb00173.x.

[41] Rostand Moutou Pitti, Claudiu Badulescu, and Michel Grédiac. Characterization of a cracked specimen with full-field measurements: direct determination of the crack tip and energy release rate calculation. *International Journal of Fracture*, 187(1):109–121, may 2014. ISSN 0376-9429. doi: 10.1007/s10704-013-9921-5. URL http://link.springer.com/10.1007/s10704-013-9921-5.

[42] B Ribbens. Development and validation of a time-domain fringe pattern analysis technique for the measurement of object shape and deformation. *PhD Thesis, Vrije Universistat Brussel and Universitat Antwerpen*, 2015.

[43] Lorna J Gibson and Michael F Ashby. *Cellular Solids: Structure and Properties - Lorna J. Gibson, Michael F. Ashby - Google Books*. Cambridge University Press, 2 edition, 1997. ISBN 0 521 49911 9. URL https://books.google.com/books?hl=en{\&}lr={\&}id=rzVIBAAAQBAJ{\&}oi=fnd{\&}pg=PR7{\&}dq=gibson+ashby+cellular+solids+structure+and+properties+citation{\&}ots=gw5x9{_}7xBU{\&}sig=JBe66HXSx7{_}2pEbPAvsWC6rE0Fw{\#}v=onepage{\&}q{\&}f=false.

[44] Baikowski. Baikowski Malakoff HP DPM. http://www.baikowski.com/products, 2017. [Online; accessed 10-June-2017].

[45] G.A. Francfort and J.-J. Marigo. Revisiting brittle fracture as an energy minimization problem. *Journal of the Mechanics and Physics of Solids*, 46 (8):1319–1342, aug 1998. ISSN 0022-5096. doi: 10.1016/S0022-5096(98)00034-9. URL https://www.sciencedirect.com/science/article/pii/S0022509698000349.

[46] B. Bourdin, G.A. Francfort, and J-J. Marigo. Numerical experiments in revisited brittle fracture. *Journal of the Mechanics and Physics of Solids*, 48(4):797–826, apr 2000. ISSN 0022-5096. doi: 10.1016/S0022-5096(99)

00028-9. URL https://www.sciencedirect.com/science/article/pii/S0022509699000289.

[47] Blaise Bourdin, Gilles A. Francfort, and Jean-Jacques Marigo. The Variational Approach to Fracture. *Journal of Elasticity*, 91(1-3):5–148, apr 2008. ISSN 0374-3535. doi: 10.1007/s10659-007-9107-3. URL http://link.springer.com/10.1007/s10659-007-9107-3.

[48] G.P. Cherepanov. Crack propagation in continuous media: PMM vol. 31, no. 3, 1967, pp. 476–488. *Journal of Applied Mathematics and Mechanics*, 31(3):503–512, jan 1967. ISSN 0021-8928. doi: 10.1016/0021-8928(67)90034-2. URL https://www.sciencedirect.com/science/article/pii/0021892867900342.

[49] A. A. Griffith. The Phenomena of Rupture and Flow in Solids. *Philosophical Transactions of the Royal Society A: Mathematical, Physical and Engineering Sciences*, 221(582-593):163–198, jan 1921. ISSN 1364-503X. doi: 10.1098/rsta.1921.0006. URL http://rsta.royalsocietypublishing.org/cgi/doi/10.1098/rsta.1921.0006.

[50] O. Chiantore, L. Trossarelli, and M. Lazzari. Photooxidative degradation of acrylic and methacrylic polymers. *Polymer*, 41(5):1657–1668, mar 2000. ISSN 00323861. doi: 10.1016/S0032-3861(99)00349-3. URL http://linkinghub.elsevier.com/retrieve/pii/S0032386199003493.

Chapter 3

ANISOTROPIC STRUCTURE TO CONTROL NUCLEATION AND PROPAGATION: FRACTURE DIODES

The contents of this chapter are also presented in "Fracture Diodes: Directional Asymmetry of Fracture Toughness" by N.R. Brodnik, S. Brach, C.M. Long, K. Bhattacharya, B. Bourdin, K.T. Faber, and G. Ravichandran, which is currently in preparation. N.R. Brodnik led the experimental portion of the work, and was assisted by C.M. Long. S. Brach led the numerical simulations. Bhattacharya and Bourdin supervised the numerical simulations while Faber and Ravichandran supervised the experimental work. All authors were involved in discussing all aspects of the work, and preparing the manuscript.

3.1 Introduction

In the previous chapter, the effect of anisotropic structure on fracture properties was discussed in the context of the effect of inclusion structure on crack propagation. Surfing load experiments were used to provide stable crack growth, but all observations of mechanical response were made well within the crack propagation regime, and crack tip position was always readily identifiable. However, if designed anisotropy is to be suitable as a toughening mechanism in practical applications, the anisotropic structures must be able to function in scenarios where loading occurs well before macro-scale crack propagation has begun. This means exploring the effects of designed anisotropic structure on both nucleation and propagation of the crack.

The surfing load experiments explored in Chapter 2 provided a promising means to investigating designed anisotropy under stable crack growth conditions, but some characterization limitations arose when exploring anisotropic structures. The first limitation was related to crack pinning and subsequent unstable propagation events. Because load progression was displacement controlled, stability was lost during nucleation and renucleation events because the crack would arrest, but the sample would continue to be loaded as it travelled along the diverging rail. This load buildup led to sudden propagation events, where the crack would propagate too quickly to be properly characterized. The second limitation with the surfing load condition was related to directionality. Because the surfing load applies a controlled load from a single direction, anisotropic toughness can only be explored by directly

characterizing and comparing the toughness values of anisotropic structures from different orientations, which can prove difficult due to the already mentioned crack pinning and unstable propagation.

The focus of this chapter is to demonstrate the influence of designed directional asymmetry on bulk fracture under loading scenarios that do not require stable growth of a preexisting crack. These scenarios were investigated by changing the loading condition to be unbiased, and exploring failure from a phenomenological standpoint. Under unbiased loads, such as uniaxial tension, because failure is equally possible from multiple directions, the effect of structural asymmetry manifests through consistent fracture from a particular direction rather than as differences in fracture toughness. The possibility of this was suggested in numerical simulations by Hossain et al.[1] through the exploitation of material architecture that lacks mirror symmetry. Consistent directional failure under unbiased loading also inspired the name "fracture diodes" for specimens exhibiting this phenomenon. The current work explores the potential of this phenomenon through numerical simulation, and demonstrates it experimentally by realizing asymmetric microstructures through 3D printing of a brittle photopolymer.

3.2 Methods

3.3 Specimen Design

Since this investigation was centered on the mode and direction of the failure event rather than the measured toughness, the design for the fracture diode specimens was chosen to be relatively simple. The asymmetric inclusions were chosen to be triangles and the inclusion phase was chosen to be a void, rather than the partial changes in thickness used in the surfing load investigations. This meant that in addition to the voids acting as a compliant inclusion phase, any cracks that formed in the brittle polymer would have to renucleate out of each void, allowing for investigations into both nucleation and propagation. This simple arrangement of triangular voids was also well-suited to numerical investigation, as continuum simulations of a single phase with voids are not less computationally demanding than more complex structures. An example of a simulation domain and analogous printed specimen is shown in Figure 3.1.

Numerical Methods

Variational phase-field simulations Similar to the surfing load tests, crack propagation in the fracture diodes was investigated numerically through the variational

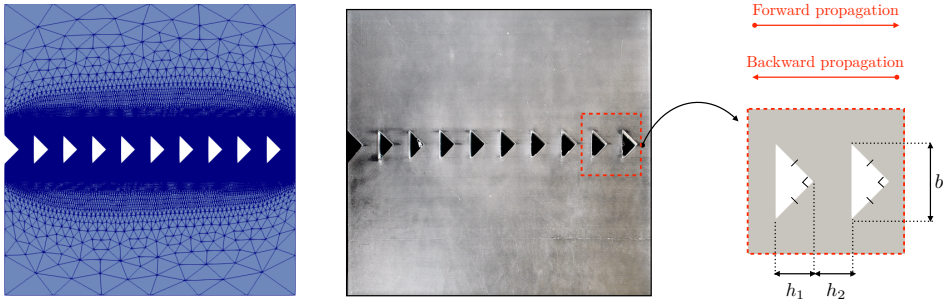

Figure 3.1: An example pattern of asymmetric triangular voids used for the numerical simulations (left) and experimental tests (middle). The inset (right) shows the relevant geometrical parameters of the triangular voids as well as the directions of crack propagation considered in this study, labeled here as 'forward' and 'backward' with respect to void orientation.

fracture approach developed by Bourdin et al.[2, 3] For these numerical analyses, the photopolymer system was treated as a perfectly-brittle elastic material. The crack propagates through this established domain as a damage phase rather than a strict discontinuity, with completely damaged phase being unable to bear any load. Within this domain, the brittle phase through which the crack travels is discretized into a mesh structure and the crack has an established nucleation length which describes both its half-width and the minimum discrete length over which it can nucleate or propagate. The mesh structure used to describe the homogeneous brittle phase is chosen to be much smaller than the characteristic nucleation length in the area around the inclusions, but is then coarsened away from the inclusions for computational efficiency. An example mesh is shown in Figure 3.1.

The fracture problem is solved by alternatively minimizing the total energy functional with respect the two state variables, which are the damage phase and the displacement. The constrained minimization with respect to the damage phase is implemented using the variational inequality solvers provided by `PETSc` [4–6], whereas the minimization with respect to displacement field is a linear problem, solved by using preconditioned conjugated gradients. All computations are performed by means of the open source code `mef90`[1].

All equations used in the numerical analyses are non-dimensionalized, and geometrical parameters are chosen to match the experimental configurations chosen for the printed diode structures.

[1] Available at `https://www.bitbucket.org/bourdin/mef90-sieve`.

Numerical Load Configurations The focus of this investigation was to look at the phenomenological aspects of failure and evaluate how designed anisotropy could influence failure mode under unbiased load. In this study, the unbiased load was chosen to be uniaxial tension because it is relatively simple to apply both numerically as well as experimentally. However, tensile load produces unstable crack growth, which can prove difficult to evaluate in extremely brittle materials. In the case of the ideally brittle and purely elastic material system used in numerical simulations, the unstable aspect of tension proved to be a significant challenge because the entire brittle system would fail within a single time step, making observation of the directionality of failure infeasible. Attempts were made to introduce both numerical and material viscosity into the system to slow the crack, but these proved ineffective.

Despite this difficulty, the numerical simulations still have the benefit of much easier design adjustment and mechanical evaluation over the actual experiment. Therefore, it proved sensible to adjust the load configuration in the numerical analysis to allow for slower, more stable crack propagation and use a more formal evaluation technique to justify the expected failure phenomena in the uniaxial tension experiments. For this reason, all numerical experiments were done under the surfing load conditions used in Chapter 2, and the macroscopic effective toughnesses of different orientations were evaluated using the J-integral. These J-integral values were used as a basis for assessing which failure modes were favorable and unfavorable within the diode specimens.

Evaluation of effective toughness As previously discussed, there does not formally exist any theoretical homogenization model able to predict the effective toughness of heterogeneous media. However, using a conceptual extension of classical fracture mechanics theories [7–9], it is reasonable to define the macroscopic resistance to fracture as the maximum value of the far-field energy-release rate as the crack propagates throughout the material. [1, 10]

At each time step, the driving force necessary to sustain the macroscopic crack propagation is determined by computing the energy-release rate using the J-integral at the domain boundary.[7, 9] Therefore, the effective fracture toughness is defined as the energy needed to propagate the crack over a macroscopic distance. This corresponds to the peak value of the energy-release rate, that is, the maximum value of the J-integral over time. This is analogous to the far field J-Integral approach used in Chapter 2, although for this investigation, it is only done in the numerical

assessment to provide a formal basis for what failure modes should be favorable or unfavorable under the unbiased load of uniaxial tension. Using this combination of surfing load for stable crack growth and macroscopic far-field J-integral, a suitable basis can be established for what types of failure are energetically favorable and would therefore be expected in uniaxial tension experiments.

Experimental Methods

Sample Fabrication For the experimental tests, samples were printed using digital light processing (DLP) printing on an Autodesk Ember 3D Printer (Autodesk, San Rafael, CA). Samples were made from commercially available Standard Clear PR48 printing resin, a urethane acrylate photopolymer. To keep comparisons of void arrangements as consistent as possible, all voids were kept to a standard size and structure, namely isosceles right triangles with a vertical hypotenuse which has a fixed length of 3 mm, as shown in Figure 3.2. Similar to the anisotropic inclusions discussed in Chapter 2, the effect of anisotropy should be visible in inclusions of any size scale, so the only factor limiting the size of the triangular voids is the resolution at which anisotropic geometries can be produced. For this study, the triangle size was chosen to make both sample fabrication and failure observation straightforward. This size scale is also well suited to the overall size of the specimen, as each void has a vertical length of 3mm and a horizontal width of 1.5 mm, which scale nicely as clean fractions of the specimen gauge length and width. All specimens tested had a gauge length of 60 mm, with gauge width changing slightly between 28.5 and 31.5 mm depending on design, to preserve symmetry.

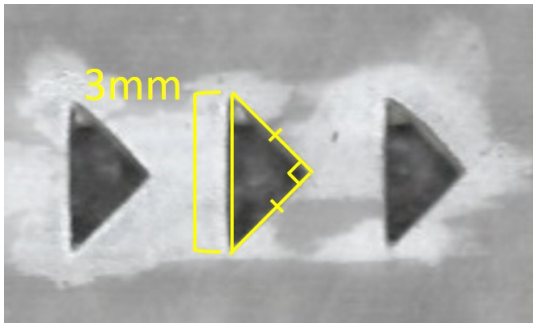

Figure 3.2: Close-up dimensioned view of void pattern used in the printed diode structures, showing the exact size of the isosceles triangle voids.

Using this 3 mm tall, 1.5 mm wide isosceles triangle void design as a standard, a variety of heterogeneous structures were developed to investigate the effect on failure behavior of different structural arrangement parameters, such as void spacing,

angle and direction. First, to investigate the influence of spacing, samples with a single row of unidirectional triangular voids were printed with the voids at different incremental spacing. To look at the effects of void direction on failure behavior, additional designs were printed with bidirectional arrangements of voids that pointed outward from the center of the specimen. To investigate the effects of nucleation and the role of the edge notch, unidirectional specimens were printed both with and without symmetric edge notches. Unidirectional and bidirectional samples shown in Figure 3.3 had a gauge width of 30 mm, while specimens with no edge notch shown in Figure 3.4(a-c) had a gauge width of 28.5 mm and specimens with two edge notches shown in Figure 3.4(d-f) had a gauge width of 31.5 mm. Finally, using the knowledge provided from the failure distributions of these designs, a final design was printed with a custom inclusion morphology and spacing distribution, which was designed to maximize anisotropic fracture behavior.

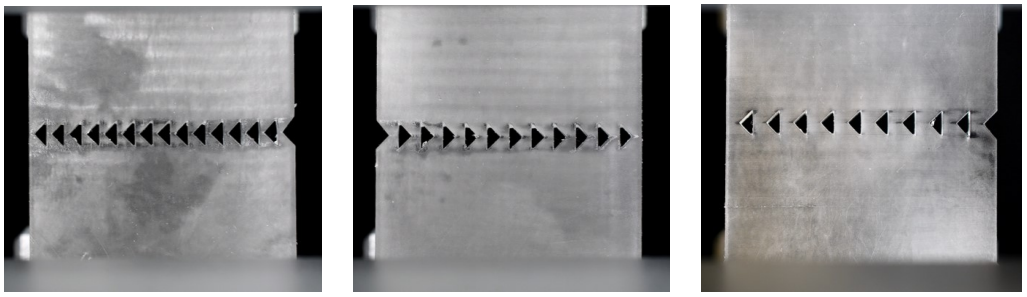

(a) Unidirectional: 0.5 mm Spacing

(b) Unidirectional: 1.0 mm Spacing

(c) Unidirectional: 1.5 mm Spacing

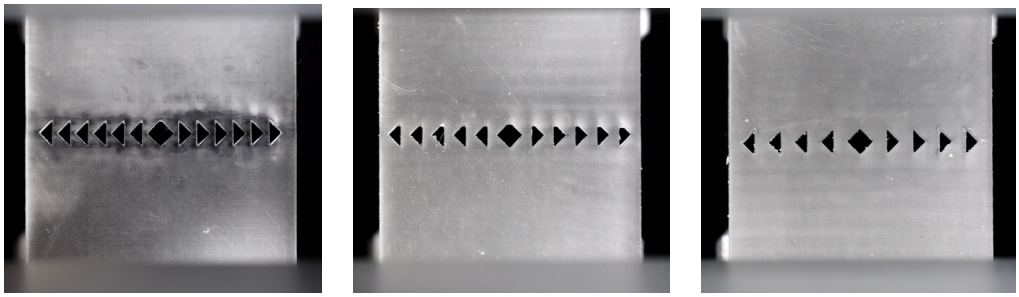

(d) Bidirectional: 0.5 mm Spacing

(e) Bidirectional: 1.0 mm Spacing

(f) Bidirectional: 1.5 mm Spacing

Figure 3.3: Images showing the unidirectional single-notch (a-c) and bidirectional (d-f) designs investigated to understand orientation dependence. Gauge width for all specimens shown is 30 mm.

Accounting for Material Variability Across each of the aforementioned configurations, much consideration had to be given to what aspects of mechanical response could be suitably measured and compared across different configurations.

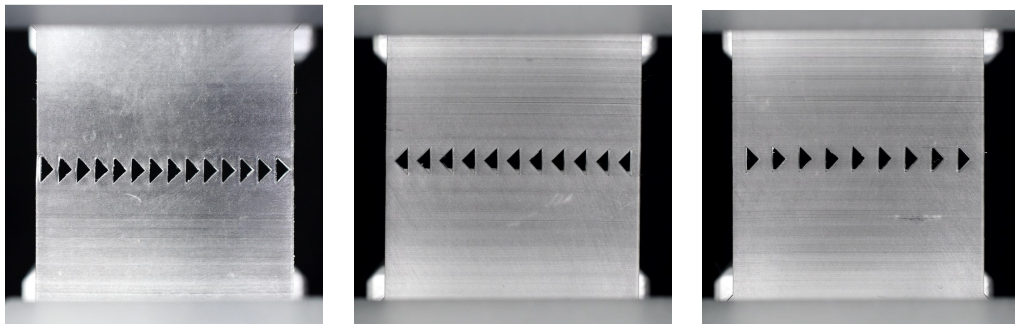

(a) Unidirectional No Notch: 0.5 mm Spacing

(b) Unidirectional No Notch: 1.0 mm Spacing

(c) Unidirectional No Notch: 1.5 mm Spacing

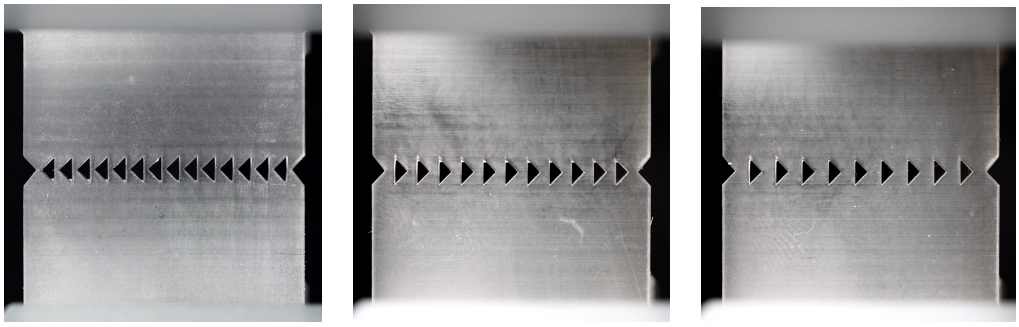

(d) Unidirectional Double Notch: 0.5 mm Spacing

(e) Unidirectional Double Notch: 1.0 mm Spacing

(f) Unidirectional Double Notch: 1.5 mm Spacing

Figure 3.4: Images showing unidirectional no notch (a-c) and unidirectional double notch (d-f) designs investigated to understand edge notch dependence. The gauge width for specimens (a-c) is 28.5 mm and the gauge with for specimens (d-f) is 31.5 mm to preserve symmetry.

Because samples are composed of a brittle photopolymer, it is critical to distinguish mechanical variations due to material response from variations due to difference in the structure or positioning of voids. To minimize the influence of the material on mechanical response, samples were printed using relatively uniform print exposure times (2.2-3.0 seconds per exposure) and were not treated with a UV post-cure. This helped ensure that all samples tested had relatively comparable amounts of UV cross-linking at time of testing. Additionally, all samples were tested within one hour after printing to minimize any embrittlement or bleaching from photo-oxidation.

Mechanical Testing Testing was done on an Instron 5892 (Instron, Norwood, MA) load frame at a constant displacement rate of 1 mm/min and different replicates of each sample type were rotated and mirrored in different ways to ensure that no bias was introduced due to the innate directionality of the DLP printing process. For each arrangement of inclusions, a minimum of 30 replicates were tested. Within

these arrangements, a minimum of 8 replicates were tested for each spacing, with the exception of double notch samples with 1 mm spacing, which only had 4 replicates due to printing errors.

For each test, the load and displacement were recorded using from the load cell and the failure behavior of the sample itself was recorded with a Nikon D7500 (Nikon, Tokyo, Japan) digital camera at a rate of 30 frames per second. Recording was started just before the beginning of load application so that loading data and video could be synchronized through visible failure events.

After testing, video recordings of failure were then reviewed frame-by-frame using the post production film software DaVinci Resolve (Blackmagic Design, Port Melbourne, Australia) to classify their failure behavior and compare with the failure modes predicted by numerical simulation.

3.4 Mechanics of Diode Failure

Numerical Computations

Numerical investigation of directionality is done using the surfing load condition, which limits instantaneous crack growth and unstable snap-throughs. This setting promotes the quasi-static interaction between the crack set and the holes, thus highlighting the occurrence of directionality effects.

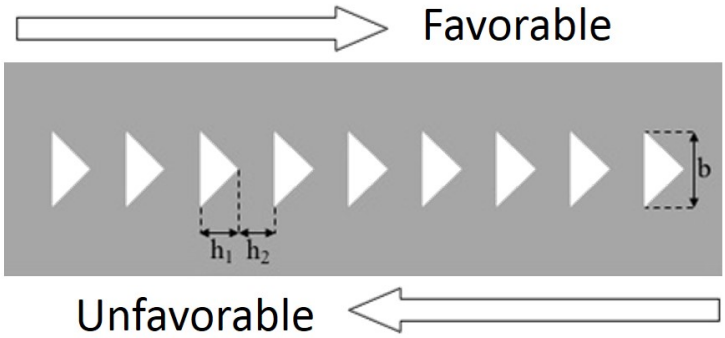

Figure 3.5: Schematic void pattern showing triangle dimensions as well as forward and backward propagation directions.

Consider a specimen with a row of triangular holes as shown in Figure 3.5. The geometry of the voids is expressed in terms of the triangle height, b, triangle spacing, h_1, and triangle width, h_2. First, the specimen is loaded with a surfing boundary condition to macroscopically drive crack propagation in the 'forward' direction, that is from the left to the right side of the specimen. The results in Figure 3.6 show that

the crack nucleates at the left notch and rapidly propagates afterwards until it reaches the first triangular hole. The crack then gets pinned at the triangular hole until it renucleates at the tip and continues to propagate in a left-to-right sense. It should be noted that, although significant damage buildup is observed at the triangle tip, when fracture does occur, each ligament instantaneously fractures without any preferred orientation at the local length-scale. Overall, though, the crack is observed to macroscopically propagate in the forward direction, following the applied boundary condition.

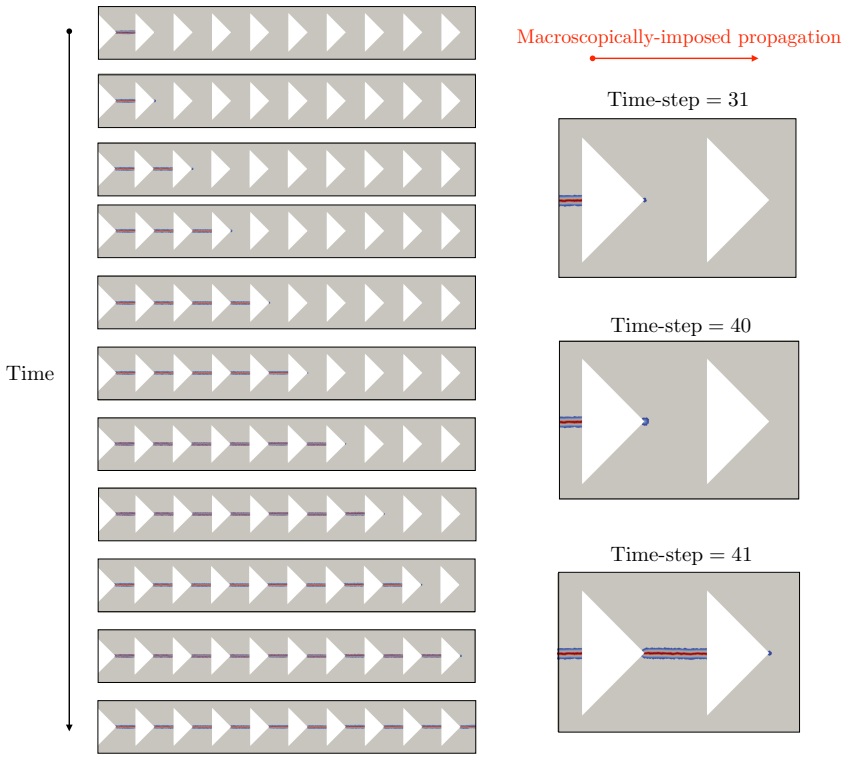

Figure 3.6: Numerical computations showing crack propagation in the forward, or favorable, direction. Left: crack path computed at different timesteps. Right: close-up view of the snapshots of the simulation showing the damage field when a crack is pinned at the hole; note that the damage always initiates at the tip of the triangular hole.

The second numerical experiment is performed by flipping the specimen with respect to the direction imposed for crack propagation by virtue of the placement of the edge notch, as shown in Figure 3.7. In other words, the biased load is now macroscopically driving the crack in the 'backward' direction, that is from the right side to the left side of the original configuration. Note that even though the triangular holes within the domain are mirrored, the edge notch is preserved to allow for identical nucleation

behavior between configurations and ensure that the ‘forward’ and ‘backward’ analysis are directly comparable. Results in Figure 3.7 show that the crack rapidly grows through the specimen, by getting pinned and subsequently renucleating at each triangle. Similar to the ‘forward’ case, failure within each solid segment between voids is unstable and instantaneous, but when the crack becomes pinned at a hole, damage buildup can be seen at the tip of the triangle at the next hole. This effect is clearly visible on the rightmost triangle at time step 75 in Figure 3.7. This suggests that in the case of ’backward’ propagation, the crack may be locally propagating from right to left, despite macroscopic failure occurring from left to right.

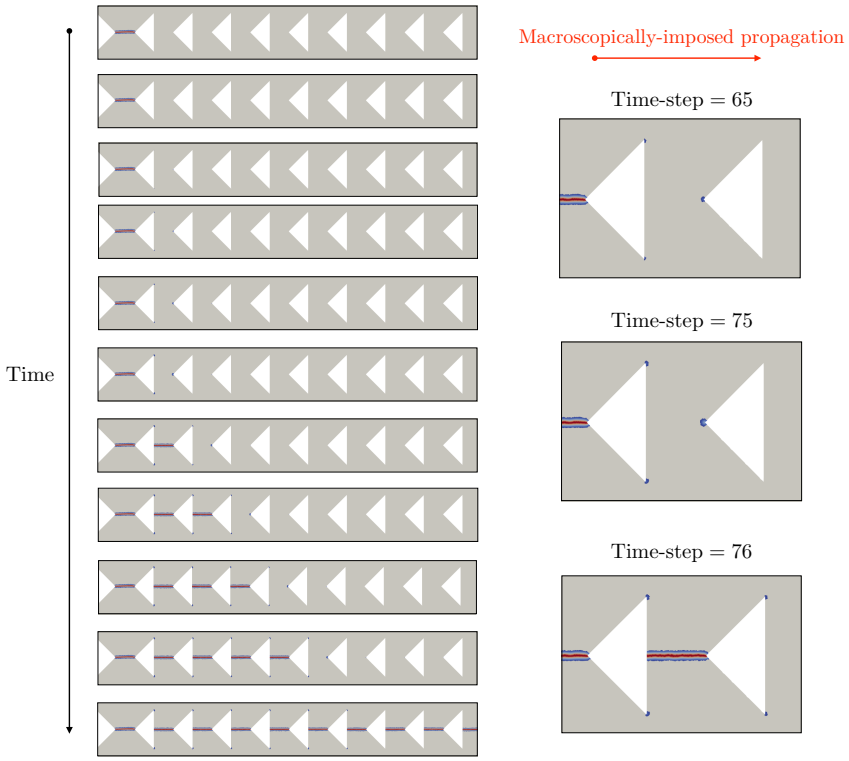

Figure 3.7: Numerical computations showing crack propagation in the backward, or unfavorable, direction. Left: crack path computed at different timesteps. Right: close-up view of the snapshots of the simulation showing the damage field when a crack is pinned at the hole; note that the damage initiates at the tip of the next consecutive triangular hole beyond the pinning site.

In both of these analyses, the driving force necessary to sustain the macroscopic crack propagation is determined by computing the energy-release rate, or J-integral, at the boundary of the specimen.[7, 9] Figure 3.8 shows the evolution of the J-integral as the crack progresses either in the forward or in the backward direction. The J-integral oscillates as the crack interacts with consecutive heterogeneities, with peak

values occurring just before unstable propagation through each solid segment. This oscillation also validates the argument that macroscopic toughness of a composite is based on the peak value of the energy release rate, as this peak value must be reached in order for the crack to propagate over macroscopic distances. As such, the maximum value of the J-integral over the duration of propagation determines the effective fracture toughness of each configuration, and these values are reported in Table 3.1. It should also be noted that, apart from small transient effects well below peak toughness near time t = 0, results are independent of the presence of the initial notch.

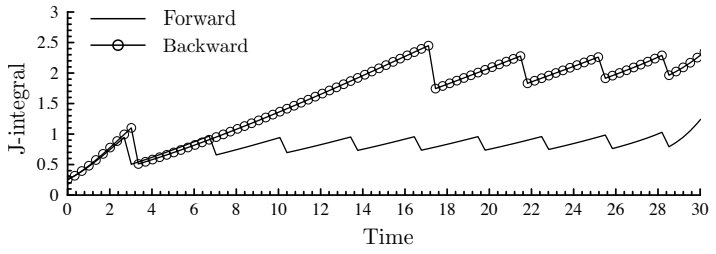

(a)

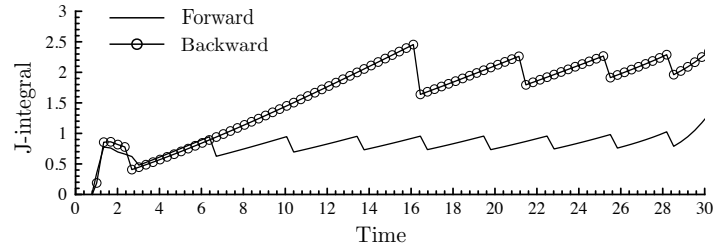

(b)

Figure 3.8: Numerical computations. Evolution of the J-integral with time as the crack is propagated through the specimens shown in Figures 3.6 (a) and 3.7 (b) with $h_1 = h_2$.

Following this procedure, effective toughness values determined for specimens with various spacings h_2 are shown in Table 3.1, expressed as a function of hole width h_1. All numerically determined toughness values are normalized with respect to the toughness of the intact material which has a J-integral value of 1. When $h_1 = h_2$, the effective toughness has a normalized value of 0.963 when propagating forward, which is far lower than the value of 2.27 in the backward direction. This trend of toughness in the forward direction being lower than the backward holds true regardless of spacing, though the difference in magnitude between the two directions varies with different spacings. It is straightforward to conclude that the resistance to

Table 3.1: Numerical computations. The computed effective toughness, that is, the maximum toughness value measured in the J-integral over the entire time duration, is shown in Figure 3.1 for both the forward and backward directions for various spacings h_2. The results are normalized with respect to the toughness of the uniform material, which is set to be J = 1.

	$h_2 = 4h_1$	$h_2 = 2h_1$	$h_2 = h_1$	$h_2 = h_1/2$	$h_2 = h_1/4$
Forward	1.4418	1.2550	0.9630	0.6712	0.4556
Backward	3.2765	3.1065	2.2692	1.1295	0.5906

crack propagation is asymmetric and depends on the sense of propagation, with the favorable growth direction being the 'forward' direction, and the unfavorable growth direction being the 'backward' direction.

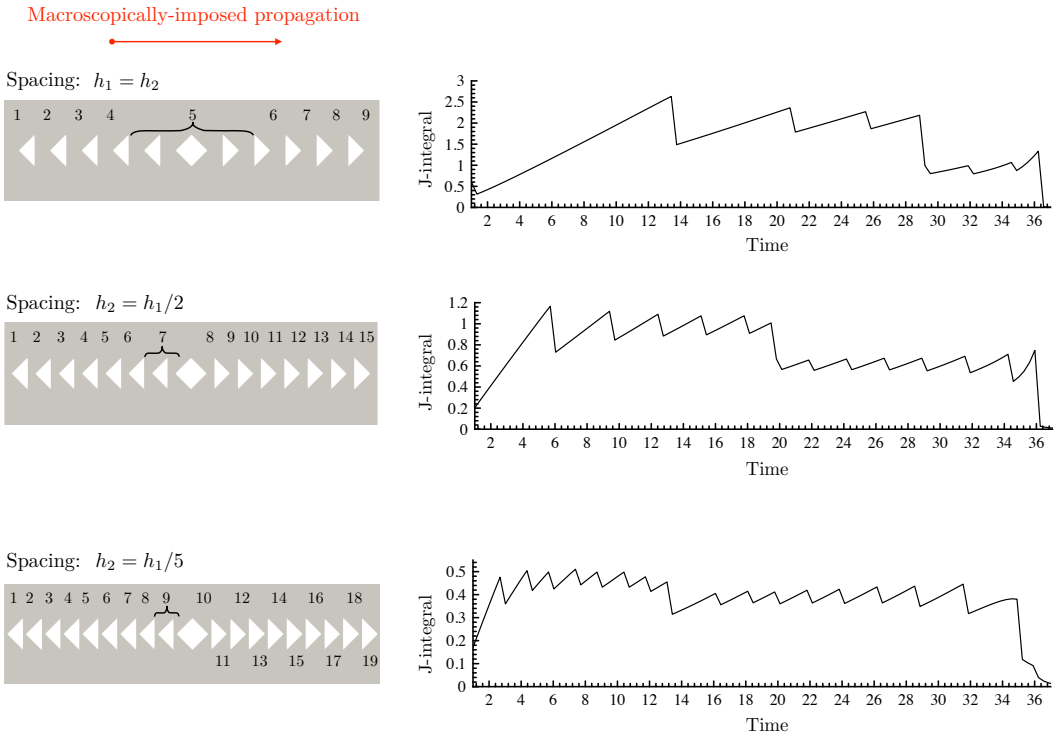

Figure 3.9: Numerical computations for bidirectional fracture diodes: crack paths and J-integrals shown for various values of spacing h_2. Numbers indicate the sequential failure of individual ligaments.

In the numerical analysis of bidirectional arrangements, the directional dependence on void orientation is present in a manner similar to that of the unidirectional arrangements, but some challenges arise due to the bias introduced by the surfing load condition. The computed crack path and J-integral are shown in Figure 3.9 for

various values of the spacing h_2 while the size h_1 of the heterogeneity is kept constant. The surfing condition introduces bias here by forcing the crack to nucleate at the left side of the specimen, resulting in the first half of the specimen exhibiting unfavorable propagation and the second half of the specimen exhibiting favorable propagation. Initially, propagation is unfavorable, as the crack gets pinned at each hole and it has to renucleate at the tip of the next void in order to continue propagating. This behavior continues until the crack approaches the symmetry axis of the specimen, beyond which the voids are oriented in a manner favorable for crack growth. The evolution of the energy-release rate over time clearly shows the sequential rapid propagation events that occur in this fracture process (see Figure 3.9). The transition from unfavorable to favorable orientation of heterogeneities is accompanied by a sudden drop in the macroscopic driving force, which demonstrates clearly the preferential direction of propagation. By extension, it is logical to conclude that under unbiased load, it would be expected for crack growth to occur along the toughness-minimizing path, which would be symmetric propagation outward from the middle of the specimen to each of the two edges.

Regardless of void arrangement, the origin of this asymmetry in effective toughness is fundamentally the lack of mirror symmetry in the void structure. As the crack is driven in the favorable growth direction, it is pinned by each new void, but a new crack can nucleate relatively easily at the tip of the triangular hole, allowing for straightforward propagation. In the unfavorable growth direction, the crack is similarly pinned at each void, but it is difficult for renucleation to occur along the flat edge opposite the triangle tip. This is not surprising, as it is known (e.g., [10, 11]) that cracks have difficulty in renucleating at interfaces where there is a sudden change in elastic modulus. Thus, it requires less energy for the crack to nucleate at the next hole (see Figure 3.7) and to propagate backwards into the current triangular void. As a consequence, the driving force needed to macroscopically drive crack propagation is higher for the unfavorable case.

Experiments

Before different void arrangements can be compared experimentally, it is important to verify that changes in void orientation and arrangement do not dramatically alter the elastic response of the system under uniaxial tension, which would introduce unwanted biases into the failure analysis. To assess this, displacement at the initial failure event in each sample was measured and plotted against the load measured at this first failure event. This relationship is a good indicator of material compliance,

and if the compliance is relatively uniform across replicates and designs, the failure stresses should follow a linear pattern. A plot of failure stress versus time to failure is shown in Figure 3.10.

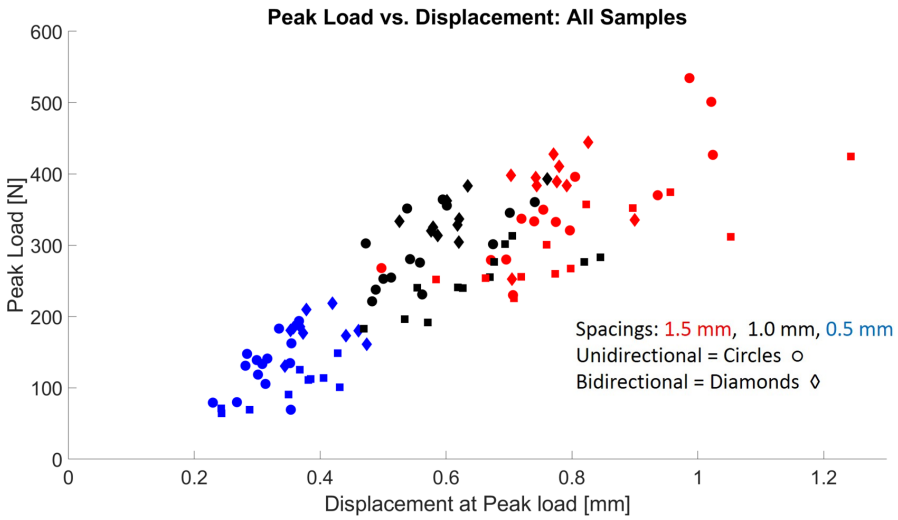

Figure 3.10: Plot of Peak Load versus Displacement for the different void arrangements analyzed in this study.

Although there is some variation, the general pattern of compliance is linear across all specimens. It should be noted that although the peak load reported in Figure 3.10 is not a perfect indicator of the stress state in the sample due to the presence of heterogeneous structure, this was still deemed reasonable under the premise that the specimens would behave like an isostress composite with a thin soft layer (the region containing voids) sandwiched between two thicker stiff layers. Because the stiff layers are much thicker, it was expected that their elastic behavior dominates, so the arrangement of the voids would not have significant effect on compliance. In other words, the elastic behavior of the specimens would be governed by the homogeneous regions, and the failure behavior would be governed by the heterogeneous regions.

During mechanical testing, all specimen failure modes were classified into three mutually exclusive groups. Specimen failure was classified as ‘favorable’ if fracture followed the direction of convergence of the triangular inclusions, consistent with the low toughness pattern predicted by numerical simulations. Analogously, behavior was termed ‘unfavorable’ when the sample failed in the exact opposite of the predicted sequence. Finally, sample failure is ‘random’ if there was no real pattern to failure or if specimen failure occurred too rapidly to be characterized from video recording. Schematic images of ‘expected’ failure behavior in unidirectional and bidirectional

void arrangements are shown in Figure 3.11.

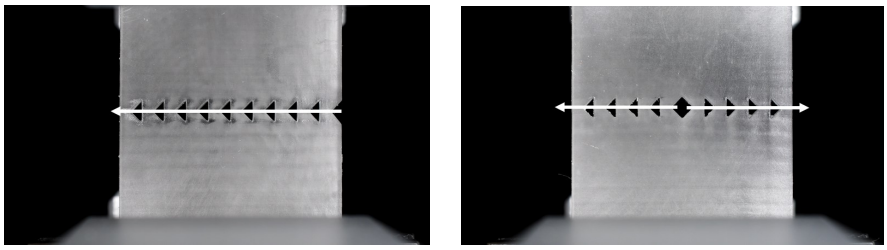

(a) Unidirectional Failure (b) Bidirectional Failure

Figure 3.11: Specimen images with overlayed arrows showing the favorable failure directions for (a) unidirectional, and (b) bidirectional designs.

Figure 3.12 shows a series of snapshots of the failure of a representative specimen that was classified as 'favorable'. The crack propagation is locally unstable, with the segments between voids failing rapidly, but the failure of each successive segment is delayed by the voids, which force renucleation into the next segment. Importantly, the crack propagates in the direction of convergence of the triangular voids, nucleating at the tip of each consecutive triangular void before continuing propagation. Additional SEM fractography shown in Figure 3.13 verifies that nucleation of the crack did occur at the tips of the triangular voids, as was predicted by numerical analyses. Furthermore, this directionally dependent behavior was somewhat resilient to the influence of precracking, as the formation of a single segment precrack on the opposite side of the specimen failed to alter the direction of the sequential events in some cases. Though weakest link failure mechanics still dominated the initial

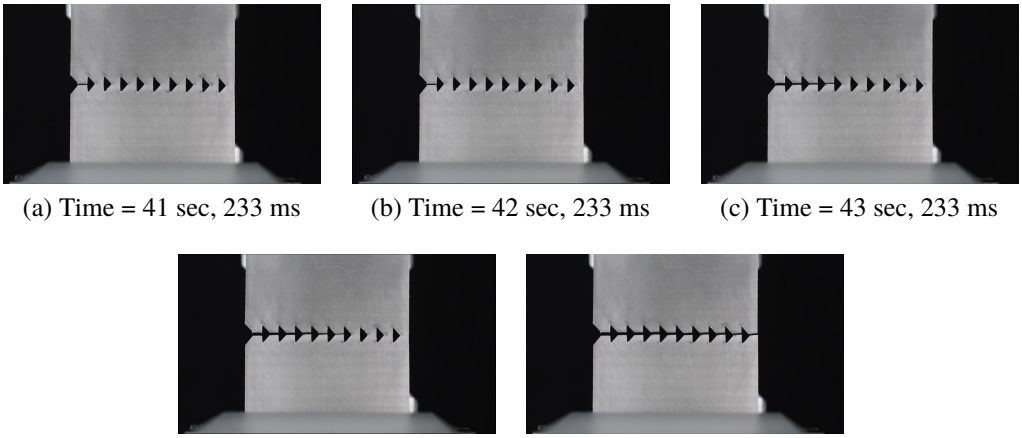

(a) Time = 41 sec, 233 ms (b) Time = 42 sec, 233 ms (c) Time = 43 sec, 233 ms

(d) Time = 44 sec, 233 ms (e) Time = 45 sec, 233 ms

Figure 3.12: Time lapse images showing the sequential failure behavior of a unidirectional specimen (mirrored for consistency). A time interval of 1 second passes between each photo in the sequence.

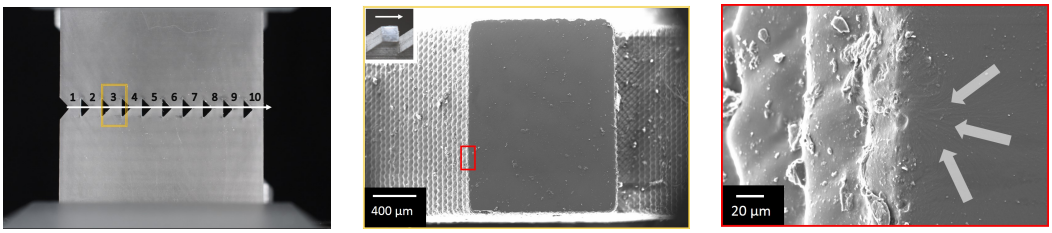

(a) Sample/Segment of Interest (b) Low Magnification SEM (c) High Magnification SEM

Figure 3.13: SEM fractography of a sample that failed in a favorable manner (a) based on simulation predictions, showing that fracture of each diode segment (b) nucleates from the tip of the triangular void inclusions (c). Inset in top left of (b) shows a representative fracture surface to indicate direction of global crack propagation with respect to SEM images.

failure of segments, the anisotropy of the voids inhibits propagation of the crack in one direction moreso than the other.

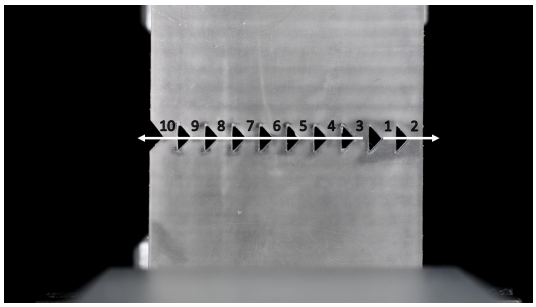

Figure 3.14: Image with a graphical overlay showing the unexpected failure of a unidirectional specimen. The failure events of individual segments are numbered in order from 1 to 10, with 1 being the first failure event and 10 being the last. White arrows indicate the direction of global crack propagation during failure.

Samples that failed in an 'unfavorable' manner also provide additional insight into fracture behavior in systems with directional anisotropy. A particular instance of unfavorable failure is shown in Figure 3.14. The critical defect in the system (as assessed post-fracture) happens to be near the far end of the sample where the crack would normally be expected to terminate. The exact nature of this defect is not clear, as it could be either a print defect or a variation in sharpness in the triangular inclusion at that location. Once the initial failure event occurs near the far right side, the crack propagates in the favorable direction until it reaches the free surface at the end of the sample. At this point, the extended macro-crack is the critical flaw in the system, and it is sufficiently large to drive the remainder of propagation backwards. This clearly demonstrates the trajectory dependence of fracture and how random nucleation events can lead to behavior that would typically be described as

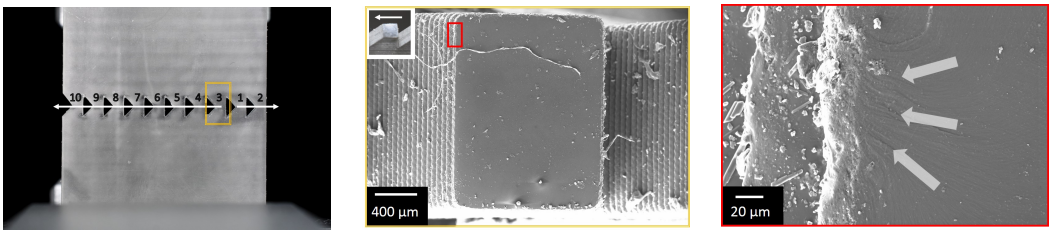

(a) Segment of Interest (b) Low Magnification SEM (c) High Magnification SEM

Figure 3.15: SEM fractography of a sample that failed in in an unexpected manner (a) based on simulation predictions. Even though global crack propagation is in the opposite direction, segment failure (b) still nucleates from the tip of the triangular void inclusions (c), so local failure propagates in the opposite direction of global failure. Inset in top left of (b) shows a representative fracture surface to indicate direction of global crack propagation with respect to SEM images.

unfavorable. Fractographic analysis shown in Figure 3.15 also demonstrates that even in the case of unfavorable propagation, numerical simulation still accurately predicts the local failure behavior, i.e., when the crack becomes trapped in a given void, it renucleates at the tip of the next consecutive triangular void, making local propagation occur in the opposite direction of macroscopic propagation.

3.5 Statistics of Diode Failure

Once the possible diode failure modes are understood, it makes sense to investigate to what extent the arrangement of asymmetric voids can actually influence failure across many replicates. To that extent, many diode samples were tested across 4 designs and 3 spacings to gain a clearer understanding of how directional asymmetry can influence failure that is otherwise governed by Weibull statistics and weakest link theory.

Table 3.2: Distribution of sample failures for the triangular void arrangements evaluated in this investigation.

Type	Total	Favorable	Random
Unidirectional	42	33	5
Bidirectional	30	19	6
Unidirectional No Notch	34	12	11
Unidirectional Double Notch	50	33	10

The distributions of failure modes for each of the triangular void arrangements tested in this study are shown in Table 3.2. The exact nature of the failure distribution as well as the impact of spacing are discussed in more detail on a case-by-case basis for

each arrangement.

Unidirectional Diodes

A total of 42 unidirectional diode samples were tested across 3 different spacings. Of these 42 samples, 33 failed in the favorable mode, with 5 failing randomly and 4 failing unfavorably. This equates to 78% of samples failing in the mode predicted by numerical simulations to be favorable. This 78% favorable failure rate is the first clear indicator that asymmetric void orientation has an influence on the macroscopic failure properties. If the voids had no influence on failure, it would be expected that failure modes were governed solely by natural material flaws, which would follow a Weibull distribution. If this were the case, the number of samples failing favorably would likely be similar to the number of samples failing unfavorably, and the number of random failures would be significantly higher. Although void orientation showed a clear effect on the failure mode in unidirectional structures, no dependence on void spacing was observed.

Bidirectional Diodes

For the bidirectional diode design, a total of 30 samples were tested. Across all three spacings tested, a total of 19 samples failed in the favorable configuration, which in this case was predicted to be failure originating from the symmetrical void at the center of the specimen. Of the remaining 11 samples, 6 failed randomly and 5 failed unfavorably, with unfavorable failure being classified as failure that originated from either edge of the specimen. This equates to failure distribution with a 63% favorable rate, which is again well above the expected value from random flaws and indicates that similar to the unidirectional design, the bidirectional void arrangement has an influence on the mode of failure of the specimen, although in this case it does not produce directional asymmetry, as the arrangement is symmetrical about the center of the specimen. There was also not found to be any significant correlation between void spacing and occurrence of favorable failure, as both random and unfavorable failure events were relatively few in number and reasonably well distributed across all spacings. However, it should be noted that when the unidirectional and bidirectional failure distributions are compared, the unidirectional specimens have a greater tendency to fail favorably by about 15%, which is a noticeable margin given the number of replicates tested for each design. It was suspected that some of this difference may arise from the presence of an edge notch in the unidirectional design. To determine whether or notch this notch was creating a significant difference,

additional unidirectional designs were explored.

Edge Notch Effects

To clarify whether or not the disparity in favorable failure rates between unidirectional and bidirectional specimens was due to edge notch effects, additional testing was done on unidirectional designs containing no edge notches as well as unidirectional designs with identical notches on both sides. When the notches were removed from the unidirectional specimens, a dramatic change in the distribution of failure modes was observed. Out of a total of 34 specimens tested across three spacings, only 12 failed in the favorable mode as predicted by numerical analyses. Out of the remaining 22 specimens, 11 failed randomly, and 11 failed unfavorably, leading to a 35% favorable failure rate and creating and almost perfectly uniform distribution of failure between all three modes, which is markedly different than the distribution seen in either the notched unidirectional or bidirectional specimens. This indicates that the presence of an edge notch has an even stronger effect on failure mode than originally expected; when edge notches are removed, failure becomes less dependent on void orientation, and thus failure modes become more random.

To better understand the influence of the edge notch on crack nucleation, an additional unidirectional design was explored with identical edge notches present on both sides of the specimen. For this double-edge notch design, a total of 50 specimens were tested across 3 different spacings. Of these 50 specimens, 33 failed favorably, 10 failed randomly, and 7 failed unfavorably, leading to a 66% favorable failure rate, very similar to that of the bidirectional specimens. Even when present on both sides, the edge notches seem to significantly increase the occurrence of nucleation from the edges of the specimen, which better allows the anisotropy of the voids to influence the failure mode by making propagation in one direction more favorable than in the other.

These double-notched specimens were also the first specimens to show spacing dependence on mode of failure. In the double-notched specimens, 80% of the random failures that occurred were in samples with the smallest spacing, which was 0.5 mm of solid material between consecutive voids. Most random failures were characterized by cracks nucleating near both edges of the specimen and propagating inward to meet near the center of the specimen. This significantly higher occurrence of random failure at smaller spacing suggests that as the spacing gets smaller, the anisotropy of the voids plays a less significant role, and the inter-void solid sections

behave less like asymmetric solid regions and more like small fibers or ligaments. This idea is further supported by the numerical analyses reported in Table 3.1, which shows a significantly smaller difference in toughness values between the favorable (forward) and unfavorable (backward) propagation modes when the spacing between voids is small. This spacing dependence also suggests that the many of the favorable failures seen at smaller spacings in the unidirectional specimens with only one edge notch may have been governed predominantly by the presence of the edge notch rather than by the asymmetry of the void arrangement itself.

3.6 Designing a "True Diode"

Analysis of the occurrence of favorable failure based on void orientation indicates that the asymmetry of the void structures plays a significant role in directional failure under unbiased loads. Despite this, even when the highest occurrence of favorable failure is considered, 78% for unidirectional diodes with only one notch, the favorable failure rate is still far too low to be considered behavior resembling that of a diode. However, using the knowledge gained from the analyses of these triangular void designs, heterogeneous structures can be made that have failure behavior resembling that of a diode.

The previous analyses demonstrated clearly that in order to obtain directional fracture behavior with high fidelity, both nucleation and propagation of the crack must be meaningfully controlled and constrained to minimize the number of possible failure occurrences that can arise from weakest link failure behavior. The importance of controlling nucleation is emphasized by the analysis of the mechanics of unfavorable failure. The analysis of unfavorable failure clearly demonstrates that even though void arrangement can make propagation of a crack preferentially less favorable in one direction, the location of the critical flaw in the system can still set the crack along a trajectory where a less favorable failure condition is the only reasonable means of releasing mechanical energy. Without any structural influence, nucleation of the crack from a critical flaw is dictated by weakest link theory, and because the printing process does not contain any spatial bias with respect to void arrangement, this nucleation should be random. However, if an asymmetric structure is to behave like a true fracture diode, this nucleation must be constrained such that the possible nucleation sites fall within regions where the asymmetric structure can effectively control propagation direction.

If true fracture diode behavior is to be achieved, once nucleation is properly controlled,

propagation must have strong directional asymmetry. In the previous analyses with isosceles triangle voids, it was found that both void spacing and structure played critical roles in the degree of toughness asymmetry seen during crack propagation. Fractographic analysis showed that in the case of unfavorable propagation, the crack would become pinned at a void and then nucleate at the triangle tip in the next consecutive void, and the energy required to achieve this was related to the distance between the pinning void and the tip of the next consecutive void. This spacing effect was also seen in the double-notched specimens, where once the spacing between voids became too small, the toughness asymmetry was not dramatic enough to discourage propagation in the unfavorable direction, and failure became effectively random.

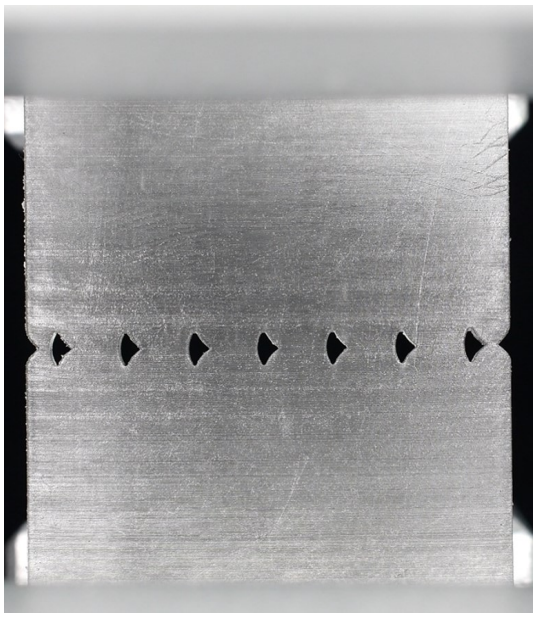

Figure 3.16: The "true diode" specimen design. In this design, the triangular voids were rounded and spaced further apart to increase toughness asymmetry and the solid segment size near the edges of the specimen were reduced to better control nucleation.

Using this information, a diode structure was designed that was able to effectively control both nucleation events as well as subsequent propagation. This design is shown in Figure 3.16. To better control nucleation without introducing bias, edge notches are introduced to both sides of the specimen to encourage nucleation from the edge of the specimen. Additionally, the solid segments near the edges of the specimen are much smaller in cross sectional area than the other inter-void spacings. This reduction in cross section near the free surface further encourages nucleation

near the sides of the specimen by locally increasing the compliance in these regions. To better control propagation, this diode structure uses a rounded triangle void design to further increase the toughness asymmetry between the favorable and unfavorable propagation modes. Additionally, void spacing is designed to make unfavorable propagation by nucleation at successive triangle tips even more difficult. This difficulty due to relatively large spacing is clearly evidenced in the numerical analysis of this diode structure shown in Figure 3.17. The larger spacing of the diodes significantly reduces the buildup of damage at the tips of successive triangles in backwards propagation, forcing much greater damage buildup at the rounded edge of the pinning diode, which requires significantly more energy to nucleate and propagate a crack. It is important to note, however, that this larger spacing effect does not scale monotonically. If the spacing of the voids becomes too far apart, the voids begin to act as isolated stress concentrators in an otherwise homogeneous matrix, and failure becomes governed the largest flaw within the homogeneous region between these voids. In this sense, choosing the spacing of the diodes is a balance between increasing spacing to discourage unfavorable propagation and reducing spacing to prevent weakest-link-governed failure. In the case of this investigation, the tailoring of this spacing was done empirically, but controlling the balance between these two effects is likely dependent on material processing, as this will dictate the resultant stiffness and toughness as well as the distribution of flaws within the material.

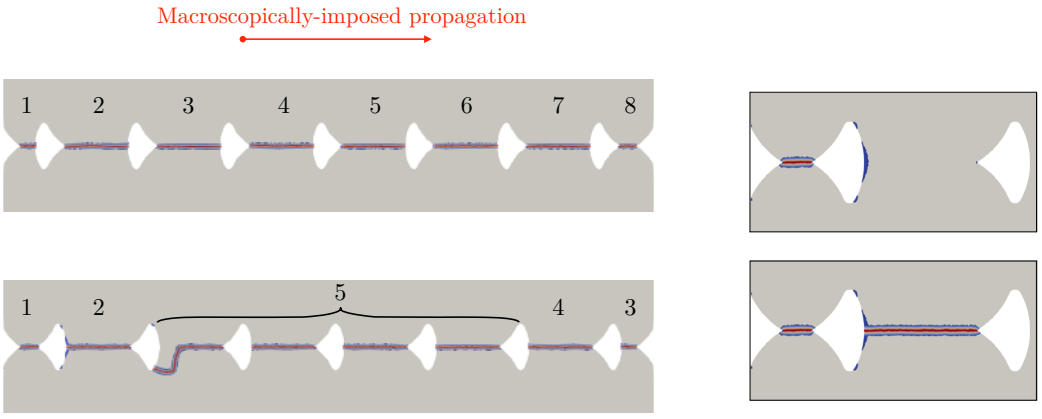

Figure 3.17: Numerical analysis of the true diode structure under surfing load conditions. (Left) Crack path in the forward and backward configuration, with numbers indicating the order of failed segments; (Right) Inset showing the fracture field in the backward specimen.

Using this true diode design, a total of 12 specimens were tested, and of these 100% failed favorably, indicating the potential for designed inclusions to produce

controllable directional fracture. Even though fracture is a statistical phenomenon, sufficient control of both compliance and anisotropy can constrain the system enough to produce a readily predictable outcome for both the nucleation and propagation of the crack. This controllable directional fracture could present significant opportunities for brittle materials in the context of a different approach to material optimization, where materials whose toughness cannot be sufficiently improved could be designed to instead fail in a way that minimizes catastrophic damage.

3.7 Summary

In this chapter, the influence of asymmetric void structure on failure behavior was explored using structures described as "fracture diodes". These structures used designs of triangular voids in different orientations to create directionally-dependent toughness behavior, which manifested as preferential directional failure under unbiased uniaxial tensile load. Several void designs were explored, including unidirectional and bidirectional arrangements as well as 3 different void spacings. Numerical simulations showed that the favorable failure direction was the direction of triangle convergence, and this was confirmed in experiment though both fractographic and statistical analysis. Analysis of the distribution of favorable failures for each arrangement showed that the presence of a notch at the edge of the specimen created some bias that encouraged failure from that edge, but introduction of symmetrical edge notches on both sides of the specimen reduced this bias. Finally, a "true diode" design was developed that used rounded triangles and carefully controlled void spacing to further enhance toughness asymmetry, resulting in favorable directional failure 100% of the time.

REFERENCES

[1] M. Z. Hossain, C. J. Hsueh, B. Bourdin, and K. Bhattacharya. Effective toughness of heterogeneous media. *Journal of the Mechanics and Physics of Solids*, 71(1):15–32, 2014. ISSN 00225096. doi: 10.1016/j.jmps.2014.06.002. URL http://dx.doi.org/10.1016/j.jmps.2014.06.002.

[2] B. Bourdin, G.A. Francfort, and J-J. Marigo. Numerical experiments in revisited brittle fracture. *Journal of the Mechanics and Physics of Solids*, 48(4):797–826, apr 2000. ISSN 0022-5096. doi: 10.1016/S0022-5096(99)00028-9. URL https://www.sciencedirect.com/science/article/pii/S0022509699000289.

[3] Blaise Bourdin, Gilles A. Francfort, and Jean-Jacques Marigo. The Variational Approach to Fracture. *Journal of Elasticity*, 91(1-3):5–148, apr 2008. ISSN 0374-3535. doi: 10.1007/s10659-007-9107-3. URL http://link.springer.com/10.1007/s10659-007-9107-3.

[4] Satish Balay, William D. Gropp, Lois Curfman McInnes, and Barry F. Smith. Efficient Management of Parallelism in Object-Oriented Numerical Software Libraries. In *Modern Software Tools for Scientific Computing*, pages 163–202. Birkhäuser Boston, Boston, MA, 1997. doi: 10.1007/978-1-4612-1986-6_8. URL http://link.springer.com/10.1007/978-1-4612-1986-6{_}8.

[5] S. Balay, S. Abhyankar, M. Adams, J. Brown, P. Brune, K. Buschelman, L. D. Dalcin, V. Eijkhout, W. Gropp, D. Kaushik, M. Knepley, D. May, L. Curfman McInnes, T. Munson, K. Rupp, P. Sanan, B. Smith, S. Zampini, H. Zhang, and H. Zhang. PETSc Users Manual Revision 3.8. Technical report, Argonne National Laboratory (ANL), Argonne, IL (United States), sep 2013. URL http://www.osti.gov/servlets/purl/1409218/.

[6] S. Balay, J. Brown, K. Buschelman, W.D. Gropp, D. Kaushik, M. Knepley, L.C. McInnes, B. Smith, and H. Zhang. PETSc/Tao: Home Page, 2013. URL https://www.mcs.anl.gov/petsc/.

[7] G.P. Cherepanov. Crack propagation in continuous media: PMM vol. 31, no. 3, 1967, pp. 476–488. *Journal of Applied Mathematics and Mechanics*, 31(3):503–512, jan 1967. ISSN 0021-8928. doi: 10.1016/0021-8928(67)90034-2. URL https://www.sciencedirect.com/science/article/pii/0021892867900342.

[8] A. A. Griffith. The Phenomena of Rupture and Flow in Solids. *Philosophical Transactions of the Royal Society A: Mathematical, Physical and Engineering Sciences*, 221(582-593):163–198, jan 1921. ISSN 1364-503X. doi: 10.1098/

rsta.1921.0006. URL http://rsta.royalsocietypublishing.org/cgi/doi/10.1098/rsta.1921.0006.

[9] James R Rice. Mathematical Analysis in the Mechanics of Fracture. Technical report, 1968. URL http://esag.harvard.edu/rice/018{_}Rice{_}MathAnalMechFract{_}68.pdf.

[10] C-J. Hsueh, L. Avellar, B. Bourdin, G. Ravichandran, and K. Bhattacharya. Stress fluctuation, crack renucleation and toughening in layered materials. *Journal of the Mechanics and Physics of Solids*, 120:68–78, nov 2018. ISSN 0022-5096. doi: 10.1016/J.JMPS.2018.04.011. URL https://www.sciencedirect.com/science/article/pii/S0022509617311407.

[11] M Y He and J W Hutchinson. Crack Deflection at an Interface Between Dissimilar Elastic-Materials. *Int J Solids Struct*, 25(9):1053–1067, 1989.

Chapter 4

DESIGNED ANISOTROPY IN BRITTLE CERAMICS: MICA AS A MODEL SYSTEM

The contents of this chapter are based on work from the journal article "Obreimoff revisited: Controlled heterogeneous fracture through the splitting of mica" by M.T. Johnson, N.R. Brodnik, T. Ekeh, K. Bhattacharya, and K.T. Faber. This article has been accepted to the journal *Mechanics of Materials* and is pending publication.[1] M.T. Johnson and N.R. Brodnik were both listed as first authors on this publication, as they collaborated on both the experimental design as well as the testing of samples and production of figures.

4.1 Introduction

The influence of designed anisotropy on fracture behavior was demonstrated in the previous chapters with brittle polymer systems fabricated using digital light processing. However, these experiments also showed some of the challenges that arise with the transition to fracture in ceramics. Many of these challenges arise from the fact that failure properties are dependent not only on the fracture toughness of a material, but also its stiffness, and the combination of these two properties dictates how well a material can dissipate energy during failure. Many ceramics have fracture toughness values similar to those seen in brittle polymers, but they are thousands of times stiffer, which makes them far worse at dissipating energy during fracture, and this makes controlling and measuring failure response much more challenging.

This control of failure behavior plays a critical role when analyzing heterogeneous ceramic structures centers with discrete crack interaction events. When a heterogeneous structure is being used to influence macroscopic toughness and the structure itself is discrete (cannot be approximated as a single continuous material), the only way that the effect of inclusions can be properly evaluated is if the toughness of the system can be measured before, during, and after crack-inclusion interaction. This greatly constrains the number of available methods for evaluating toughness, as the system must be loaded in a way that provides continuous stable crack growth throughout the entirety of the interaction between crack and inclusion. If stability of the system changes as the crack lengthens, as occurs in tests such as compact tension and bending, the measured toughness will be dependent on the absolute position

of the inclusions within the sample, which is not useful for assessment of material properties.[2] As previously demonstrated, surfing load is able to achieve continuous stable crack growth, but it has limitations regarding the stiffness of materials that can be tested.[2] One test that has been shown to demonstrate global stability, however, is small-angle wedge splitting, which can readily be done on ceramics with layered crystallographic structures.[2]

The earliest forms of small-angle wedge splitting are almost as old as the field of fracture mechanics itself. In 1931, just 10 years after Griffith's work [3], J.W. Obreimoff performed an experiment to investigate whether or not the surface chemistry mechanisms that produced contact bonding were the same mechanisms that governed brittle fracture.[4] In the experiment, muscovite mica, which is known to cleave smoothly along the (001) crystallographic plane, was split with a blunted glass wedge, and the curvature of the split mica surface was used to determine the energy required for separation, which is a combination of the surface energy for the newly formed surfaces 2γ and the mechanical energy required to bend the cleaved mica sheet with the wedge. After the first splitting, the wedge was retracted and the mica was split a second time to determine if the fracture would heal and subsequently re-separate, as is the case with contact bonding of smooth surfaces. The results demonstrated that contact bonding and fracture are fundamentally different, and the latter is not fully reversible. Moreover the fracture energy of mica is dependent on the environment in which it is fractured, as the presence of air, or more specifically water vapor in air, reduces the energy required to form new surfaces.[4] As previously discussed, this is also one of the earliest published fracture studies to demonstrate continuous stable crack propagation [2], which has been established as critical for the understanding of discrete interactions between cracks and heterogeneous structures.

In the time since Obreimoff's study, mica has been a material of research interest both mechanically as well as chemically. Its layered structure creates smooth pathways along which fracture can occur, allowing for controlled observation of brittle fracture where the crack front is constrained to a single plane. Wedge opening experiments similar to Obreimoff's have been used to investigate in greater detail the crack healing abilities of mica as well as the kinetic aspects of thin interface fracture.[5] Additional splitting experiments have been used to study the fracture and contact energies of mica-mica and mica-silica interfaces in moist environments as well as the effects of crack damage recovery and interface misorientation on mica interfaces.[6, 7] Beyond mechanical characterization, pristine cleaved mica surfaces can also be

functionalized and used as substrates for thin film growth.[8, 9]

Although wedge splitting presents great promise in terms of achieving stable crack growth, challenges still arise with the introduction of heterogeneous structure into a naturally layered system like mica. Fortunately, a reliable method for producing heterogeneous structure in constrained fracture has already been established in a related context. Recently, there has been great interest in how contrast in material properties of composite constituents can affect strength and toughness. However, studying and simulating the fracture behavior of composite structures across multiple dimensions and length scales can prove difficult, so these composite systems are often constrained in one or more dimensions. One of simplest methods for applying this type of constraint is tape peeling, where the toughness of the tape system is the work of adhesion originally described by Rivlin [10], and the stiffness is affected by changing either the thickness or material composition of the tape. Traditionally, tape that is being peeled can be described as a membrane, but elasticity plays a role in peeling behavior in cases where the tape is under large tensile stresses or the peeling angle is small.[11] This latter case is of particular interest because when elasticity plays a significant enough role, tape peeling can be a reasonable analog to fracture. Furthermore, a tape peeling with a small peel angle can be seen in several respects to be similar to wedge splitting with a small splitting angle, so techniques for introducing heterogeneous structure should translate well between techniques.

In the case of tape peeling with small peel angles, several studies have demonstrated that either compliance or elastic contrast in tape can produce a significant change in the required peel force without any alteration to the work of adhesion itself.[11–14] This contrast can be produced by either introducing multiple layers of tape to vary stiffness or by changing the polymer composition of the tape substrate without changing the adhesive. Similar behavior has been shown in the constrained fracture of three-dimensional printed specimens with different polymer layers as well as in the separation of glass from soft adhesive substrates, where variations in composition can be used to change both the composition and adhesive properties of the substrate, which would alter the analogous stiffness and toughness respectively.[12, 14–18] Finally, the effect of stiffness and toughness contrast in constrained fracture has also been demonstrated numerically both for tape peeling as well as for fracture of heterogeneous materials.[19, 20]

Tape peeling studies provide promising insight into the fracture mechanics of multi-material composites, but they can only provide limited information about

failure of stiff, brittle systems like ceramics, as they typically rely on soft polymeric materials with large cohesion zones and low elastic moduli, which ultimately affect the resultant failure behavior.[21] This is where the layered structure of muscovite mica presents a promising opportunity for the investigation of brittle fracture. Small angle wedge splitting of mica can provide constrained, continuously stable, brittle fracture of a model system with high stiffness, where heterogeneous structure can be readily introduced. First, homogeneous muscovite mica is split with a glass wedge similar to Obreimoff's experiments to establish a baseline material behavior. Once homogeneous material behavior is established, thickness variations are introduced into the system to study how compliance contrast affects both the required splitting force as well as the subsequent failure behavior in ceramics. Finally, the implications of this investigation are then discussed in the context of the design of layered ceramic composites.

4.2 Methods

Materials

Mica samples for testing were prepared from sheets (V-1 quality, Electron Microscopy Sciences, Hatfield, PA, USA) designed for atomic force microscope applications. Individual mica sheets, nominally 25 x 75 x 0.26-0.31 mm^3, were burnished lightly on 400 grit paper to remove edge defects that may have been introduced in prior cutting operations. Sheet dimensions were unchanged from processing, and care was taken to prevent any visible mica cleavage during handling. For testing, individual samples were mounted vertically on a T-shaped aluminum sample holder using wafer mounting adhesive (Wafer-Mount 559, Electron Microscopy Sciences) following Figure 4.1a.

Mechanical Testing

In the context of this study, the force required to split the mica was used as an indirect analog to the measurement of actual fracture toughness, which requires measurement of the curvature of the mica. Although measuring the splitting force is indirect, it should still be a good predictor of the toughness of the system so long as the system is quasi-static and the wedge is advanced slow enough to allow the fracture front to equilibrate with each propagation event. The quartz wedge used to apply this splitting force was prepared from a quartz sheet (150 x 50 x 1 mm^3) polished to a 25° angle using abrasive paper. This polished edge was flame-treated to remove any residual polishing marks and gently round the tip of the wedge. The prepared wedge

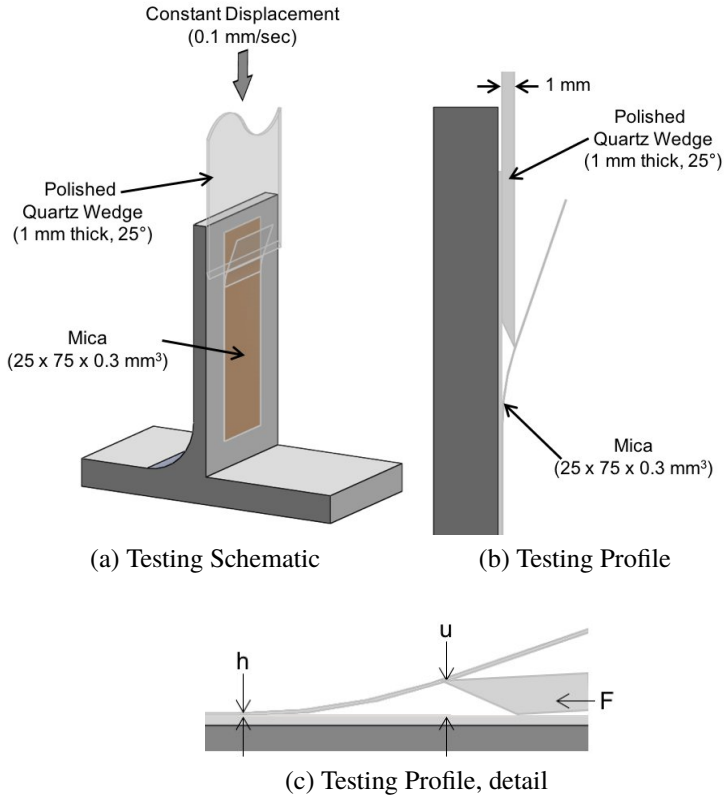

(a) Testing Schematic (b) Testing Profile

(c) Testing Profile, detail

Figure 4.1: Schematics showing (a) the mica splitting sample setup, (b) a side profile of the cleavage front, and (c) the wedge orientation in more detail.

was mounted in an Instron 5982 mechanical testing frame (Instron Corporation, Norwood, MA) and aligned vertically with the angled tip oriented away from the mica sample following Figure 4.1b. This orientation was chosen to encourage the wedge to smoothly pass over any defects or height variations present in the substrate mica, which reduces the occurrence of both undesired pinning of the wedge as well as tearing of the cleaved sheet during testing. In all testing, the mica cleavage front extends a considerable distance (5 to 20 mm, depending on cleaved sheet thickness) in front of the wedge.

An initial cleavage crack was started by hand using a razor blade prior to insertion of the quartz wedge for testing. Tests were performed with a constant displacement rate of 0.1 mm*s^{-1} until the cleavage crack extended fully through the sample. Samples demonstrating an abundance of defects — typically in the form of tearing or pinning from edge defects — were discarded. To monitor crack propagation, still images were taken at five second intervals through the duration of testing. A mirror was used to simultaneously capture both the face and profile of samples, and images were synchronized to force-displacement curves to correlate propagation events with

measured mechanical response.

Homogeneous Samples

A initial series of 27 mica samples with homogeneous cleave layer thickness, shown schematically in Figure 4.2, were tested in order to validate test methods and determine a correlation between measured splitting force and the thickness of the cleaved mica layer. Mica sheets of thicknesses ranging from 0.01 to 0.16 mm were cleaved from larger mounted samples. The measured force was averaged over the steady-state portion of the test to determine the splitting force for a given sample. Typically, the first 10-15 mm of test displacement as well as the last 15-20 mm were discarded from averaging, as these regions tended to show edge effects either from the initiation of the crack with a razor or from the cleave front approaching the end of the sample. Within the measurement region, samples sometimes showed the presence of transient increases in load above the steady-state, which were fully recoverable. Due to their random nature, these events occurred at varying locations in the measurement region and their prevalence tended to increase with increasing thickness. Samples with sufficiently few of these events to still achieve a steady-state condition were included in analysis, with the events themselves removed from averaging.

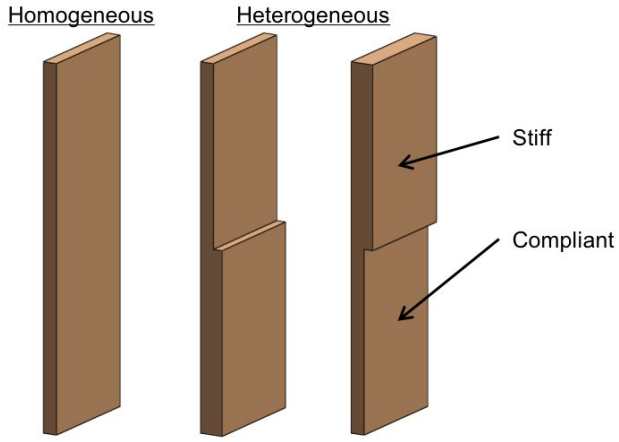

Figure 4.2: Schematic of homogeneous and heterogeneous sample profiles.

Heterogeneous Samples

A second series of samples were prepared with prescribed thickness variations to alter the bending stiffness in different regions along the length of the fracture plane as shown in Figure 4.2. A razor blade and straight edge were used to hand-scribe a parting line near the middle of the sample, which marks the location of the

heterogeneity. Mica sheets above or below this parting line were cleaved by hand to create a step-wise thickness transition. After splitting of heterogeneous specimens, the thicknesses of the two different sections of the cleaved sheet were measured, and the difference in thickness between these sections was taken to be the overall height of the heterogeneity.

4.3 Results and Discussion

Homogeneous Samples

A variety of different homogeneous mica sheet thicknesses were tested both to build a baseline of expected splitting forces as well as to determine the intrinsic toughness of the mica, which is directly related to the surface energy of the basal cleavage planes in the mica crystal. Establishing this baseline is particularly critical for later heterogeneous studies because mica's stiffness of 200 GPa [2] is much higher than the polymers used tapes or other soft substrates, so the elastic component of the separation energy is significantly larger than in the case of heterogeneous tape peeling or other membrane separation.

Load-displacement curves for a representative selection of mica cleavage thicknesses are shown in Figure 4.3. These curves each show an initial increasing load regime over approximately the first 10 mm of displacement as well as an observable load drop within the final 10-15 mm of displacement, both of which are likely due to edge effects. Between these loading and unloading sections exists a generally constant splitting load that scales proportionally with the thicknesses of the cleaved mica sheet. Of note in the 0.04 mm, and more notably in the 0.06 mm curves, transitory increases in force are evident in the 20-30 mm and 50-60 mm displacement ranges respectively. These increases in force are due to localized imperfections such as edge defects or localized sheet tears. These effects were characterized by their random occurrence and magnitude, and in some cases, small local tears could even be visually observed. There was no strong indicator to the occurrence of these imperfections, but they tended to be more prevalent in the splitting of thicker sections of mica. As previously mentioned, these defect events, as well as initial loading and unloading periods, were omitted when calculating the mean splitting force. Observations of samples following testing showed that, with the exception of small local tears, cleavage propagation was dictated by the layered structure of mica, with splitting events never deviating from the initial cleavage plane regardless of the thickness or structure of the cleaved sheet.

Originally described by Obreimoff[4] in terms of surface energy, γ, and later by

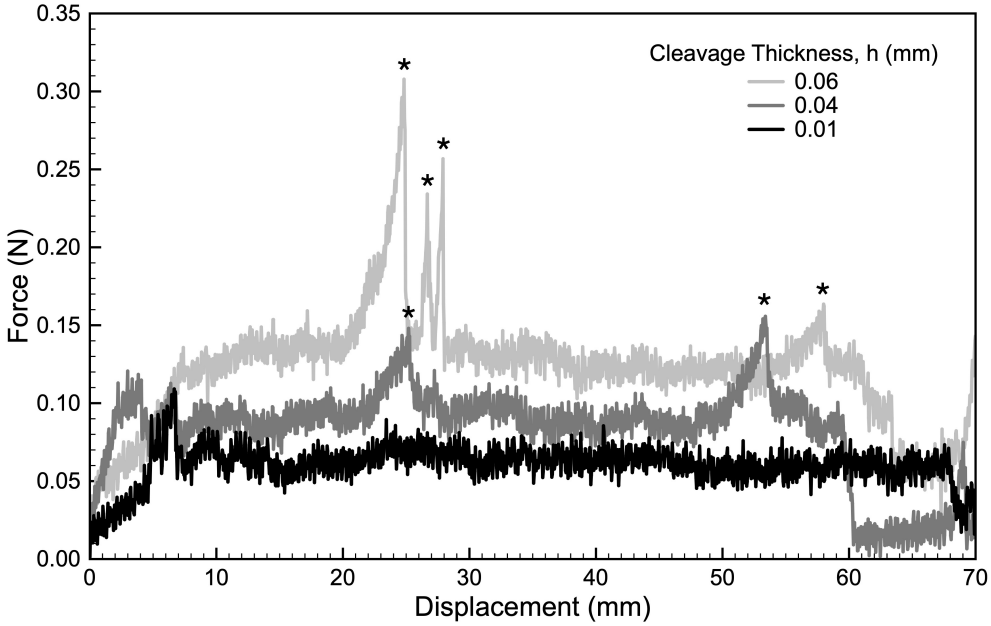

Figure 4.3: Load vs. displacement for the cleavage of select homogeneous mica layers. Transitory increases in force (*) due to edge defects or localized tears were excluded from analysis.

Williams[22] using energy release rate, G, the width-normalized force, F/b, can be correlated to cleavage thickness, h, following

$$\frac{F}{b} \approx G\left(1 + \frac{\mu}{\alpha}\right) \tag{4.1}$$

where α is a geometric factor related to the angle of contact between the wedge face and the mica sheet that can be described as

$$\alpha = 3\left(\frac{u}{h}\right)^{\frac{1}{2}}\left(\frac{G}{6Eh}\right)^{\frac{1}{4}} \tag{4.2}$$

where u is wedge thickness, E is elastic modulus, and μ is the coefficient of friction between wedge and mica. These relations, developed by Williams for the case of small angles, account for elastic deformations, but omit plastic deformation. Friction is also accounted for in the mathematical expression, but quantifying friction experimentally is not straightforward, so some variability is expected in this regard. The assumptions of elastic deformation and small splitting angles are considered to be appropriate though, as no permanent deformations were observed in cleaved mica sheets and the crack tip extends approximately 10 mm in advance of the wedge face, so the largest angles of deflection achieved are of the order of 20°, which is within the range for which the small angle assumption used by Williams is valid.[22]

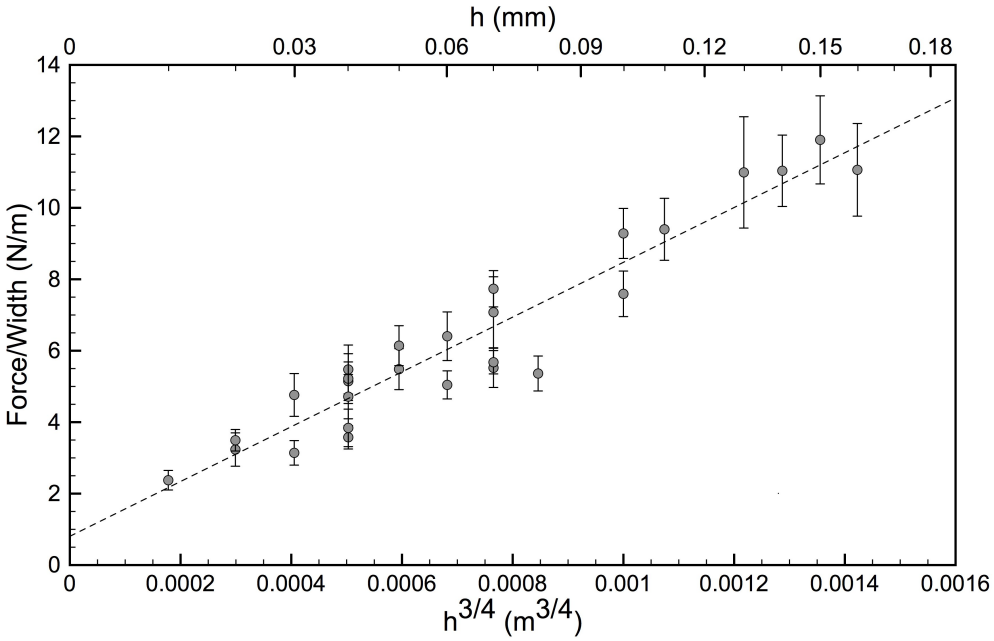

Figure 4.4: Width-normalized average force vs cleavage thickness, $h^{\frac{3}{4}}$.

Shown in Figure 4.4, a regression of normalized force with respect to $h^{\frac{3}{4}}$ reveals a linear trend which corresponds well to Equation 4.1. The intercept of this regression line is a measure of the normalized force associated with cleaving an infinitely thin mica sheet, which can otherwise be seen as energy required for the creation of two new mica surfaces or the thickness independent critical strain energy release rate, G_c. The critical strain energy release rate in air was measured in this work to be $0.81 \pm 0.38 \frac{J}{m^2}$. Obreimoff's original G_c, determined via surface-energy analysis and expressed as 2γ, was determined to be $0.76 \frac{J}{m^2}$.[2, 4] Similarly, Wan et al. measured mica-mica adhesion energy across a range of relative humidities; they observed energies in the range of 0.6 to 0.8 $\frac{J}{m^2}$ at humidities of 20% and above.[7]

Much of the variability in splitting strength seen in this study is likely due to the combination of frictional effects and natural variations in mica. However, with sufficient replicates across a range of thicknesses, this variation can be accounted for, and a G_c value can be determined that is in good agreement with those found in literature. This agreement indicates that the wedge cleavage techniques developed here are appropriate for the measurement of splitting strengths for the range of mica thicknesses examined in this study.

Heterogeneous Samples

Mica samples with thickness heterogeneities were prepared and tested in an analogous fashion to samples of homogeneous thickness. Shown in Figure 4.5 are two loading curves for mica samples of 0.03 mm initial thickness and 0.06 mm final thickness with a step-wise change of thickness at approximately 30 mm of displacement. Both of these samples show similar loading behavior to their homogeneous analogs, whose range of splitting strengths (with uncertainties included) are shown in the shaded regions. Additionally, the observed loads in the constant-thickness regions before and after the step-wise thickness change are in good agreement with predicted load values based upon Equation 4.1 and Figure 4.4. However, unique to samples of heterogeneous thickness is the significant increase in force as the crack interacts with the sudden change in mica thickness. Like the homogeneous samples discussed earlier, there was no observed change in crack path at any point during testing as the crack stayed fully constrained to the cleavage plane. The observed increase in splitting force, approximately 5x above the baseline, combined with no change to the crack path indicates that the presence of an increased-thickness heterogeneity has increased the effective macroscopic toughness of the mica system well over that of homogeneous structures of equivalent thickness. These observations are not explained by the classical analyses of Obreimoff and Williams, where only constant-thickness cleavage is addressed.

As the cleavage front passes from compliant (thin) regions to stiff (thick) regions, the front experiences a rapid change in stored elastic energy within the portion of the mica sheet that is being bent. As the crack front interacts with the thickness increase, the work being done by the advancing wedge transfers from propagating the crack to bending the split mica layer, slowing crack advancement. The geometry of the wedge splitting setup makes it difficult to precisely predict the splitting force enhancement due to this change in thickness, as all sources of friction as well as the exact wedge thickness and exact sheet thickness need to be known, and this is not straightforward. However, a good analytical indicator of the expected splitting force enhancement is the differences in flexural rigidity between the two regions of the heterogeneous mica sheet. This approach has been used to describe similar contrast in membrane peeling. Based on this, the splitting force enhancement can be estimated as

$$\frac{F_{heterogenous}}{F_{homogeneous}} = \frac{D_{stiff}}{D_{compliant}} \tag{4.3}$$

where D is the bending rigidity, which is described as

$$D = \frac{Ebh^3}{12\left(1-\nu^2\right)} \tag{4.4}$$

where E is elastic the modulus, b is the width of the mica sheet, b is the thickness of the cleaved layer in the region being evaluated, and ν is Poisson's ratio. It follows from this that for the case of heterogeneous mica, the change in splitting force is proportional to h^3 for a bending beam, so changes in splitting force should scale with the cubed magnitude of the change in thickness across the heterogeneity. For the mica dimensions in Figure 4.5 this would predict an eight-fold enhancement in cleavage force, though again, some variation is expected due to differences in test geometry between membrane peeling and wedge splitting. Xia et al. did observe an eight-fold peeling force enhancement in experiments on polyester-backed adhesive tape on epoxy substrates, but these were more precisely analogous to direct peeling of membranes.[12]

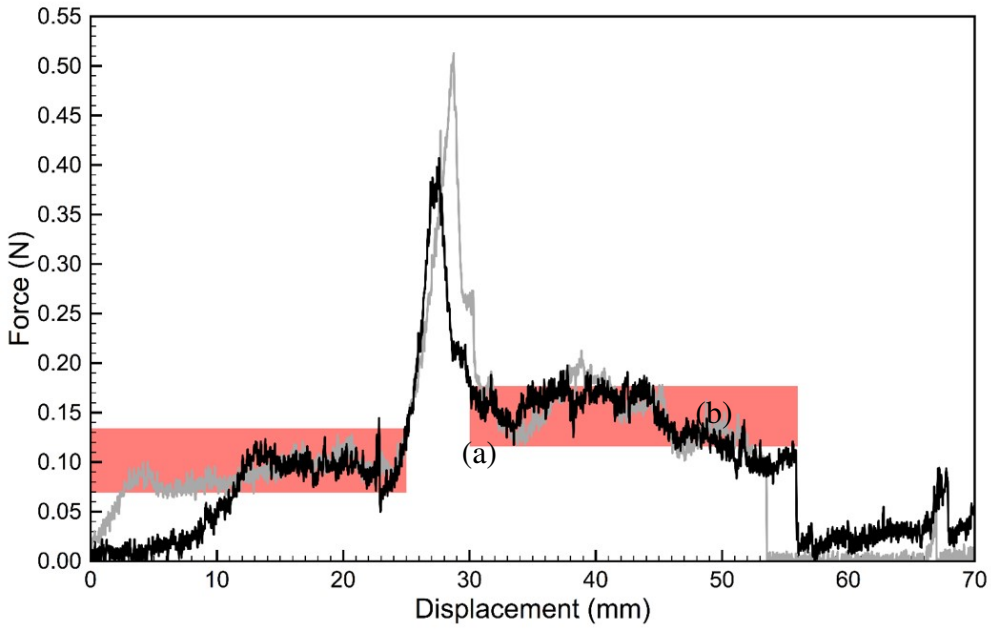

Figure 4.5: Load vs. displacement for the cleavage of mica layers with thickness heterogeneities. Heterogeneities took the form of step-wise thickness increases, from 0.03 to 0.06 mm, at approximately 30 mm of displacement. The shaded region (a) corresponds to the force required to split a homogeneous sheet of thickness 0.03 mm and the shaded region (b) corresponds to the force required to split a homogeneous sheet of thickness 0.06 mm.

To visually correlate crack position to force enhancement, Figure 4.6 shows a

progression of still profile images correlated to specific positions in the load-displacement curve for a 0.03 to 0.06 mm thickness change. Figure 4.6A shows the crack position well in advance of the quartz wedge at the approximate moment where the crack meets the thickness step as indicated by the dotted line across each photo. Figure 4.6B shows a growing increase in curvature of the separated mica layer while the cleavage front appears to still be pinned by the step-wise change of thickness. Figures 4.6C and D show continuing increases in curvature as the splitting force reaches its maximum value. After the thickness step, Figure 4.6E shows a return to behavior similar to the homogeneous splitting conditions where the crack front has become unpinned and has jumped forward, reducing the curvature of the cleaved mica layer.

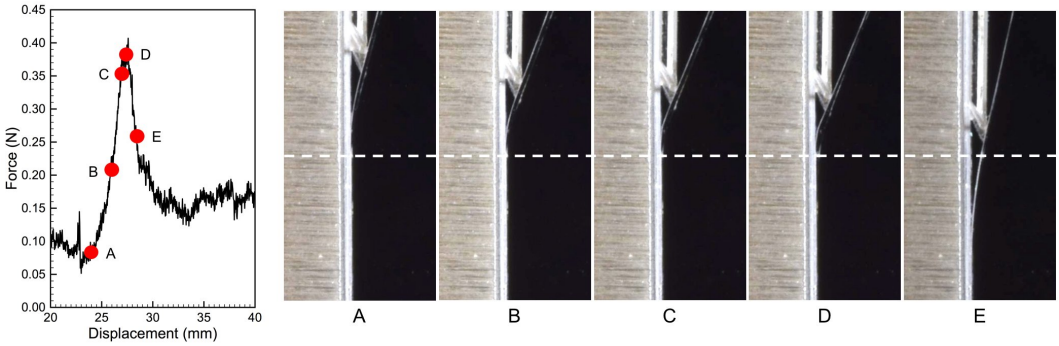

Figure 4.6: Profile still image progression of cleavage crack interacting with a 0.03 to 0.06 mm step-wise thickness change. Image labels correlate to points indicated in Force v. Displacement plot.

Figure 4.7 shows orthogonal face-on views of the same loading stills shown in Figure 4.6. Solid blue lines indicate the position of the advancing quartz wedge while the light gray shading tracks the furthest progress of the crack front. The general position of the crack tip in this perspective correlates well to the profile view; however, some curvature of the crack front is evident immediately after the thickness heterogeneity. As the load builds, Figure 4.7A and B, the crack front stays stationary at the thickness step. Near the point of peak load, Figure 4.7C and D, the crack front has migrated past the heterogeneity on the left-hand side of the mica sheet while still being pinned on the right-hand side. After passing the thickness step, Figure 4.7E, the crack front has jumped further ahead of the quartz wedge as the influence of the heterogeneity is passed.

Unlike in previous tape-peeling and soft membrane studies, where the peeling front propagates past the thickness heterogeneity coupled with an instantaneous drop in

peel force, the cleavage force in these tests falls more gradually, over the span of approximately 5 mm of displacement. This delayed load drop correlates well to the time delay associated with the crack passing the thickness heterogeneity, as illustrated in the progression in Fig 4.7. Likewise, the eight-fold enhancement of cleavage force as predicted by bending rigidity is likely not fully realized since the the cleavage front propagates through the heterogeneity unevenly across the width of the specimen. This could be due to a number of effects including natural variations in the mica as well as slightly imperfect orientation of the wedge with respect to the thickness heterogeneity. This imperfect orientation arises because the wedge is flame polished to minimize surface roughness and reduce the occurrence of unwanted pinning. Although the flame polish was done with great care, it is difficult to obtain a perfectly parallel wedge front, and because the wedge front dictates the equilibrium crack position, this would correlate to a crack front that is not perfectly parallel to the thickness heterogeneity. This deviation from parallel would cause the energy buildup to be slightly uneven along the crack front at the heterogeneity, which may have contributed to both the spread in the measured load increase as well as the fact that the peak load increase was only a factor of 5 over the homogeneous case rather than the factor of 8 predicted by membrane separation models.

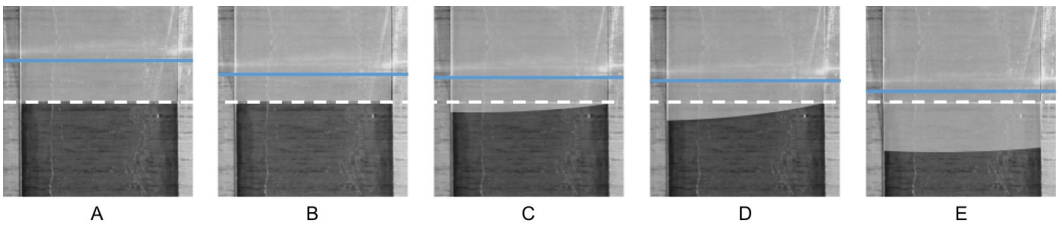

Figure 4.7: Face-view still image progression of a top-to-bottom cleavage crack interacting with a 0.03 to 0.06 mm step-wise thickness change. Images correlate to load-displacement curve positions shown in Figure 4.6. The horizontal solid blue line indicates quartz wedge position, light gray shading (enhanced for clarity) indicates the extent of the cleavage crack, and the thickness step is marked by the white dashed line.

Considering the opposite case of a decreasing thickness heterogeneity, Figure 4.8 shows the loading curve for a mica sample prepared with a step-wise thickness decrease from 0.04 to 0.01 mm. Before and after the thickness change at approximately 30 mm of displacement, the load profile remains consistent with samples of similar homogeneous thickness. Significant differences, however, are evident as the cleavage front interacts with the decrease in sample thickness. A load drop, at approximately 24 mm of displacement, occurs as the crack tip, extending ahead of the quartz wedge,

passes from relatively stiff (thick) to complaint (thin) regions. The cleavage force recovers to a plateau correlating to the predicted value for a 0.01 mm thickness after a brief transition region. The abrupt decrease in splitting force is consistent with the sudden change in compliance that would make crack propagation more favorable. However, the transition region after the jump is believed to be an artifact of the cleavage front propagating well in advance of the wedge tip; although the cleavage front has passed to the thinner region, the thickness step has yet to pass the wedge tip, which is moving at a fixed velocity. Therefore, the change in bending rigidity, which is dictated by the location of the wedge, occurs slightly later than the crack entering the thinned mica. It should be noted that the drop in strength seen in this transition region does not follow the h^3 scaling predicted by differences in flexural rigidity, but this expected because the sudden forward movement of the crack well beyond tip of the wedge indicates a deviation from the ideal equilibrium, so the analytical assessment will not necessarily be a good predictor. Regardless, an enhancement of cleavage force is not realized in this case because the transition from a stiffer material to a softer one actually allows the crack to propagate more readily rather than pinning it.

Implications for Layered Composite Materials

The increase in required force for separation along a cleavage plane in heterogeneous mica is particularly noteworthy because it shows that compliance contrast, or more explicitly a sharp increase in bending stiffness, near the crack tip can affect the force required to propagate a crack, which will manifest as a higher splitting strength. This effect of both elastic and compliance contrast on toughness have been demonstrated in various forms in softer systems, but in this study, a clear confirmation is made in a brittle system with a small cohesive zone and small splitting angles. This makes the study a promising analog to illustrate how compliance contrast or stiffness contrast could improve macroscopic toughness in brittle ceramics with layered structures.

Many layered ceramic structures rely on interfaces to deflect cracks and dissipate energy, but previous studies have also demonstrated the potential of layered ceramics with strongly bonded interfaces which could greatly benefit from the toughness gained through elastic modulus contrast. These strongly bonded, layered ceramic structures are typically composed of a hard thin brittle outer layer and a much thicker functional layer beneath that is typically more compliant and damage tolerant. These types of layered structures have been shown to be beneficial in bilayer composites, which are useful in applications such as thermal barrier coatings and dental implants,

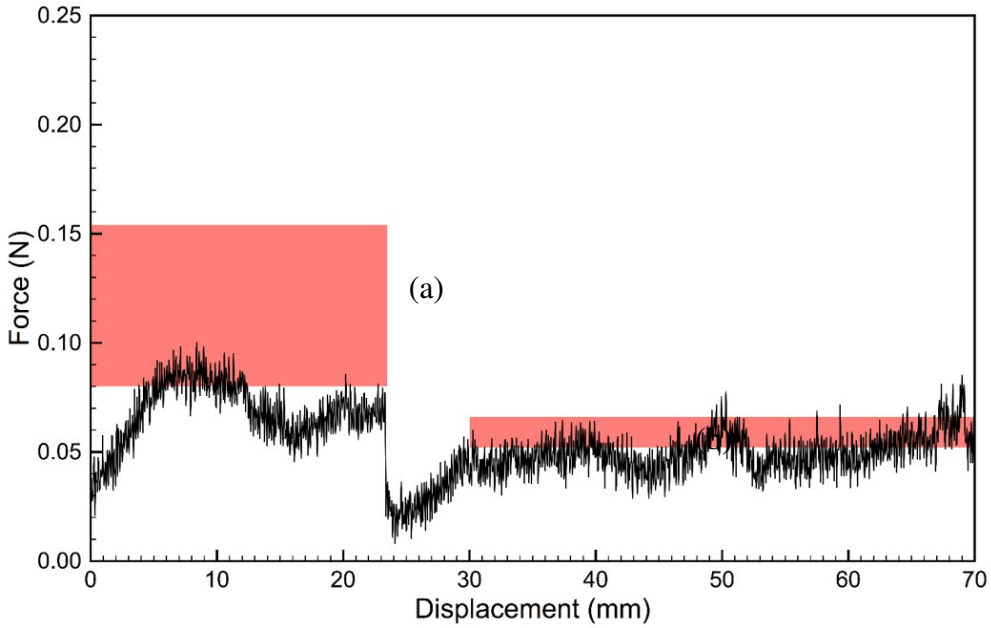

Figure 4.8: Load vs. displacement for the cleavage of mica with a thickness heterogeneity. The heterogeneity took the form of step-wise thickness decrease, from 0.04 to 0.01 mm, at approximately 30 mm of displacement. The shaded region (a) corresponds to the force required to split a homogeneous sheet of thickness 0.04 mm and the shaded region (b) corresponds to the force required to split a homogeneous sheet of thickness 0.01 mm.

where resistance to impact and indentation are critical.[23–31] However, functional layers often rely on defects and small cracks to accommodate deformations, and concerns can arise in cases where the functional layer develops cracks that are sufficiently large that it can no longer effectively accommodate mechanical loads without failing catastrophically.[23, 32] In these scenarios, the results of this study indicate that the addition of internal hard brittle layers, either as a complete layer or fractions of layers, may be of significant benefit in limiting the propagation of larger cracks in the functional layer through the presence of significant elastic contrast. If the elastic contrast is sufficiently large, the presence of these additional internal layers could increase the toughness of the composite well above the toughness of its constituent components. Furthermore, the spacing of these hard brittle layers could be adjusted to tailor the functionality of the layered composite to sufficiently resist indentation damage as well as limit the propagation of larger internal cracks. This additional toughening through elastic contrast at strong interfaces presents interesting opportunities for toughening in layered ceramic composites that are, to date, not well

investigated.

Implications for Designed Asymmetry

In the context of designed anisotropy, muscovite mica with added thickness variations also demonstrates how heterogeneous structure can be used to create directionally-dependent macroscopic fracture properties. Based on analytical assessments of membrane separation, the peak wedge splitting force measured across a thickness heterogeneity scales with the cube of the magnitude of the thickness difference in the ideal case. But even with deviations from ideality, the scaling is still some exponential of the height difference that is larger than 1. This nonlinear scaling is important because if macroscopic fracture toughness is considered to scale with the maximum splitting force, then a heterogeneous mica specimen with two separate 0.3 mm thickness increases should exhibit lower macroscopic toughness than a specimen with one 0.6 mm thickness increase. This same argument could also be applied in reverse to the compliance changes associated with a decreases in thickness. Logical extension of this leads to the argument that the macroscopic toughness anisotropy of the mica sheet could be maximized by introducing a large thickness increase followed by many small, consecutive thickness decreases. This design would maximize the peak splitting force and minimize the subsequent load drop in one direction, while minimizing peak force and maximizing load drop in the other direction, all while keeping the crack constrained to stable, continuous growth in a single fracture plane.

Attempts were made to demonstrate this directional anisotropy within one mica sheet in a single experiment, but it proved infeasible, as uniform mica sheets of sufficient length could not be produced, so it was not possible to achieve steady state propagation after each heterogeneity and get accurate measurements of splitting strength. Attempts were made to achieve this effect in larger sheets of natural mica (Ward's Science, Rochester, NY) rather than sectioned sheets for atomic force microscopy (V-1 quality, Electron Microscopy Sciences, Hatfield, PA, USA), but these natural sheets had too many natural defects and pinning sites to be suitable for fracture study. Finally, a similar exploration of this topic was done in the context numerical simulations of idealized heterogeneous media with equivalent toughnesses and different stiffnesses.[19] Similar multi-material studies may also be possible in the context of mica by filling in thickness variations with a resin or other soft phase, but steps must be taken to prevent the second phase from infiltrating over the top of or between mica layers. However, even without the addition of a second phase, these experiments on muscovite mica readily demonstrate that compliance

contrast can directly improve both the strength and toughness of a brittle composite structure as well as introduce toughness anisotropy that is dependent on the direction of propagation of the crack within a singular orientation.

4.4 Summary

Following an experimental procedure inspired by Obreimoff, muscovite mica specimens were separated along cleavage planes under displacement controlled conditions using a polished quartz wedge. The force required for separation was measured, and related to the critical energy release rate, a combination of the surface energy and elastic bending energy of the cleaved mica sheet. Homogeneous mica separation was performed for a variety of sheet thicknesses to establish the baseline thickness dependence. These observations were then applied to investigate the behavior of heterogeneous mica sheets with designed, step-wise thickness heterogeneities.

In mica prepared with thickness heterogeneities, a dramatic increase in required separation force occurred when the mica splitting front encountered the thickness increase in the mica sheet. This force enhancement is associated with a change in flexural rigidity of the cleaved mica sheet, and the increase in force observed is significantly larger than the splitting force required for the homogeneous constituents.

The results of this study indicate that compliance contrast near the tip of a crack can dramatically alter the magnitude of the required driving force to propagate a crack, which will manifest as an increase in macroscopic fracture toughness. This phenomenon could prove to be of significant benefit in layered ceramic composites with strongly bonded interfaces where more compliant layers are used beneath high-stiffness brittle layers to absorb damage from impact and indentation. This study suggests that the incorporation of additional high-stiffness layers may serve to mitigate crack growth and improve failure strength. Additionally, these studies of heterogeneous structures in mica demonstrate the potential for macrosopic improvements of toughness in ceramic composites through the introduction of elastic contrast or compliance contrast. This same elastic and compliance contrast can also be used to introduce toughness properties that are dependent on the direction of crack propagation.

REFERENCES

[1] M.T. Johnson, N.R. Brodnik, T. Ekeh, K. Bhattacharya, and K.T. Faber. Obreimoff revisited: Controlled heterogeneous fracture through the splitting of mica. *Mechanics of Materials*, 136:103088, sep 2019. ISSN 0167-6636. doi: 10.1016/J.MECHMAT.2019.103088. URL https://www.sciencedirect.com/science/article/pii/S0167663618307543?dgcid=author.

[2] Brian R. Lawn. *Fracture of brittle solids*. Cambridge University Press, 1993. ISBN 9780511623127.

[3] A. A. Griffith. The Phenomena of Rupture and Flow in Solids. *Philosophical Transactions of the Royal Society A: Mathematical, Physical and Engineering Sciences*, 221(582-593):163–198, jan 1921. ISSN 1364-503X. doi: 10.1098/rsta.1921.0006. URL http://rsta.royalsocietypublishing.org/cgi/doi/10.1098/rsta.1921.0006.

[4] J. W. Obreimoff. The Splitting Strength of Mica. *Proceedings of the Royal Society of London A*, 25:290–297, 1930. ISSN 1364-5021. doi: 10.1098/rspa.1933.0074.

[5] Lawn B. R. Roach, D. H., Hueckeroth, D. M. Crack Velocity Thresholds and Healing in Mica. *Journal of Colloid and Interface Science*, 114(1):292–294, 1986.

[6] Kai-tak Wan, Nicholas Aimard, S Lathabai, Roger G Horn, and Brian R. Lawn. Interfacial energy states of moisture-exposed cracks in mica. *Journal of Materials Research*, 5(1):172–182, 1990. ISSN 08842914. doi: 10.1557/JMR.1990.0172.

[7] Kai-Tak Wan, Douglas T. Smith, and Brain R. Lawn. Fracture and Contact Adhesion Energies of Mica-Mica, Silica-Silica, and Mica-Silica Interfaces in Dry and Moist Atmospheres. *Journal of the American Ceramic Society*, 75 (3):667–676, mar 1992. ISSN 0002-7820. doi: 10.1111/j.1151-2916.1992.tb07857.x. URL http://doi.wiley.com/10.1111/j.1151-2916.1992.tb07857.x.

[8] Hiroshi Okusa, Kazue Kurihara, and Toyoki Kunitake. Chemical Modification of Molecularly Smooth Mica Surface and Protein Attachment. Technical report, 1994. URL https://pubs.acs.org/sharingguidelines.

[9] Hong Yang, Alex Kuperman, Neil Coombs, Suzan Mamiche-Afara, and Geoffrey A. Ozin. Synthesis of oriented films of mesoporous silica on mica. *Nature*, 379(6567):703–705, feb 1996. ISSN 0028-0836. doi: 10.1038/379703a0. URL http://www.nature.com/articles/379703a0.

[10] Rivlin R. S. The Effective work of adhesion Experiments with Adhesive Tape. *Paint Technology*, IX(106):2611–2614, 1944.

[11] K Kendall. Thin-film peeling-the elastic term. *Journal of Physics D: Applied Physics*, 8(13):1449–1452, sep 1975. ISSN 0022-3727. doi: 10.1088/0022-3727/8/13/005. URL http://stacks.iop.org/0022-3727/8/i=13/a=005?key=crossref.1fe0609b9b564ad02f86ea972699bc29.

[12] S. Xia, L. Ponson, G. Ravichandran, and K. Bhattacharya. Toughening and Asymmetry in Peeling of Heterogeneous Adhesives. *Physical Review Letters*, 108(19):1–5, may 2012. ISSN 0031-9007. doi: 10.1103/PhysRevLett.108.196101. URL https://link.aps.org/doi/10.1103/PhysRevLett.108.196101.

[13] S.M. Xia, L. Ponson, G. Ravichandran, and K. Bhattacharya. Adhesion of heterogeneous thin films—I: Elastic heterogeneity. *Journal of the Mechanics and Physics of Solids*, 61(3):838–851, mar 2013. ISSN 0022-5096. doi: 10.1016/J.JMPS.2012.10.014. URL https://www.sciencedirect.com/science/article/pii/S0022509612002359.

[14] S.M. Xia, L. Ponson, G. Ravichandran, and K. Bhattacharya. Adhesion of heterogeneous thin films II: Adhesive heterogeneity. *Journal of the Mechanics and Physics of Solids*, 83:88–103, oct 2015. ISSN 0022-5096. doi: 10.1016/J.JMPS.2015.06.010. URL https://www.sciencedirect.com/science/article/pii/S0022509615001593.

[15] A Majumder, S Mondal, A K Tiwari, A Ghatak, and A Sharma. Direction specific adhesion induced by subsurface liquid filled microchannels. *Soft Matter*, 8(27):7228–7233, 2012. ISSN 1744683X (ISSN). doi: 10.1039/c2sm25507c. URL http://www.scopus.com/inward/record.url?eid=2-s2.0-84869594034{\&}partnerID=40{\&}md5=ff1ba1eafe4330c24c1a2f4598ac51d8.

[16] Animangsu Ghatak. Peeling off an adhesive layer with spatially varying topography and shear modulus. *Physical Review E - Statistical, Nonlinear, and Soft Matter Physics*, 89(3):1–6, 2014. ISSN 15502376. doi: 10.1103/PhysRevE.89.032407.

[17] J. Gonzalez and J. Lambros. Crack Path Selection in Microstructurally Tailored Inhomogeneous Polymers. *Experimental Mechanics*, 53(4):619–634, apr 2013. ISSN 0014-4851. doi: 10.1007/s11340-012-9668-3. URL http://link.springer.com/10.1007/s11340-012-9668-3.

[18] Neng Wang and Shuman Xia. Cohesive fracture of elastically heterogeneous materials: An integrative modeling and experimental study. *Journal of the Mechanics and Physics of Solids*, 98:87–105, jan 2017. ISSN 0022-5096. doi: 10.1016/J.JMPS.2016.09.004. URL https://www.sciencedirect.com/science/article/pii/S0022509616303313.

[19] M. Z. Hossain, C. J. Hsueh, B. Bourdin, and K. Bhattacharya. Effective toughness of heterogeneous media. *Journal of the Mechanics and Physics of Solids*, 71(1):15–32, 2014. ISSN 00225096. doi: 10.1016/j.jmps.2014.06.002. URL http://dx.doi.org/10.1016/j.jmps.2014.06.002.

[20] C-J. Hsueh, L. Avellar, B. Bourdin, G. Ravichandran, and K. Bhattacharya. Stress fluctuation, crack renucleation and toughening in layered materials. *Journal of the Mechanics and Physics of Solids*, 120:68–78, nov 2018. ISSN 0022-5096. doi: 10.1016/J.JMPS.2018.04.011. URL https://www.sciencedirect.com/science/article/pii/S0022509617311407.

[21] C. Kovalchick, A. Molinari, and G. Ravichandran. An experimental investigation of the stability of peeling for adhesive tapes. *Mechanics of Materials*, 66: 69–78, nov 2013. ISSN 0167-6636. doi: 10.1016/J.MECHMAT.2013.07.012. URL https://www.sciencedirect.com/science/article/pii/S0167663613001415.

[22] J. G. Williams. Friction and plasticity effects in wedge splitting and cutting fracture tests. *Journal of Materials Science*, 33(22):5351–5357, November 1998. ISSN 1573-4803. doi: 10.1023/A:1004490015211. URL https://doi.org/10.1023/A:1004490015211.

[23] Brian R. Lawn. Indentation of Ceramics with Spheres: A Century after Hertz. *Journal of the American Ceramic Society*, 81(8):1977–1994, jan 1998. ISSN 00027820. doi: 10.1111/j.1151-2916.1998.tb02580.x. URL http://doi.wiley.com/10.1111/j.1151-2916.1998.tb02580.x.

[24] Haiyan Liu, Brian R. Lawn, and Stephen M. Hsu. Hertzian Contact Response of Tailored Silicon Nitride Multilayers. *Journal of the American Ceramic Society*, 79(4):1009–1014, apr 1996. ISSN 0002-7820. doi: 10.1111/j.1151-2916.1996.tb08540.x. URL http://doi.wiley.com/10.1111/j.1151-2916.1996.tb08540.x.

[25] Antonia Pajares, Lanhua Wei, Brian R. Lawn, and Christopher C. Berndt. Contact Damage in Plasma-Sprayed Alumina-Based Coatings. *Journal of the American Ceramic Society*, 79(7):1907–1914, jul 1996. ISSN 0002-7820. doi: 10.1111/j.1151-2916.1996.tb08012.x. URL http://doi.wiley.com/10.1111/j.1151-2916.1996.tb08012.x.

[26] Antonia Pajares, Lanhua Wei, Brian R. Lawn, Nitin P. Padture, and Christopher C. Berndt. Mechanical characterization of plasma sprayed ceramic coatings on metal substrates by contact testing. *Materials Science and Engineering: A*, 208(2):158–165, apr 1996. ISSN 0921-5093. doi: 10.1016/0921-5093(95)10071-7. URL https://www.sciencedirect.com/science/article/pii/0921509395100717.

[27] A C Fischer-Cripps, B R Lawn, A Pajares, and L Wei. Stress Analysis of Elastic-Plastic Contact Damage in Ceramic Coatings on Metal Substrates.

Journal of the American Ceramic Society, 79(10):2619–2625, aug 1996. ISSN 00027820. doi: 10.1111/j.1151-2916.1996.tb09024.x. URL http://dx.doi.org/10.1111/j.1151-2916.1996.tb09024.x.

[28] Linan An, Helen M. Chan, Nitin P. Padture, and Brian R. Lawn. Damage-resistant alumina-based layer composites. *Journal of Materials Research*, 11(01):204–210, jan 1996. ISSN 0884-2914. doi: 10.1557/JMR.1996.0025. URL http://www.journals.cambridge.org/abstract{_}S0884291400022214.

[29] Donald M. Baskin, Michael H. Zimmerman, K. T. Faber, and Edwin R. Fuller. Forming Single-Phase Laminates via the Gelcasting Technique. *Journal of the American Ceramic Society*, 80(11):2929–2932, nov 1997. ISSN 0002-7820. doi: 10.1111/j.1151-2916.1997.tb03213.x. URL http://doi.wiley.com/10.1111/j.1151-2916.1997.tb03213.x.

[30] Sataporn Wuttiphan, Antonia Pajares, Brian R. Lawn, and Christopher C. Berndt. Effect of substrate and bond coat on contact damage in zirconia-based plasma-sprayed coatings. *Thin Solid Films*, 293(1-2):251–260, jan 1997. ISSN 0040-6090. doi: 10.1016/S0040-6090(96)08992-4. URL https://www.sciencedirect.com/science/article/pii/S0040609096089924.

[31] John K. Montgomery and K. T. Faber. Processing and Surface Flaw Tolerance of Alumina Bilayers. *Journal of the American Ceramic Society*, 88(2):287–292, feb 2005. ISSN 0002-7820. doi: 10.1111/j.1551-2916.2005.00073.x. URL http://doi.wiley.com/10.1111/j.1551-2916.2005.00073.x.

[32] Sataporn Wuttiphan, Brian R. Lawn, and Nitin P. Padture. Crack Suppression in Strongly Bonded Homogeneous/Heterogeneous Laminates: A Study on Glass/Glass-Ceramic Bilayers. *Journal of the American Ceramic Society*, 79 (3):634–640, apr 1996. ISSN 00027820. doi: 10.1111/j.1151-2916.1996.tb07922.x. URL http://doi.wiley.com/10.1111/j.1151-2916.1996.tb07922.x.

Chapter 5

EXTENSION INTO CERAMICS: 3D PRINTING WITH PRECERAMIC POLYMERS

The work in this chapter is based the publication “Analysis of Multi-scale Mechanical Properties of Ceramic Trusses Prepared from Preceramic Polymers" by N.R. Brodnik, J. Schmidt, P. Colombo, and K.T. Faber, which is currently under review in Additive Manufacturing. N.R. Brodnik and J. Schmidt shared first authorship in this work, with N.R. Brodnik taking lead on sample and testing design, and J. Schmidt taking lead on sample fabrication. Both N.R. Brodnik and J. Schmidt contributed to mechanical testing of samples. The details of the print resin and fabrication process used in this study are discussed in reference [1].

5.1 Introduction

In the previous chapter, the potential for designed anisotropy through compliance contrast was demonstrated in a model ceramic system, mica, where stable crack growth can be readily achieved using wedge splitting.[2, 3] While mica is a good ceramic system for stable crack growth coupled with elastic contrast, the possibilities for the introduction of designed anisotropy are relatively limited. To explore greater design possibilities in ceramics, we return to stereolithography as a means to introduce a degree of structural control that cannot be provided by conventional ceramic processing. However, instead of using acrylate photopolymers, we instead use preceramic photopolymers, which can be converted into silicon-based ceramics via pyrolysis.

To date, both stereolithography and digital light processing of preceramic polymer resins have been used to produce a variety of complex structures, and improvements to both the printing and conversion processes indicate there is potential for these systems to begin transitioning into industrial applications.[1, 4–7] However, if preceramic polymer 3D printing, or any other ceramic additive manufacturing technique, is going to prove viable in an industrial setting, it is critical to understand how the complex geometries afforded by 3D printing will affect the properties of the resultant ceramic structure. This effect must be understood both in the context of transformation of the printed part into a ceramic body and in the mechanical response of that ceramic body. Previous analyses on preceramic polymer printing systems across

multiple additive manufacturing methods have been restricted to characteristics of the printing resin itself, printing parameters, ceramic yield, and overall linear shrinkage of representative ceramic bodies.[8–12] In cases where mechanical properties were analyzed, compression tests on bulk structures and flexural tests on representative bodies are most common (e.g. bend beams, discs), and little consideration is given to complex structures.[5, 10, 13–16] Furthermore, even characterization of representative solid bodies is somewhat limited, as the size of bulk structures that can be produced by ceramic additive manufacturing is limited by the available conversion processes, which are diffusion mediated.

In this sense, a mechanical investigation of designed ceramic structures made from printed preceramic polymers can serve two purposes. Not only can stereolithography of preceramic polymers be used to investigate the effects of designed anisotropy, but the introduction of complex design can also be used to better understand the effects of structure on the mechanical properties in printed silicon oxycarbide (SiOC) ceramics, going well beyond what has been explored with simple representative bodies. However, exploration of large bulk structures in this manner is still limited by diffusion-governed ceramic conversion processes. This can be addressed by instead examining lattice structures, which have relatively small solid features, but still demonstrate complex structure at multiple length scales as well as deformation and failure behavior that is structure dependent. The exploration of lattice structures as materials is not a new concept, as many mechanical metamaterials use varieties of interchanging truss structures to tailor elastic deformation behavior at both the macro and micro scales.[17, 18] However, the exploration of interchanging truss structures in the context of failure behavior is not well investigated.

To explore the effect of complex design on ceramics made from printed preceramic polymers, truss structures measuring multiple centimeters in size were printed in different geometric arrangements, and the mechanical properties of not only the pyrolyzed SiOC lattice but also the individual beam elements were analyzed in detail along with the effects of the pyrolysis process on resultant geometry. Two different lattice structures were produced: a Kelvin cell structure which deforms through beam bending, as well as an octet cell structure which deforms through beam stretching. Additionally, to explore the potential for designed anisotropy, a mixed structure was designed to incorporate these two beam configurations within one structure with uniform cell size and stiffness, taking advantage of the possibility to control beam element positioning as well as specific structure deformation modes. If the stiffness

can be matched between different truss unit cell elements, it should be possible to create a structure with uniform elastic behavior, but failure strength that varies on an element by element basis due to differences in deformation, and consequently, failure mode. This would allow for control of fracture behavior at the level of failure strength, and the arrangement of different unit cells in the mixed structure could be used to control the direction of crack propagation.

5.2 Methods

Sample Fabrication

The preceramic printing resin used in this work was based on a selected physical blend of preceramic polymers, discussed in detail by Schmidt and Colombo.[1] The photocurable siloxane TEGO RC 711 (Evonik Industries, Germany) was mixed in equal parts in weight with the high ceramic yield silicone resin H44 (Wacker Chemie A.G., Germany), which was previously dissolved in toluene at a 3/1 weight ratio of solvent/solid polysiloxane. The resin was printed using a digital light processing printer (3DLPrinter-HD 2.0, Robofactory, Italy), which operates in the visible light wavelength range of 400-500 nm. The printed samples were then pyrolyzed in an alumina tube furnace (Carbolite CTF 17/300) at 1000 °C for 1 hour in argon with a temperature ramp of 2 °C/min. During the pyrolysis process, the preceramic polymer blend used in this study exhibits an isotropic linear shrinkage of 51.5 ± 3.3% when measured on representative solid bodies.[1]

Four different structures with overall dimensions of 30 x 30 x 60 mm^3 were designed, each consisting of 7 x 7 x 14 unit cells: two Kelvin cell structures with different beam diameters to explore the effect of aspect ratio in a fixed design, one octet cell structure to explore different deformation modes, and one mixed structure, which combined unit cells from the thick beam Kelvin and octet designs in parallel (see Figure 5.1). Although more complex designs would be desirable to explore, a proof of concept using two different structures in parallel can still demonstrate the potential for matching elastic moduli with different deformation and failure modes. Beam diameters, beam lengths, and unit cell sizes can be seen in Table 5.1. All dimensions listed are for the as-printed state, and all samples in this study will be referenced using their as-printed dimensions, as these were the dimensions that are the most consistent and readily controlled.

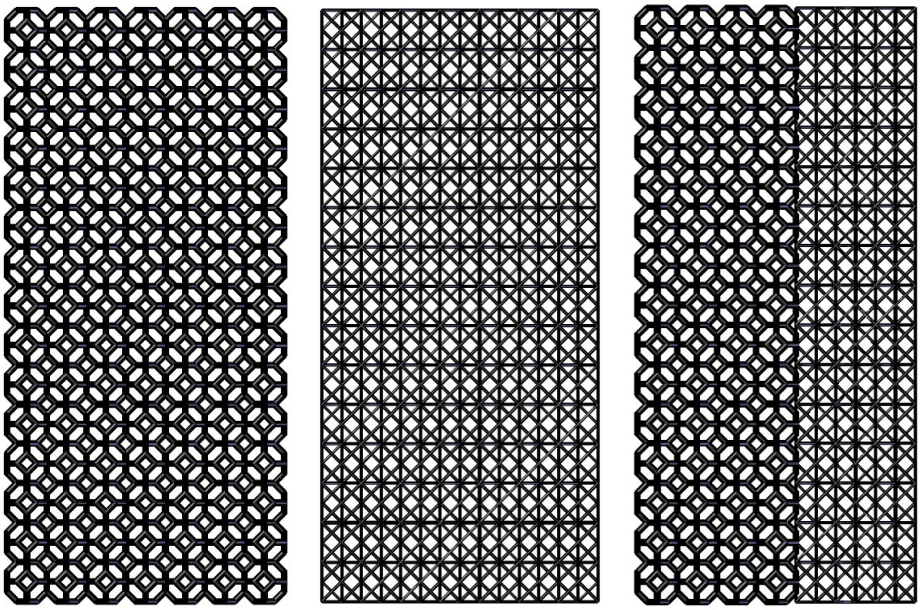

(a) Kelvin Cell Design (b) Octet Cell Design (c) Mixed Cell Design

Figure 5.1: Planar views of the design files for the truss structures investigated. The width of each design is 30 mm and the height is 60 mm.

Table 5.1: Dimensions of as-printed truss designs. Mixed cell designs in this study used a combination of Thick Beam Kelvin Cells and octet Cells.

	Kelvin (Thin Beam)	Kelvin (Thick Beam)	Octet
Beam Diameter (mm)	0.6	0.7	0.34
Beam Length (mm)	1.5	1.5	3.0
Unit Cell Size (mm)	4.2	4.2	4.2

5.3 Mechanical Characterization

Print Geometries

Morphological characterization of the printed structures was performed using optical camera (D7500, AF-S Micro Nikkor 40mm Lens, Nikon, Tokyo, Japan), stereo-microscopy (STEMI 2000-C, Zeiss, USA), and electron microscopy (Zeiss 1550 VP FE SEM, Carl Zeiss AG, Oberkochen, Germany). To investigate the shrinkages, bulk dimensional values of the structures were measured with a manual digital caliper, while the dimensions of the individual beams were obtained from SEM images analyzed with ImageJ [19] software at several locations.

Truss Structures

To characterize the mechanical properties of the truss systems, two separate sets of mechanical tests were performed: uniaxial compression on entire truss structures, and tensile beam bending (3-point) on individual truss elements. All mechanical tests were performed using an Instron 5982 mechanical testing machine (Instron, Norwood, MA). Uniaxial compression testing on complete truss structures was done at a constant displacement rate of 0.1 mm/min, to ensure stable quasi-static loading. The elastic moduli of the samples was taken from stress-strain curves of the mechanical compression tests after accounting for fixture compliance.

For uniaxial compression tests, to ensure proper contact over the whole loading area, samples were cut on the top and bottom using a diamond wafering blade in an Isomet 5000 saw (Buehler Inc.). This cut was made through consecutive nodes in the truss system to minimize the occurrence of partial truss cells at the contact surface, which could potentially cause uneven loading or early failure due to contact stresses. In addition to this, to account for load eccentricity, sets of spherical washers were placed on either side of the specimen to allow for a small amount of rotation of load surfaces during compression, as shown in Figure 5.2a.

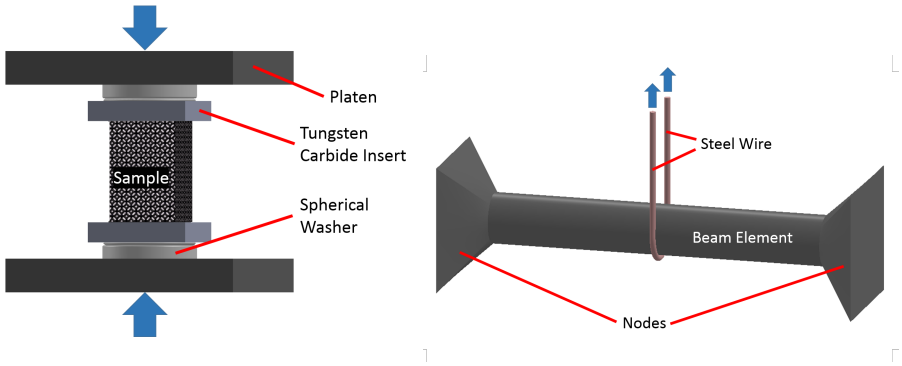

(a) Uniaxial Compression (b) Beam Flexure

Figure 5.2: Schematics of the mechanical tests used to characterize the truss structures in this study.

Beam Elements

For the flexural tests on individual beams, a test setup was adapted from the work by Brezny et al., which investigated the strength of struts in open-cell foams of alumina and zirconia.[20] The truss structures were mounted in a small-scale bench vice and oriented so that the tested beams were arranged horizontally with respect to the loading axis. A low-carbon steel wire with a diameter of 35.56 µm was looped under

the center of a single beam and then attached to a tensile fixture on the load frame. This wire was then pulled at a constant displacement rate of 1.0 mm/min to create a tension-driven 3-point bending configuration, as shown in Figure 5.2b.

For flexural testing of individual beam elements, the determination of strength is fairly straightforward. Per ASTM C 1684,[21] the strength of cylindrical rod in 3-point flexure can be described as:

$$\sigma = \frac{8PL}{\pi D^3} \tag{5.1}$$

where P is the load on the beam (exerted by the wire looped underneath the beam), L is the length of the beam, and D is the diameter. Because this test setup uses a looped wire to apply the bending force, a large amount of compliance is expected during testing. This compliance from the testing fixture made determination of elastic modulus from this test infeasible, as modulus measurement error was too high. Instead, the elastic modulus of the SiOC composing the individual beam elements was established using load controlled nanoindentation with a Berkovich tip as developed by Oliver and Pharr.[22]

Analytical Methods for Design of Mixed Structures

Across all mechanical tests, in order for different truss structures to be compared meaningfully, differences in beam geometry and arrangement had to be properly considered. Particularly, in order for truss elements with different deformation modes to be readily interchangeable, the elastic moduli of different unit cells had to match for the same loading conditions. This is best achieved using analytical descriptions of the truss structures, which allow for comparison of failure strengths and elastic moduli for across different densities and beam arrangements. For uniaxial compression tests, all stresses and strains are calculated as engineering stresses and strains using the outer dimensions of the truss structure, including internal porosity. To make these structures mechanically compatible, their effective elastic moduli have to be expressed as a function of beam size and arrangement.

The Kelvin cell structure deforms by bending of beams in the structure that are at a 45° angle with respect to the loading axis. As such, the elastic modulus of the truss structure was determined using calculations developed by Zhu et al. [23] for bending-dominant open cell foams with tetrakaidecahedral (truncated octahedral) cells. For these cell structures, the elastic modulus is equivalent along all axes of the cubic unit cell, and can be expressed in the form:

$$E_{001} = \frac{6\sqrt{2}E_S I}{L^4\left(1 + 12\frac{I}{AL^2}\right)} \tag{5.2}$$

where E_S is the elastic modulus of the solid material, I is the moment of inertia of the beams along the axis of bending, L is the length of a single beam, and A is the cross-sectional area of a single beam. In the case of both this investigation as well as the calculations by Zhu et al., the Kelvin cells are regular truncated octahedra, so all beams in the cell have the same length, cross-sectional area, and moment of inertia.

For the octet structure, deformation from loading along the z-axis of the cubic unit cell is dominated by the stretching of beams orthogonal to the load direction. The elastic modulus of this structure was described by Deshpande et al. in terms of the relative density of the lattice.[24] In this case, the stiffness of the octet-truss lattice along the (001) direction can be described using the equation:

$$E_{001} = \frac{\overline{\rho}}{5}E_S \tag{5.3}$$

where E_S is again the elastic modulus of the solid material and $\overline{\rho}$ is the relative density of the octet-truss material, which is described as follows:

$$\overline{\rho} = 6\sqrt{2}\pi\left(\frac{R}{L}\right)^2 \tag{5.4}$$

where R is the radius and L the length of a single beam.

Finally, for the design of the mixed structure, several considerations had to be made in its design in order to properly characterize its mechanical behavior. In order for a structure composed of a mixture of octet and Kelvin cells to be printed and reasonably characterized, the two different cells had to have the same unit cell size so they could be readily interchanged, as described in Table 1. Additionally, to minimize eccentric or non-uniform loading due to the arrangement of different cells in the mixed structure, the beams were printed such that the elastic modulus of both as-printed cells, Kelvin and octet, would be equivalent during uniaxial compression. Beam dimensions were established by equating the modulus descriptions of the Kelvin and octet designs to produce the relation:

$$\frac{4}{5}\left(\frac{L_k^4}{R_k^4} + 3\frac{L_k^2}{R_k^2}\right) = \left(\frac{L_o^2}{R_o^2}\right) \tag{5.5}$$

where L_k and R_k are the length and the radius of the beams in the Kelvin cells and L_o and R_o are the length and radius of the beams in the octet structure. This equation can be further simplified by relating the beam lengths between the two structures. Because the Kelvin and octet cells are both regular structures with equivalent unit cell sizes, some straightforward geometry shows that beams in the octet structure are exactly twice the length of beams in the Kelvin structure, so $2L_k = L_o$. Substituting this into Equation 5.5 and simplifying produces the following relation.

$$\left(\frac{L_k^2}{R_k^2} + 3\right) = 5\left(\frac{R_k^2}{R_o^2}\right) \tag{5.6}$$

Based on this equation, for a chosen unit cell size and beam radius in one structure, the beam radius of the other structure will be fully defined under the constraint that both structures will have the same modulus. This relation was used to design all the mixed structures in this study and also motivated the beam dimensions for the individual octet and Kelvin cells that were investigated.

5.4 Results

Printing/Pyrolysis

As previously established, the material characteristics of the preceramic printing resin were previously investigated by Schmidt and Colombo.[1] Thermogravimetric analysis showing the total mass loss of the preceramic polymer as a function of temperature is shown in Figure 5.3.[1] After pyrolysis, the ceramic yield of 40.1 wt% is a weighted average of the ceramic yields of the pure RC 711: 7.4 wt%, and H44: 76.5 wt%, and is consistent with the expected value for the resin blend, confirming a homogeneous distribution of silicone chains from both compounds within the printed structure.[1]

To verify the amorphous character of the truss structures and confirm that truss designs and beam dimensions did not affect the crystallinity of the pyrolyzed SiOC, X-Ray diffraction was performed on pulverized truss structures of each design. The X-Ray diffraction patterns of all designs are shown in Figure 5.4. Regardless of truss design, all pyrolyzed SiOC structures showed complete amorphous character with no visible crystalline domains. It should be noted though, that the intensity counts are relatively low for these structures, which arises from the relatively low atomic number of all chemical constituents of SiOC.

In all Kelvin and octet structures, no sign of delamination or crack formation was

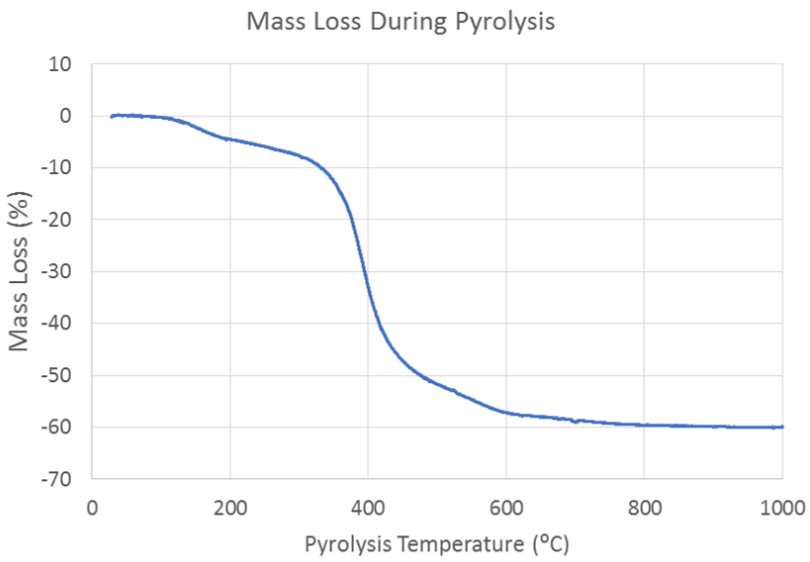

Figure 5.3: Thermogravimetric analysis showing the mass loss of the 50% RC 711 and 50% H44 preceramic polymer blend during pyrolysis as a function of heating temperature.

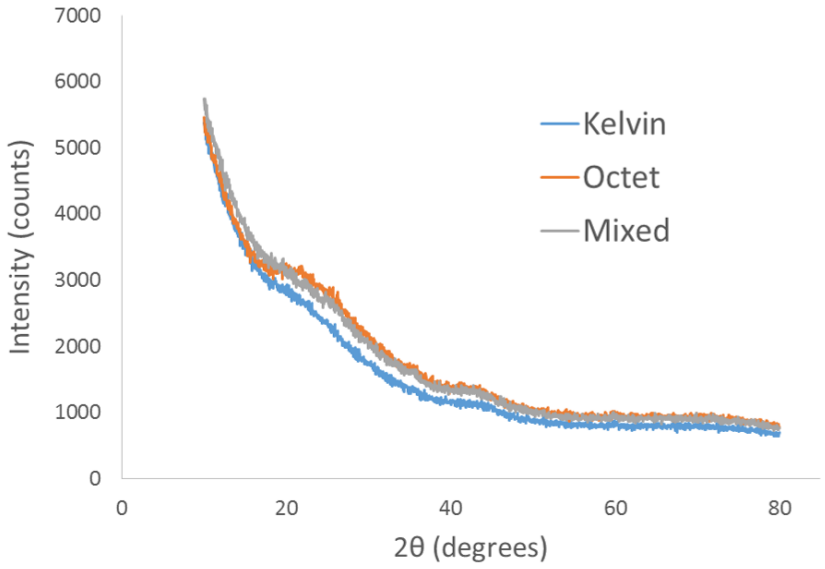

Figure 5.4: X-Ray diffraction analysis of the different truss structures, verifying uniform amorphous crystal structures across all three designs.

visible in the as-printed state. Similarly, after pyrolysis, no cracks were observed in the produced SiOC structures, which are shown in Figure 5.5. Accurate copies of the designs (shown in Figures 5.1a and 5.1b) were produced with good shape retention and relatively isotropic body shrinkage (see Table 5.2).

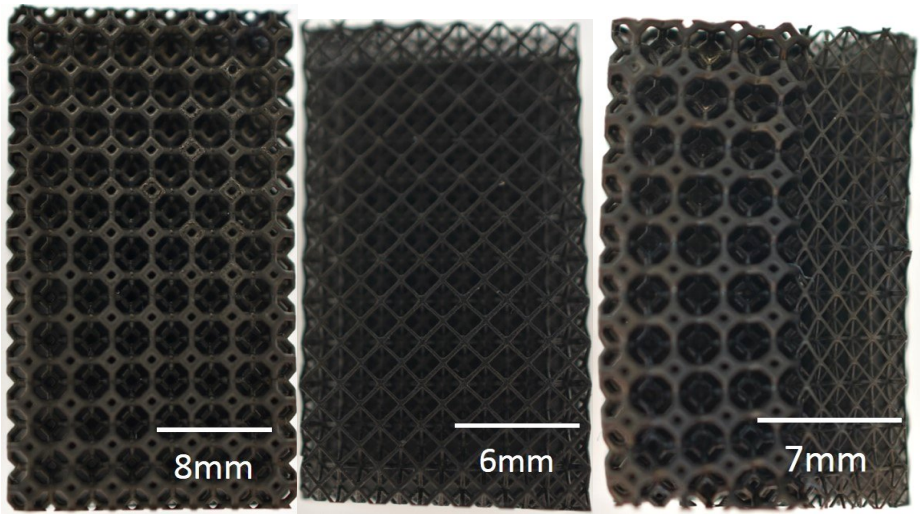

(a) Kelvin Structure (b) Octet Structure (c) Mixed Structure

Figure 5.5: Representative images of pyrolyzed and SiOC truss structures that have been prepared for uniaxial compression testing.

Table 5.2: Linear shrinkages of Kelvin and octet structures. Shrinkages measured based on total size of pyrolyzed specimens.

	Kelvin (Thin Beam)	Kelvin (Thick Beam)	Octet
X-Direction (%)	45.4 ± 1.6	43.7 ± 0.7	49.5 ± 1.4
Y-Direction (%)	44.8 ± 1.7	43.3 ± 0.8	48.8 ± 1.4
Z-Direction (%)	45.2 ± 0.8	43.4 ± 0.7	49.3 ± 1.3

Shrinkage Measurements

The linear shrinkages of the overall structures as well as their constituent elements were investigated for the two Kelvin cell structures as well as for the octet structure, and comparisons of these are shown in Table 5.3. The aspect ratio reduction is also reported, which is the percentage change in the value of (L/D) for the beam elements in each structure, where L is beam length and D is beam diameter. Even though the linear shrinkages are isotropic for each structure, the shrinkages are not the same, neither within one structure nor between different structure geometries fabricated with the same material. Moreover, all beam elements show greater shrinkage in length than in diameter, and the shrinkage of the overall structure scales with a combination of the beam length shrinkage and the geometry of the beams within the structure.

The difference in overall shrinkage between the Kelvin and octet structures means

Table 5.3: Percent shrinkages of individual beam elements and beam aspect ratios (L/D) within each of the two truss structures. Average linear shrinkage of each truss structure is shown for comparison.

	Kelvin (Thin Beam)	Kelvin (Thick Beam)	Octet
Beam Diameter Shrinkage (%)	36.9 ± 1.7	37.5 ± 1.0	44.6 ± 1.3
Beam Length Shrinkage (%)	44.9 ± 1.6	42.0 ± 0.8	67.0 ± 1.0
Beam Volume Shrinkage (%)	77.9 ± 2.4	77.3 ± 0.7	90.0 ± 0.8
Aspect Ratio Reduction (%)	12.2 ± .01	14.8 ± .05	40.3 ± .01
Structure Average Shrinkage (%)	45.1 ± 1.4	43.5 ± 0.8	49.2 ± 1.4

that the mixed structure does not exhibit isotropic shrinkage, which is apparent in Figure 5.5c. All mixed structure specimens exhibited a slight curvature towards the octet section of the structure, which exhibited an overall linear shrinkage that was larger than that of the Kelvin structure by about 6%. Despite this nonuniform shrinkage, the mixed structures, like the Kelvin and octet structures, showed no cracks within the structure nor any sign of delamination or beam separation, even at the interface between the two geometrically different parts.

Truss Structure Response: Uniaxial Compression

Table 4 lists the porosity, strength and elastic modulus measured in uniaxial compression for all truss configurations. The thick beam Kelvin cell structure demonstrated an approximately 30% increase in failure strength over the thin beam Kelvin structure at the cost of only about 4% porosity. The octet structure exhibited a significantly larger porosity than any of the other structures as well as the lowest average strength and stiffness. Since the mixed structure is partially thick beam Kelvin design and partially octet design, its porosity and strength values lie between those of the octet and Kelvin structures. The elastic modulus of the mixed structure, however, is closer to that of the thick beam Kelvin structure.

Table 5.4: Comparison of the porosities and mechanical properties of the different truss designs characterized in this study.

	Kelvin (Thin Beam)	Kelvin (Thick Beam)	Octet	Mixed
Porosity (%)	85.3 ± 0.5	81.5 ± 1.2	91.1 ± 0.4	84.3 ± 0.1
Strength (MPa)	7.7 ± 1.1	10.0 ± 1.8	3.8 ± 0.7	9.4 ± 0.4
Elastic Modulus (GPa)	2.0 ± 0.7	3.1 ± 0.6	0.9 ± 0.1	2.7 ± 0.1

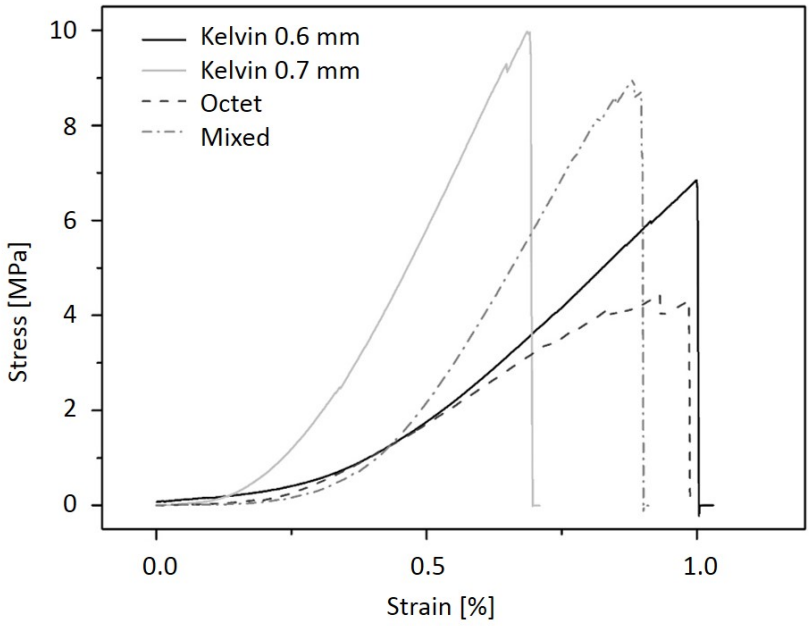

Figure 5.6: Representative uniaxial compression loading curves for each of the truss designs investigated in this study. Non-linearity at load onset is the result of spherical washer movement/alignment before load buildup.

A representative stress-strain curve for each truss structure is shown in Figure 5.6. The stress-strain curves show the typical linear elastic behavior followed by brittle fracture of a ceramic material. Besides having several local failure events, especially in the octet samples, the structures exhibited linear load buildup and catastrophic failure after peak load was reached. After failure, the fracture behavior of the Kelvin, octet, and mixed structure was analyzed using SEM fractography. Representative images of the observed fracture planes are shown in both low and high magnifications in Figure 5.7.

Fractography of all structures showed a dense SiOC material with no visible internal porosity ($\rho = 2.1\,\mathrm{g/cm^3}$). Though present, the individual print layers from the DLP printing process showed no influence on the fracture behavior, indicating that the failure strength between print layers was comparable to the strength within individual print layers and strong layer adhesion was achieved.

Beam Element Response: Flexure

The mean failure strengths, intercept failure strengths (63rd percentile), and Weibull Moduli of the individual beams in the structures are reported in Table 5.5. Two different kinds of fracture behavior were observed during the 3-point bending

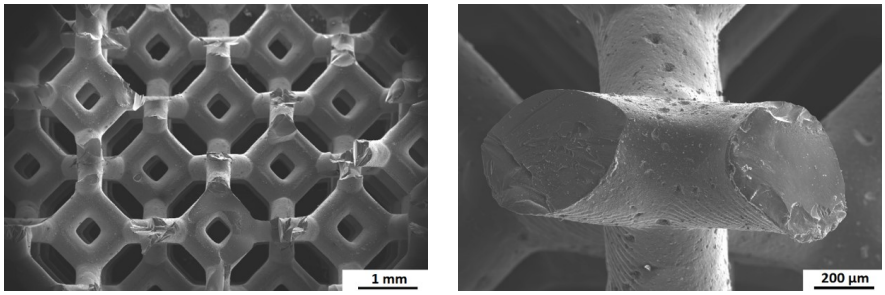

(a) Kelvin Low Magnification

(b) Kelvin High Magnification

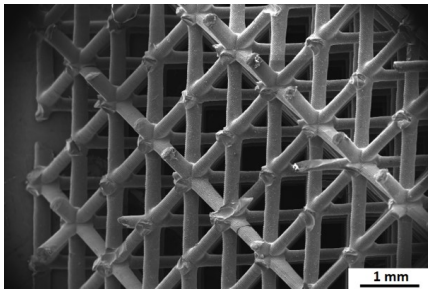

(c) Octet Low Magnification

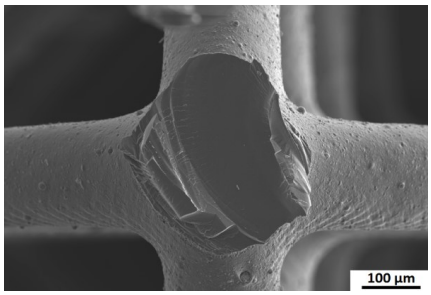

(d) Octet High Magnification

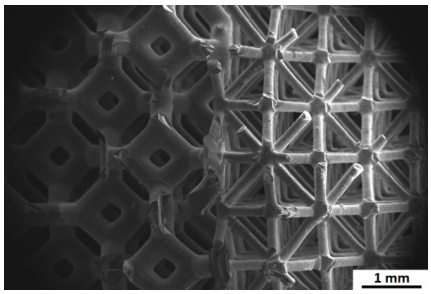

(e) Mixed Low Magnification

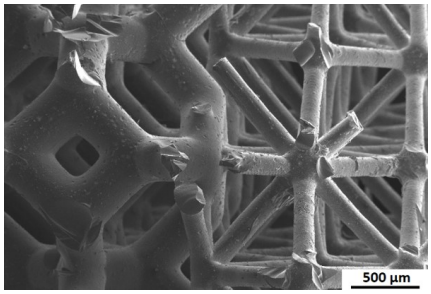

(f) Mixed High Magnification

Figure 5.7: Low and high magnification fractography images showing the failure modes of each truss system in uniaxial compression.

experiment (Figure 5.8). Figures 5.8c and 5.8f show cases of beam fracture where the nodes remain unaffected, whereas Figures 5.8b and 5.8e show beam failure where the node fractured and was partially removed with the beam. Failure both with and without node damage was observed, but no statistically significant difference in strength values was seen between the two fracture modes. The beams and cell nodes adjacent to the loaded beams remain unaffected during the experiment, providing a rigid support of the tested beams.

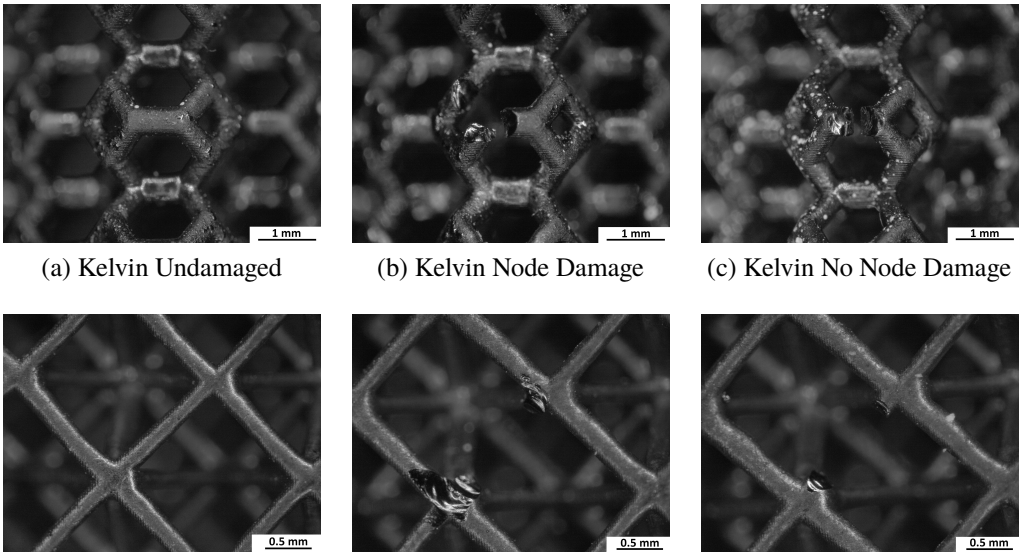

(a) Kelvin Undamaged (b) Kelvin Node Damage (c) Kelvin No Node Damage

(d) Octet Undamaged (e) Octet Node Damage (f) Octet No Node Damage

Figure 5.8: Fractography of beam pullout fracture in Kelvin and octet structures showing undamaged beams as well as pullout events with node damage and no node damage.

Table 5.5: Mean failure strengths, intercept failure strengths (63rd percentile) σ_0, and Weibull moduli of the beam elements of the Kelvin and octet truss designs. For each design, 10 beams were tested.

	Kelvin (Thin Beam)	Kelvin (Thick Beam)	Octet
Mean Failure Strength (GPa)	0.47 ± 0.16	0.54 ± 0.15	1.9 ± 0.27
σ_0 (GPa)	0.5	0.6	2.1
Weibull Modulus	3.0	3.9	8.5

5.5 Discussion

Deformation and Failure Modes

Before the mechanical responses of the ceramic structures can be properly discussed, it is critical to establish some of the principal factors that can influence truss strength and mechanical behavior. These can be separated into the categories of truss structure and porosity effects. The arrangement of beams in the truss structure dictates how the truss will deform under far-field loading, which ultimately impacts both the strength and stiffness of the structure. The truss arrangements in this study were chosen to exhibit different deformation modes, namely bending in the Kelvin structures and stretching in the octet structures. The effect of porosity in truss systems, on the other hand, is similar to that in foam structures or other porous media. Greater amounts of

porosity lead to lower strengths due to the reduced amount of load bearing solid in the body.[25]

Firstly, to understand the effects of truss structure on deformation and failure, a fractography analysis was performed, shown in Figure 5.7. In the Kelvin structure, where deformation is dominated by bending of beam elements, the fracture path proceeds in the plane normal to the loading axis, although this fracture plane did have some curvature in certain specimens. The majority of beam failures in the Kelvin structures occurred in elements that were at a 45° angle with respect to the loading axis, as these are the beams in bending when the structure is under compression. The majority of beams failed within the beam element near to a node, further indicating that the failure was ultimately flexural within each beam element.

The octet structure, which deforms by beam stretching, exhibited a markedly different behavior from the Kelvin structure. In all octet structures, failure occurred along a fracture plane at a 45° angle with respect to the loading direction. When considering the failure of individual beams, much of the fracture occurred in beams perpendicular to the loading direction, which were the elements in tension during loading of the structure. This also helps explain why global fracture of the specimen occurred along a 45° angle, as this the direction of nearest-neighbor tensile elements in the octet truss structure.

The mixed structure exhibited a combination of the fracture characteristics of both structures with respect to both fracture path and the orientation of fractured elements. The Kelvin section of the structure exhibited bending dominant failure with a fracture surface normal to the load axis and the octet section of the structure exhibited the same 45° angle failure path as the pure octet structure. The interface in the mixed structure proved to be robust, as the fracture path was not heavily influenced by the interface orientation. However, because failure was extremely rapid, it was not possible to determine whether failure events originated in the Kelvin structure or the octet structure, so the influence of deformation mode on failure behavior could not be properly evaluated.

Truss Structure Strength and Porosity

Figure 5.9 compares the strength versus the porosity on a logarithmic scale for all the lattice structures characterized in this study, and it indicates that although the strength of the octet structure is much lower than either of the Kelvin cell structures, its porosity is also significantly higher. Beyond this, there is insufficient data to

establish clear relationships of the strength scaling of either structure.

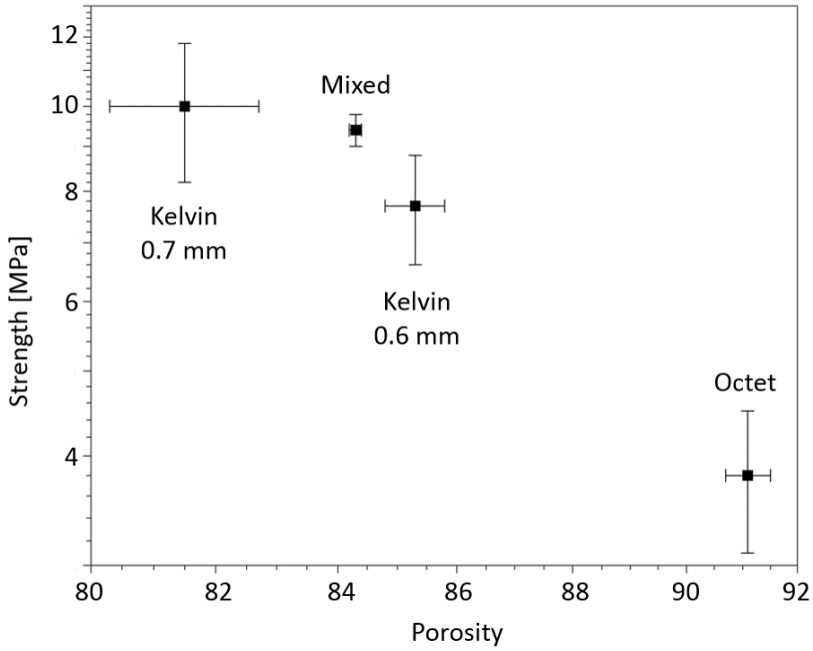

Figure 5.9: Comparison of strength and porosity between different truss designs. Both axes are plotted on a logarithmic scale.

When comparing to the mechanical strengths of other ceramic structures derived from preceramic polymers in literature, the strengths reported in this study are higher than those of SiOC structures produced by foaming or directional solidification,[26–28] but they are lower than those reported in Eckel et al.[5] for SiOC printed microlattices and honeycombs. It is suspected that much of the difference in the latter case is due to a combination of differences in truss geometry and drastic differences in specimen size and geometry, as most of the specimens tested in Eckel et al. were either of relatively small volume or were sheets with single-cell thicknesses.

Effect of Shrinkage on Mechanical Response

It is apparent from the comparison in Figure 5.9 as well as Table 5.4 that the differences in mechanical response between the different structures are at least in part a result of different shrinkage behavior. In processes involving ceramic conversion, including additive manufacturing of ceramics, it is common to report linear shrinkage values in the x, y, and z-directions, or to report overall volume shrinkage, with focus being on whether this shinkage is isotropic or has a process-dependent directionality. Beyond this, the shrinkage of complex structures is typically only considered with

respect to shape retention. Following this common trend, the linear shrinkage of the preceramic polymer blend used in this study was previously investigated on model cube structures, where it exhibited a homogeneous shrinkage of 51.5 ± 3.3 %.[1] However, a more detailed shrinkage analysis in this study found that while a representative structure can show uniform shrinkage in all directions, the constituent elements within these structures can each exhibit different shrinkage values, which change their geometry non-uniformly and lead to structure-dependent shrinkage.

Morphological analysis revealed that both Kelvin cell designs had similar structure and beam element shrinkages despite having different beam diameters. In contrast, the octet design shrank around 6% more than the Kelvin ones, and also showed a remarkable difference in beam shrinkage with an additional decrease of 13% in beam volume, 7% in beam thickness, and more than 22% in length. The similar shrinkage characteristics between the Kelvin designs and the significant difference in the octet structure suggests that the shrinkage behavior depends on the geometric arrangement. It is possible that the architecture of the truss structure puts constraints on the material's ability to freely move during the transformation from preceramic polymer into ceramic material. This constrains the shrinkage that occurs as a result of the loss of mass during pyrolysis and densification. If the nodes are hypothesized as rigid points where the beams intersect and the contraction of beams is non-uniform, then the difference in geometrical arrangement of the nodes between the Kelvin and octet structures, will influence the free shrinkage movement of the individual beams, resulting in a different overall size change between the octet and Kelvin structures.

Table 5.3 indicates that in addition to producing structure dependent shrinkage, the pyrolysis process affected beams differently depending on their aspect ratio. The octet beams, which had a much higher aspect ratio (L/D), shrank in a manner that reduced their aspect ratio far more than any of the Kelvin beams. This suggests that during pyrolysis, the systems densifies and loses mass in a manner that minimizes the surface energy of the beams, thereby reducing the aspect ratio. This makes sense logically, as it is well understood that mass loss during pyrolysis is diffusion mediated, so size reduction would be dominated by minimum diffusion distances. However, to properly characterize diffusion-dependent shrinkage, the diffusivities of the volatile species in the preceramic polymer would have to be measured, and this is both nontrivial and beyond the scope of this study.

Despite the difference seen in unit cell shrinkage between structures, the overall shrinkages of both Kelvin and octet structures are uniform in every direction and

therefore globally isotropic. This is not the case in the mixed structure, where the Kelvin and octet parts are both present, leading to non-homogeneous shrinkage. This demonstrates that even though a structure consisting of two different geometrical arrangements can be produced via additive manufacturing, special attention must be placed on the shrinkage analysis of the constituent elements, which will not necessarily match the shrinkage of representative solid bodies. Similar anisotropic shrinkage effects may also be present in ceramic additive manufacturing processes that involve a sintering step instead of a pyrolysis step, but this has been given little research attention to date. In the case of preceramic systems however, it has been demonstrated here that the shrinkage behavior of a constrained net-shape part produced via stereolithography is nontrivial, and this shrinkage must be thoroughly investigated in order for additive manufacturing to be viable for the production of complex ceramic parts for technical applications.

Beam Element Strength

The strengths of individual beam elements were investigated in this study using a testing method developed based on the work of Brezny et al.[20] When compared to the strengths of the overall truss structures, the flexural strengths of the individual beams show a markedly different trend. Despite having different structure strengths, the two Kelvin structures investigated in this study do not have individual beam strengths that are different with statistical significance. The octet structure however, which had the lowest strength of any of the truss structures investigated in this study, had beam strengths that were about four times stronger than the Kelvin beams. This difference is likely due to size effects, which can be described using the conventional weakest link model. For surface dominant flaws, this effect can be quantified using the following comparison [29]:

$$\frac{\overline{\sigma}_{\mathrm{max1}}}{\overline{\sigma}_{\mathrm{max2}}} = \left(\frac{\mathrm{k_2 A_2}}{\mathrm{k_1 A_1}}\right)^{\frac{1}{\mathrm{m}}} \tag{5.7}$$

where 1 and 2 are the different surface areas being compared, $\overline{\sigma}_{max}$ is the maximum stress in the given beam geometry, m is the Weibull modulus of the solid material, A is the beam surface area (excluding faces in contact with nodes), and k is a loading factor that changes depending on the cross section and aspect ratio of the beam being bent. Using both the post-pyrolysis beam dimensions and the average Weibull modulus value from Table 5.5 in Equation 5.7 indicates that the strength of the octet structure should be about twice that of the Kelvin structures, which explains much of

the discrepancy seen between the two systems.

Size effects can explain much of the difference in behavior between the octet and Kelvin beam elements, but not why the more slender Kelvin beams do not perform better than the thicker ones. One possible reason for this is that the effect of added beam thickness did more to improve the bending strength than the increase in volume did to reduce it. It is also possible that the lower aspect ratio of the Kelvin beams distorted the bending behavior, making the effect of volume on failure strength less apparent. Additionally, it should be noted that although the individual octet beams were extremely strong, the octet structure itself demonstrated the lowest strength of all structures tested in this study. This is a testament to the fact that weakest link behavior is governed by volume or area rather than characteristic length. Regardless of how slender the beams are, as more are introduced, the total volume and surface area of structure increase, which raises the probability of a large flaw being present in a single beam, which will ultimately lead to a reduction of strength. This effect, while simple, is less from an experimental standpoint, as beams with larger flaws would likely not be viable as standalone bodies, but could easily be part of larger truss structure, where they would greatly reduce overall strength. This subtle effect shows that even in complex architected structures, strength is still governed by the principal phenomena of porosity and geometry of the solid body.

Evaluation of Structure Elastic Modulus

For the Kelvin cell structures, the derivation from Zhu et al. (shown earlier in Equation 5.2) describes what the elastic modulus of the truss structure should be with respect to the elastic modulus of the solid material for a given beam length and radius.[23] Since all the truss structures in this study were fabricated with the same preceramic polymer blend and pyrolysis process, it is reasonable to assume that the elastic modulus of the solid SiOC ceramic is the same across all structures. This was verified through nanoindentation, and the elastic modulus of the SiOC for both the Kelvin and octet structures was found to be about 65 GPa. With this assumption and the beam dimensions measured in the shrinkage analysis, it is possible to determine the expected stiffness ratios across different structures using the following form:

$$\text{StiffnessRatio} = \frac{E_{001}^{\text{Design2}}}{E_{001}^{\text{Design1}}} \tag{5.8}$$

For the Kelvin structures, the expected stiffness ratio between designs is that the thick

beam Kelvin structure would be about twice as stiff as the thin beam Kelvin structure, but the experimental results show a ratio of about 1.5 instead. This difference is likely due to the relatively low aspect ratio of the beams in the Kelvin structures tested in this study. A print design intended to produce a high bending stiffness alongside anisotropic beam shrinkage during pyrolysis resulted in Kelvin cell beams that had aspect ratios on the order of 2:1, whereas the analytical calculation of stiffness uses the assumption of more slender beams, typically on the order of at least 5:1. This lack of slenderness would cause some of the stiffness of the Kelvin cells to be due to the deformation of the nodes, which would cause a more complex deformation behavior that deviates from the predictions established by Zhu et al.[23] using traditional beam theory. A more detailed discussion of the role of the nodes in truss structures composed of non-slender beams is discussed in Portela et al.[30]

While a lack of slenderness in beams provides a plausible explanation for the difference in stiffness ratio between the two Kelvin structures, it does not adequately explain the stiffness of the octet structures in any way. If both designs were printed to be of equal elastic modulus, based on the calculations by Deshpande et al. (shown in Equations 5.3 and 5.4), it would be expected that the octet structure would exhibit higher stiffness than either of the Kelvin structures due to the dramatic reduction in beam length during pyrolysis, which is not the case. This observation, in combination with the difference in strength between the individual octet beams and the octet structure further indicates that some eccentricity of loading may have occurred during compression, which would affect the deformation mode of the octet beams.

In the case of the mixed structures, even though shrinkage was uneven and load eccentricity is expected, a relative analysis of the expected stiffness can still be performed. Since the mixed structure is an isostrain configuration of the thick beam Kelvin and octet structures we can use the experimental modulus measurements for each of these structures along with a rule of mixtures calculation to determine the modulus of the mixed structure

$$E_{mixed} = v_{Kelvin}E_{Kelvin} + v_{octet}E_{octet} \tag{5.9}$$

where $v_{Kelvin} = \frac{4}{7}$ is the volume fraction of Kelvin cells in the mixed structure and $v_{octet} = \frac{3}{7}$ is the volume fraction of octet cells in the mixed structure. This calculation predicts an elastic modulus for the mixed structure of about 2.2 GPa, which is slightly lower than the measured 2.7 GPa. The non-uniform shrinkage of the mixed structures would make the effective fraction of Kelvin structure larger than predicted

from as-printed geometries, which would result in an increase in elastic modulus. Additionally, the curvature of the mixed structure would make the load bearing portion of the octet structure even smaller, further increasing the influence of the Kelvin structure on the elastic modulus.

Potential for Mixed Structures

Although the mixed structures in this study had load eccentricity and bending due to non-uniform shrinkage during pyrolysis, it is still worthwhile to assess the potential implications for these types of mixed structures. Previously, many different truss systems have been designed to create bulk structures with a variety of different mechanical, optical, or acoustic properties. Often referred to as metamaterials, these types of structures can be designed to have properties that normal solids cannot exhibit, such as high acoustic dampening, negative coefficients of thermal expansion, or nonuniform mechanical response, as outlined in reviews by Deshpande et al. and Wegener et al.[31, 32] Experimentally, many different trusses have been fabricated using additive manufacturing techniques such as 3D printing, but mechanical characterization of these structures has generally been limited to the elastic regime, with almost no consideration of failure mechanisms.[31–34]

However, ceramic truss structures present an interesting opportunity mechanically as materials with designed anisotropic structure, as the only mechanical responses they tend to exhibit are elastic deformation and brittle fracture. If one could design a ceramic truss system composed of compatible truss structures with different deformation modes but identical elastic moduli, it could in theory produce a structure with uniform bulk elastic properties but very controlled and specified failure. Due to differences in beam deformation behavior, it would be expected that, despite having identical stiffnesses, one truss structure in this mixed material would have a lower failure strength than the other, which would mean that when the bulk structure was loaded, the cells of the weaker structure would fail preferentially. In experimental practice, this behavior would even be expected in the case of different structures in parallel. If both truss elements have the same stiffness, and are loaded in parallel, it would be expected that the elements with lower strength would fail first, and fracture behavior would be dictated the location and distribution of the lower strength truss elements. However, in this study, failure in mixed structures was too rapid for the origin of failure to be characterized. While the idea of pairing compatible truss designs to tailor elastic deformation has been explored previously, using differences in deformation modes to drive and control failure in trusses has to date not been well

investigated.[18] A design of this type would allow for predictable and potentially controllable failure properties at the bulk scale, which could have a variety of applications both in fracture research as well as in industry, where predictable failure can be used to mitigate loss of functionality.

5.6 Summary

To study the influence of complex geometry on the mechanical properties of printed ceramics as well as explore the potential for designed structures as a mechanism to control failure behavior, four different truss systems were printed using DLP of preceramic polymer resin. Two of the truss designs were Kelvin cell arrangements which deform by bending of beams, one design was an octet cell arrangement which deforms by stretching of beams, and one design was a mixture of the two in parallel. The designs were characterized both at the structure level through uniaxial compression and at the beam element level using a previously established strut flexure method. Mechanical analysis of the truss structures after pyroylysis revealed that each of the different designs had different strength, stiffness, and shrinkage, despite attempts to control both their size and stiffness based on uniform linear shrinkage assumptions established from prior studies of printed preceramic polymer. Fractographic analyses of each design indicated that failure occurred as expected given the dominant beam loading regimes. The different structure strengths could reasonably be attributed to different porosities, but the relatively low stiffness and strength of the octet design in comparison to theory indicated that some amount of bending in the structure due to load eccentricity may have occurred. Analysis of the individual beam elements showed a reverse trend from the structures, with the individual elements of the octet beams being about four times stronger than those of the individual Kelvin beams. Much of this difference in strength was attributable to size effects arising from the dramatically reduced surface area the octet beam elements compared to the Kelvin ones. However, the difference in measured strength between the octet structure and its individual beam elements highlights some of the challenges that can arise when relying on the assumption that a structure built from strong individual elements will itself be strong. Furthermore, this study shows that when fabricating complex geometries, careful consideration must be given to the structure-dependent shrinkage behavior of additively manufactured ceramics. The current standards of linear shrinkage and mass loss analysis fail to capture these shrinkage effects. If additive manufacturing of ceramics is to be viable for industrial applications, it is critical to understand these shrinkage behaviors,

which will require investigations well beyond those of simple representative bodies. However, if this degree of shrinkage control can be achieved, there is potential to create truss structures with uniform elastic behavior and failure mechanisms that are controlled solely through designed variations in failure strength.

REFERENCES

[1] Johanna Schmidt and Paolo Colombo. Digital light processing of ceramic components from polysiloxanes. *Journal of the European Ceramic Society*, 38(1):57–66, jan 2018. ISSN 0955-2219. doi: 10.1016/J.JEURCERAMSOC.2017.07.033.

[2] J. W. Obreimoff. The Splitting Strength of Mica. *Proceedings of the Royal Society of London A*, 25:290–297, 1930. ISSN 1364-5021. doi: 10.1098/rspa.1933.0074.

[3] Brian R. Lawn. *Fracture of brittle solids*. Cambridge University Press, 1993. ISBN 9780511623127.

[4] Paolo Colombo, Johanna Schmidt, Giorgia Franchin, Andrea Zocca, and Jens Günster. Additive manufacturing techniques for fabricating complex ceramic components from preceramic polymers. *American Ceramic Society Bulletin*, pages 16–24, 2017.

[5] Zak C Eckel, Chaoyin Zhou, John H Martin, Alan J Jacobsen, William B Carter, and Tobias A Schaedler. Additive manufacturing of polymer-derived ceramics. *Science (New York, N.Y.)*, 351(6268):58–62, jan 2016. ISSN 1095-9203. doi: 10.1126/science.aad2688.

[6] Y. de Hazan and D. Penner. SiC and SiOC ceramic articles produced by stereolithography of acrylate modified polycarbosilane systems. *Journal of the European Ceramic Society*, 37(16):5205–5212, dec 2017. ISSN 0955-2219. doi: 10.1016/J.JEURCERAMSOC.2017.03.021.

[7] Erika Zanchetta, Marco Cattaldo, Giorgia Franchin, Martin Schwentenwein, Johannes Homa, Giovanna Brusatin, and Paolo Colombo. Stereolithography of SiOC Ceramic Microcomponents. *Advanced Materials*, 28(2):370–376, jan 2016. ISSN 09359648. doi: 10.1002/adma.201503470.

[8] T.-A. Pham, D.-P. Kim, T.-W. Lim, S.-H. Park, D.-Y. Yang, and K.-S. Lee. Three-Dimensional SiCN Ceramic Microstructures via Nano-Stereolithography of Inorganic Polymer Photoresists. *Advanced Functional Materials*, 16(9): 1235–1241, jun 2006. ISSN 1616-301X. doi: 10.1002/adfm.200600009. URL http://doi.wiley.com/10.1002/adfm.200600009.

[9] Andrea Zocca, Cynthia M. Gomes, Andreas Staude, Enrico Bernardo, Jens Günster, and Paolo Colombo. SiOC ceramics with ordered porosity by 3D-printing of a preceramic polymer. *Journal of Materials Research*, 28 (17):2243–2252, sep 2013. ISSN 0884-2914. doi: 10.1557/jmr.2013.129. URL https://www.cambridge.org/core/product/identifier/S0884291413001295/type/journal{_}article.

[10] Giorgia Franchin, Larissa Wahl, and Paolo Colombo. Direct ink writing of ceramic matrix composite structures. *Journal of the American Ceramic Society*, 100(10):4397–4401, oct 2017. ISSN 00027820. doi: 10.1111/jace.15045. URL http://doi.wiley.com/10.1111/jace.15045.

[11] Laura Brigo, Johanna Eva Maria Schmidt, Alessandro Gandin, Niccolò Michieli, Paolo Colombo, and Giovanna Brusatin. 3D Nanofabrication of SiOC Ceramic Structures. *Advanced Science*, 5(12):1800937, dec 2018. ISSN 21983844. doi: 10.1002/advs.201800937. URL http://doi.wiley.com/10.1002/advs.201800937.

[12] Xifan Wang, Franziska Schmidt, Dorian Hanaor, Paul H. Kamm, Shuang Li, and Aleksander Gurlo. Additive manufacturing of ceramics from preceramic polymers: A versatile stereolithographic approach assisted by thiol-ene click chemistry. *Additive Manufacturing*, 27:80–90, may 2019. ISSN 2214-8604. doi: 10.1016/J.ADDMA.2019.02.012. URL https://www.sciencedirect.com/science/article/pii/S2214860418310479.

[13] Giorgia Franchin, Halide Maden, Larissa Wahl, Andrea Baliello, Marco Pasetto, Paolo Colombo, Giorgia Franchin, Halide Selin Maden, Larissa Wahl, Andrea Baliello, Marco Pasetto, and Paolo Colombo. Optimization and Characterization of Preceramic Inks for Direct Ink Writing of Ceramic Matrix Composite Structures. *Materials*, 11(4):515, mar 2018. ISSN 1996-1944. doi: 10.3390/ma11040515. URL http://www.mdpi.com/1996-1944/11/4/515.

[14] Andrea Zocca, Giorgia Franchin, Hamada Elsayed, Emilia Gioffredi, Enrico Bernardo, and Paolo Colombo. Direct Ink Writing of a Preceramic Polymer and Fillers to Produce Hardystonite ($Ca_2ZnSi_2O_7$) Bioceramic Scaffolds. *Journal of the American Ceramic Society*, 99(6):1960–1967, jun 2016. ISSN 00027820. doi: 10.1111/jace.14213. URL http://doi.wiley.com/10.1111/jace.14213.

[15] Giovanni Pierin, Chiara Grotta, Paolo Colombo, and Cecilia Mattevi. Direct Ink Writing of micrometric SiOC ceramic structures using a preceramic polymer. *Journal of the European Ceramic Society*, 36(7):1589–1594, jun 2016. ISSN 0955-2219. doi: 10.1016/J.JEURCERAMSOC.2016.01.047. URL https://www.sciencedirect.com/science/article/abs/pii/S0955221916300474.

[16] A Zocca, H Elsayed, E Bernardo, C M Gomes, M A Lopez-Heredia, C Knabe, P Colombo, and J Günster. 3D-printed silicate porous bioceramics using a non-sacrificial preceramic polymer binder. *Biofabrication*, 7(2):025008, may 2015. ISSN 1758-5090. doi: 10.1088/1758-5090/7/2/025008. URL http://stacks.iop.org/1758-5090/7/i=2/a=025008?key=crossref.ad6c583046cb0f2af81ab1c2c8b34a48.

[17] Tiemo Bückmann, Nicolas Stenger, Muamer Kadic, Johannes Kaschke, Andreas Frölich, Tobias Kennerknecht, Christoph Eberl, Michael Thiel, and Martin Wegener. Tailored 3D mechanical metamaterials made by dip-in direct-laser-writing optical lithography. *Advanced Materials*, 24(20):2710–2714, 2012. ISSN 09359648. doi: 10.1002/adma.201200584.

[18] Julian Panetta, Qingnan Zhou, Luigi Malomo, Nico Pietroni, Paolo Cignoni, and Denis Zorin. Elastic textures for additive fabrication. *ACM Transactions on Graphics*, 34(4):1–12, jul 2015. ISSN 07300301. doi: 10.1145/2766937. URL http://dl.acm.org/citation.cfm?doid=2809654.2766937.

[19] Caroline A Schneider, Wayne S Rasband, and Kevin W Eliceiri. NIH Image to ImageJ: 25 years of image analysis. *Nature Methods*, 9(7):671–675, jul 2012. ISSN 1548-7091. doi: 10.1038/nmeth.2089. URL http://www.nature.com/articles/nmeth.2089.

[20] Rasto Brezny, David J. Green, and Chuong Quang Dam. Evaluation of Strut Strength in Open-Cell Ceramics. *Journal of the American Ceramic Society*, 72(6):885–889, jun 1989. ISSN 0002-7820. doi: 10.1111/j.1151-2916.1989.tb06239.x.

[21] ASTM C1684 - 18, Standard Test Method for Flexural Strength of Advanced Ceramics at Ambient Temperature Cylindrical Rod Strength, 2018.

[22] G. M. Pharr. An improved technique for determining hardness and elastic modulus using load and displacement sensing indentation experiments. *Journal of Materials Research*, 7(6):1564–1583, 1992. ISSN 20445326. doi: 10.1557/JMR.1992.1564.

[23] H.X. Zhu, J.F. Knott, and N.J. Mills. Analysis of the elastic properties of open-cell foams with tetrakaidecahedral cells. *Journal of the Mechanics and Physics of Solids*, 45(3):319–343, mar 1997. ISSN 0022-5096. doi: 10.1016/S0022-5096(96)00090-7.

[24] V.S. Deshpande, N.A. Fleck, and M.F. Ashby. Effective properties of the octet-truss lattice material. *Journal of the Mechanics and Physics of Solids*, 49 (8):1747–1769, aug 2001. ISSN 0022-5096.

[25] Lorna J Gibson and Michael F Ashby. *Cellular Solids: Structure and Properties - Lorna J. Gibson, Michael F. Ashby - Google Books*. Cambridge University Press, 2 edition, 1997. ISBN 0 521 49911 9.

[26] Paolo Colombo, John R. Hellmann, and David L. Shelleman. Thermal Shock Behavior of Silicon Oxycarbide Foams. *Journal of the American Ceramic Society*, 85(9):2306–2312, sep 2002. ISSN 0002-7820. doi: 10.1111/j.1151-2916.2002.tb00452.x.

[27] Cekdar Vakifahmetoglu, Paolo Colombo, Alberto Pauletti, Cristina Fernandez Martin, and Florence Babonneau. SiOC Ceramic Monoliths with Hierarchical Porosity. *International Journal of Applied Ceramic Technology*, 7(4):528–535, mar 2009. ISSN 1546542X. doi: 10.1111/j.1744-7402.2009.02365.x. URL http://doi.wiley.com/10.1111/j.1744-7402.2009.02365.x.

[28] Noriaki Arai and Katherine T. Faber. Hierarchical porous ceramics via two-stage freeze casting of preceramic polymers. *Scripta Materialia*, 162:72–76, mar 2019. ISSN 1359-6462. doi: 10.1016/J.SCRIPTAMAT.2018.10.037. URL https://www.sciencedirect.com/science/article/pii/S1359646218306663.

[29] J. B. Wachtman, W. Roger. Cannon, and M. John. Matthewson. *Mechanical properties of ceramics*. Wiley, 2009. ISBN 9780470451502. URL https://www.wiley.com/en-us/Mechanical+Properties+of+Ceramics{\%}2C+2nd+Edition-p-9780470451502.

[30] Carlos M. Portela, Julia R. Greer, and Dennis M. Kochmann. Impact of node geometry on the effective stiffness of non-slender three-dimensional truss lattice architectures. *Extreme Mechanics Letters*, 22:138–148, jul 2018. ISSN 2352-4316. doi: 10.1016/J.EML.2018.06.004. URL https://www.sciencedirect.com/science/article/pii/S2352431618300725.

[31] N. A. Fleck, V. S. Deshpande, and M. F. Ashby. Micro-architectured materials: past, present and future. *Proceedings of the Royal Society A: Mathematical, Physical and Engineering Sciences*, 466(2121):2495–2516, sep 2010. ISSN 1364-5021. doi: 10.1098/rspa.2010.0215. URL http://www.royalsocietypublishing.org/doi/10.1098/rspa.2010.0215.

[32] Johan Christensen, Muamer Kadic, Oliver Kraft, and Martin Wegener. Vibrant times for mechanical metamaterials. *MRS Communications*, 5(03):453–462, sep 2015. ISSN 2159-6859. doi: 10.1557/mrc.2015.51. URL http://www.journals.cambridge.org/abstract{_}S2159685915000518.

[33] T A Schaedler, A J Jacobsen, A Torrents, A E Sorensen, J Lian, J R Greer, L Valdevit, and W B Carter. Ultralight metallic microlattices. *Science (New York, N.Y.)*, 334(6058):962–965, nov 2011. ISSN 1095-9203. doi: 10.1126/science.1211649. URL http://www.ncbi.nlm.nih.gov/pubmed/22096194.

[34] Lucas R. Meza, Satyajit Das, and Julia R. Greer. Strong, lightweight, and recoverable three-dimensional ceramic nanolattices. *Science*, 345(6202):1322–1326, sep 2014. ISSN 0036-8075. doi: 10.1126/SCIENCE.1255908. URL http://science.sciencemag.org/content/345/6202/1322.

Chapter 6

CONCLUSIONS AND FUTURE WORK

6.1 Conclusions

The objective of this work was to gain a better understanding of how the design freedom afforded by precise net shape processing techniques such as additive manufacturing might be better utilized to achieve brittle composites with higher toughness. This focus centered how designed structures can affect fracture behavior, what kind of material contrast is needed to achieve higher toughness, and how anisotropic structures might be used to improve toughness beyond what is possible with conventional processing techniques. This increase in toughness would be of particular benefit in the context of ceramics systems, which show promise in structural and engine applications due to their thermal and chemical resilience, but are limited by their brittle failure behavior.

Firstly, we used stable crack growth experiments to understand the influence of designed anisotropy on crack propagation behavior. In particular we explored parameterized composite structures under surfing load conditions with full-field displacement measurement techniques. This analysis showed, in particular, the potential of elastic contrast as a tool for pinning cracks and how a balance between inclusion spacing and inclusion size can maximize the toughness to be well above that of the homogeneous case. Directional toughness showed particular potential for cases of biased or loading because toughness values could be achieved that were similar to those of isotropic materials, but at significantly lower inclusion volume fractions. This improved toughness using smaller volume fractions makes anisotropic inclusions favorable for directional toughness with better retention of bulk matrix properties, which is desirable in structural ceramics.

The effect of anisotropy on both nucleation and propagation was explored through asymmetric void structures called “fracture diodes". These structures used designs of triangular voids to produce a favorable propagation direction, and nucleation was controlled though the presence of an edge notch in the unidirectional cases and larger void at the center of the specimen in the bidirectional case. With this added understanding, a “true diode" design was developed that used rounded triangles and carefully controlled void spacing to further enhance toughness asymmetry, resulting

in controlled directional failure 100% of the time. This demonstrates that with a careful control of both compliance and anisotropy, brittle fracture can be controlled in the context of both nucleation as well as propagation of a macrocrack.

After exploring both nucleation and propagation in brittle polymers, the focus transitioned to toughening through designed anisotropy in ceramics. This was achieved using wedge splitting of muscovite mica, which allows for globally stable crack growth. Building on the work of Obreimoff, the behavior of heterogeneous mica sheets with designed, step-wise thickness heterogeneities was investigated. In mica prepared with thickness heterogeneities, a dramatic increase in required separation force occurred when the mica splitting front encountered the thickness increase in the mica sheet. This force enhancement is associated with a change in flexural rigidity of the cleaved mica sheet, which is nonlinear, and the increase in force observed is significantly larger than the splitting force required for the homogeneous constituents. This nonlinearity implies that not only do changes in compliance have an impact on achievable toughness, but variations in the magnitude of compliance change can lead to anisotropy in fracture directions. This anisotropy could be beneficial for maximizing toughness increase and minimizing unstable crack growth due to rapid propagation. This phenomenon could prove to be of significant benefit in layered ceramic composites, as it demonstrates that the introduction of additional stiff layers within compliant regions might further increase effective toughness.

The exploration of ceramics was then extended to systems produced printed preceramic polymer. The investigation explored not only the potential for designed structures as a mechanism to control failure behavior, but also the influence of complex geometry on the mechanical properties of printed ceramics. Four different truss design (two Kelvin cell designs, one octet design, and one mixed design) were characterized both at the structure level through uniaxial compression and at the beam element level using a previously established beam flexure method. Despite attempts to control both size and stiffness based on prior studies of printed preceramic polymer, mechanical analysis of the truss structures after pyrolysis revealed that each of the designs had different strength, stiffness, and shrinkage. Analysis of bulk structures showed a relatively linear scaling between strength and porosity, whereas of the individual beam elements showed a reverse trend from the structures, with the most slender octet beams being the strongest despite the octet structure being weakest. Much of this difference in strength was attributable to size effects arising from the dramatically reduced surface area of the octet beam elements compared

to the Kelvin ones. This study shows that when fabricating complex geometries, careful consideration must be given to the structure-dependent shrinkage behavior of additively manufactured ceramics, and the current standards of linear shrinkage and mass loss analysis fail to capture these shrinkage effects. If additive manufacturing of ceramics is to be viable for industrial applications, it is critical to understand these shrinkage behaviors, which will require investigations well beyond those of simple representative bodies. However, if the degree of shrinkage can be managed, there is potential to create truss structures with uniform elastic behavior and controlled failure mechanisms, where crack nucleation and propagation would be dictated by the location of low strength truss elements within the system.

Finally, this work demonstrates how improved processing control not only changes the available design space for composite toughening mechanisms, but it also explores how this new design space can be used to achieve toughening behaviors that have not been well explored. Directional toughening, which is achievable through anisotropy, can produce comparable effective toughness values to isotropic inclusions in one direction, but at a significantly lower volume fraction of inclusion phase, which is beneficial for preserving desirable matrix properties. Furthermore, this directionality can be used to constrain and control crack growth, even before the crack has nucleated. This opens the potential for structures that can be designed to provide toughening based on a particular known crack location, which is dictated by inclusion design and arrangement. Although ceramic additive manufacturing of ceramics is at present limited in terms of bulk structures that can be readily produced, the same anisotropic toughening principles can be applied to truss systems as well. Instead of different materials, different truss elements can be used to control the potential crack nucleation and propagation directions, which opens up further possibilities for increased material toughness.

6.2 Future Work

This exploratory nature of this work means there are a multitude of potential avenues for future work extending off the approaches used in this investigation. The potential areas of research that can emerge from this work will be addressed based on the order of the studies presented.

Propagation Studies Using Surfing Load

Although the surfing load experiments could not be readily extended to explore ceramic systems due the significant stiffness increase, there is still significant potential

for the surfing load in the context of exploration of possible two-dimensional toughening designs. The stable crack growth that can be achieved both numerically as well as experimentally means that inclusion arrangements can be readily explored in simulation and then validated in experiment, although the materials suitable for testing would be limited to brittle polymers with lower stiffness than ceramics. This has particular promise because the thin specimens tested in surfing load keep specimen failure constrained to two dimensions, which removes some of the more challenging, hard-to-model aspects of three-dimensional fracture from a numerical standpoint, such as out-of-plane crack twisting and crack bowing. Still, within this two dimensional space, there is significant possibility for the exploration of inclusion arrangements to maximize toughness in a singular direction while minimizing inclusion volume fraction, or to maximize toughness anisotropy, that is, the difference in toughness between different propagation directions. Furthermore, any potential designs could readily be tested experimentally to verify their performance in physical material systems. Some of the experimental limitations with the current surfing load setup would have to be addressed, such as the unwanted buildup of load due to crack pinning. However, it may be possible to address some of this through a redesign of the rail. For example, changing the rail from aluminum to brass to minimize friction and galling and also changing the pin and bushing fittings to have tighter tolerances may make the load buildup more reliable and consistent. With these improvements, it may be possible to refine the diverging section of the rail to be less abrupt, which may help prevent an excess buildup of tension when the crack is pinned at inclusion/matrix interfaces. A refined rail design would also allow for the exploration of additional polymer systems, such as acrylic polymers that can be laser cut. Coupling these with acrylate photopolymers and photosensitive slurries would allow for the testing of multi-material composite designs under surfing load conditions, which would remove the issue associated with crack pinning due to geometric effects, where the crack is forced to bow outward to account for the changes in thickness in the printed specimens in surfing load studies.

Nucleation and Propagation Studies with Fracture Diodes

Experiments with fracture diodes showed the potential of asymmetrical voids to control both the nucleation and subsequent propagation direction of cracks under unbiased loads. However, the exploration of this degree of control was relatively limited both in the context of possible inclusion designs and orientations as well as possible materials of interest. In the context of inclusion designs, all designs in this

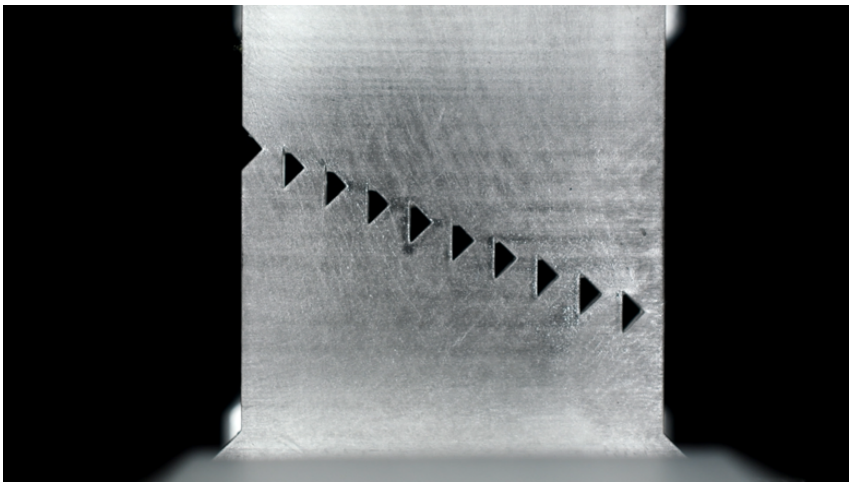

Figure 6.1: Example of fracture diode specimen with inclusion position along an axis not orthogonal to the load axis.

study were constrained to a single axis, and that axis was chosen to be orthogonal to the loading axis. However, there is significant potential to explore axes that are not orthogonal to the load axis as a means to introduce mixed mode failure behavior into the system as shown in Figure 6.1. This type of mixed mode failure may have some potential in the context of exploring how different arrangements of porosity can affect failure behavior as well as how crack deflection can be used as a tool to prevent macroscopic failure. Some basic experiments with slanted diodes were performed by C.M. Long, but the extent of designs explored was relatively limited, and additional criteria need to be established in the context of what behaviors are favorable, which would require additional numerical simulations.

Additionally, given that fracture diodes are able to provide such a high degree of failure control, it is logical to explore how this failure control might be exploited to achieve higher toughness behavior. The approach here would be of particular interest because it would deviate slightly from the ideologies of traditional composite toughening. Instead of creating a uniform micro- and macrostructure to prevent macrocrack growth wherever it may occur, the idea would be to instead create locations where macrocracks are more likely to form, and then construct toughening mechanisms specifically around each of these potential locations. In this sense, the fracture diodes could be used to create predictable crack propagation over a short distance, which could then be arrested by much more elaborate toughening mechanisms than can be produced in traditional composites. In this sense, the formation of these macrocracks can be used to relieve stress on other parts of the

system, where these more complex toughening mechanisms are not present. This approach is particularly favorable from a numerical standpoint because it is far easier to explore possible toughening mechanisms numerically when the exact location of the macroscopic crack is already known, but these can be difficult to implement practically because the trajectory of the crack is not known. This type of toughening around a known crack location has even been explored relatively recently in the context of machine learning.[1] In these scenarios, the trajectory control afforded by diodes may prove useful by making fracture more predictable.

Finally, fracture diode behavior can also be explored in the context of different material systems. Theoretically, this degree of fracture control should also be achievable in stiffer systems like printed ceramics, but this has never been explored in any meaningful detail. In the case of ceramics, higher stiffness will likely result in a larger buildup of elastic energy for a given displacement, so failure may occur more rapidly and catastrophically, which will demand more faster image capture techniques, but the directionality associated with the failure should still be present. If this degree of control could also be achieved in ceramics, there is potential for more complex structures to provide crack arrest and further enhance ceramic toughness, which is a desirable property in many technical ceramics.

Wedge Splitting of Heterogeneous Mica

Compared to the surfing load and fracture diode experiments, the possibilities for further exploring heterogeneous toughening through mica splitting are somewhat limited. The most promising avenues for additional exploration involve either larger sections of uniform mica material or the introduction additional phases. If larger pieces of mica could be obtained, the nonlinearity in the toughening increase due compliance contrast could be explored in greater detail, and structures containing both thickness increases and subsequent thickness decreases could be explored to both maximize the load buildup due to the crack arrest at increases in thickness and minimize the load drop that occurs at decreases in thickness. Along these same lines, the introduction of additional phases to change stiffness contrast becomes much easier when mica sheets are larger in size.

Ceramics from Printed Preceramic Polymers

Although the experiments in this work were somewhat limited due to previously undocumented structurally dependent shrinkage behavior, the potential for additional toughening mechanisms through 3D printed ceramics is still rather large. In the

context of truss systems, if shrinkage can be properly accounted for, the potential to use different truss structures with equivalent stiffnesses but different mechanisms (bending vs. stretching), and therefore different failure strengths, presents promise as a way to control the nucleation of cracks in more complex structures. Structurally dependent shrinkage is expected to be present in most ceramic printing techniques that involve a diffusion-mediated conversion process, and controlling this will take some effort, but it is likely achievable with enough data on shrinkage behavior for different print systems. All that would be required to get these data would be a change in shrinkage reporting methodologies in the ceramic additive manufacturing community.

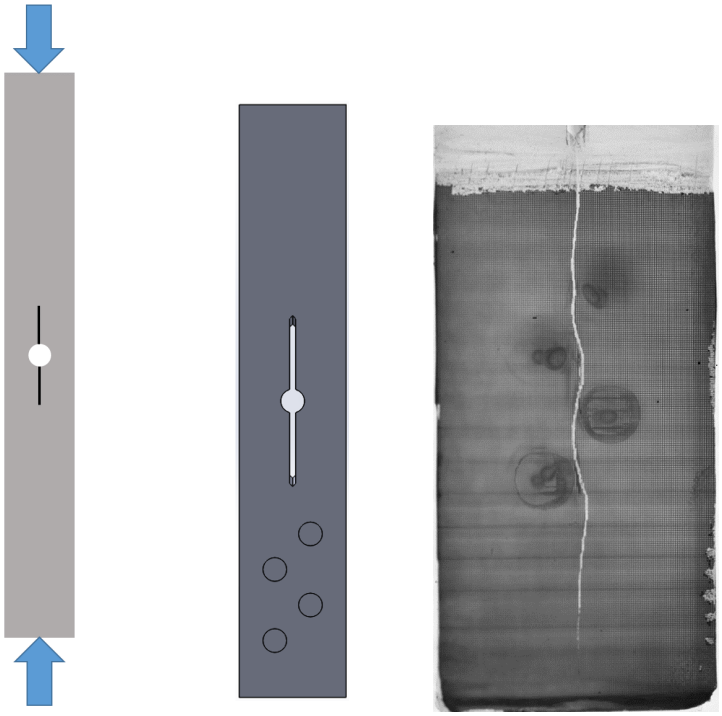

(a) DCDC schematic (b) DCDC design with inclusions (c) Crack-inclusion interaction

Figure 6.2: Images showing a schematic of the DCDC test (a), a DCDC design containing inclusions (b), and the crack-inclusion interactions in a test of a printed photopolymer DCDC specimen (c).

Going beyond truss structures, however, there is also potential for testing of solid ceramic structures if the test chosen such that stable crack growth can be achieved and specimen volume does not have to be large. One promising test is double cleavage drilled compression (DCDC), which involves the compression of slender ceramic or glass specimens with a hole in the center of the specimen, such that the crack

nucleates at this hole and grows parallel to the axis of compression, as shown in Figure 6.2a.[2, 3] This test provides stable crack growth on specimens that are relative small in both width and thickness, so it may prove to be a suitable means of evaluating the effect of anisotropic inclusions on ceramic structures. C.M. Long has already done some preliminary tests to explore the potential of DCDC in printed polymer systems, as shown in Figure 6.2b and 6.2c, and crack behavior similar to the response seen in surfing load was seen in DCDC systems, though characterization of toughness proved challenging due to large compressive deformations before fracture. To explore the potential of DCDC for characterizing ceramic composites, SiOC ceramics developed and printed at HRL laboratories are being evaluated in DCDC, and crack length and load are being used to calculate toughness in systems during fracture. It is proposed that the introduction of additional soft inclusions into these SiOC systems, through either changes in thickness or a second phase, would create crack deflection and pinning due to elastic contrast, which should improve macroscopic toughness.

REFERENCES

[1] Grace X. Gu, Chun Teh Chen, and Markus J. Buehler. De novo composite design based on machine learning algorithm. *Extreme Mechanics Letters*, 2018. ISSN 23524316. doi: 10.1016/j.eml.2017.10.001.

[2] C. Janssen. Specimen for fracture mechanics studies on glass. *Proceedings of the 10th International Congress On Glass*, pages 10.23–10.30, 1974.

[3] M. Y. He, M. R. Turner, and A. G. Evans. Analysis of the double cleavage drilled compression specimen for interface fracture energy measurements over a range of mode mixities. *Acta Metallurgica Et Materialia*, 43(9):3453–3458, 1995. ISSN 09567151. doi: 10.1016/0956-7151(95)00036-U.

BIBLIOGRAPHY

[1] N. R. Brodnik, C. J. Hsueh, and M. T. Johnson. A nonconstraining templated powder grid for measurement of strain. *Strain*, 2018. ISSN 14751305. doi: 10.1111/str.12273.

[2] M.T. Johnson, N.R. Brodnik, T. Ekeh, K. Bhattacharya, and K.T. Faber. Obreimoff revisited: Controlled heterogeneous fracture through the splitting of mica. *Mechanics of Materials*, 136:103088, sep 2019. ISSN 0167-6636. doi: 10.1016/J.MECHMAT.2019.103088. URL https://www.sciencedirect.com/science/article/pii/S0167663618307543?dgcid=author.

[3] N. R. Brodnik, S. Brach, K. Bhattacharya, B. Bourdin, K.T. Faber, and G. Ravichandran. Fracture diodes: Directional asymmetry of fracture toughness. *In Preparation*, 2019.

[4] N. R. Brodnik, J. Schmidt, P. Colombo, and K.T. Faber. Analysis of multi-scale mechanical properties of ceramic trusses prepared from preceramic polymers. *Submitted to Additive Manufacturing*, 2019.

[5] N. R. Brodnik, C.-J. Hsueh, K. Bhattacharya, B. Bourdin, K.T. Faber, and G. Ravichandran. Guiding and trapping cracks with compliant inclusions for enhancing toughness of brittle composite materials. *Submitted to Journal of Applied Mechanics*, 2019.

[6] United States Energy Information Administration. Annual Energy Outlook 2019 with projections to 2050. Technical report, 2019. URL www.eia.gov/aeo.

[7] Koch Gerhardus, Jeff Varney, Neil Thompson, Dnv Gl, Oliver Moghissi, Melissa Gould, and Joe Payer. NACE Impact Report: International Measures of Prevention Application, and Economics of Corrosion Technologies Study. Technical report, 2016.

[8] A. A. Griffith. The Phenomena of Rupture and Flow in Solids. *Philosophical Transactions of the Royal Society A: Mathematical, Physical and Engineering Sciences*, 221(582-593):163–198, jan 1921. ISSN 1364-503X. doi: 10.1098/rsta.1921.0006. URL http://rsta.royalsocietypublishing.org/cgi/doi/10.1098/rsta.1921.0006.

[9] C.E. Inglis. Stresses in a plate due to the presence of cracks and sharp corners. *Trans Inst Naval Archit*, 55:219–241, 1913.

[10] Brian R. Lawn. *Fracture of brittle solids*. Cambridge University Press, 1993. ISBN 9780511623127.

[11] R. W. Hertzberg, R. P. Vinci, and J. L. Hertzberg. Dynamic Embrittlement. *Deformation and Fracture Mechanics of Engineering Materials*, 2012.

[12] G.R. Irwin. Fracture. *Handbuch der Physik*, 6:551, 1958.

[13] P.C. Paris and G.C. Sih. Stress Analysis of Cracks. In *Fracture Toughness Testing and its Applications*. 1965. doi: 10.1520/stp26584s.

[14] D. S. Dugdale. Yielding of steel sheets containing slits. *Journal of the Mechanics and Physics of Solids*, 1960. ISSN 00225096. doi: 10.1016/0022-5096(60)90013-2.

[15] G. I. Barenblatt. The Mathematical Theory of Equilibrium Cracks in Brittle Fracture. *Advances in Applied Mechanics*, 1962. ISSN 00652156. doi: 10.1016/S0065-2156(08)70121-2.

[16] James R Rice. Mathematical Analysis in the Mechanics of Fracture. Technical report, 1968. URL `http://esag.harvard.edu/rice/018{\_}Rice{\_}MathAnalMechFract{\_}68.pdf`.

[17] Peter L. Swanson, Carolyn J. Fairbanks, Brian R. Lawn, Yiu-Wing -W Mai, and Bernard J. Hockey. Crack-Interface Grain Bridging as a Fracture Resistance I, Mechanism in Ceramics: I, Experimental Study on Alumina. *Journal of the American Ceramic Society*, 1987. ISSN 15512916. doi: 10.1111/j.1151-2916.1987.tb04982.x.

[18] J Cook and J E Gordon. A mechanism for the control of crack propagation in all-brittle systems. *Proceedings of the Royal Society of London. Series A. Mathematical and Physical Sciences*, 1964. ISSN 2053-9169. doi: 10.1098/rspa.1964.0248.

[19] K.T. Faber and A.G. Evans. Crack deflection processes—I. Theory. *Acta Metallurgica*, 31(4):565–576, apr 1983. ISSN 0001-6160. doi: 10.1016/0001-6160(83)90046-9. URL `https://www.sciencedirect.com/science/article/pii/0001616083900469`.

[20] R. W. Davidge and T. J. Green. The strength of two-phase ceramic/glass materials. *Journal of Materials Science*, 1968. ISSN 00222461. doi: 10.1007/BF00757910.

[21] A. G. Evans and K. T. Faber. Crack-Growth Resistance of Microcracking Brittle Materials. *Journal of the American Ceramic Society*, 1984. ISSN 15512916. doi: 10.1111/j.1151-2916.1984.tb18842.x.

[22] R. C. Garvie, R. H. Hannink, and R. T. Pascoe. Ceramic steel? *Nature*, 1975. ISSN 00280836. doi: 10.1038/258703a0.

[23] D. B. Marshall, B. N. Cox, and A. G. Evans. The mechanics of matrix cracking in brittle-matrix fiber composites. *Acta Metallurgica*, 1985. ISSN 00016160. doi: 10.1016/0001-6160(85)90124-5.

[24] Giorgia Franchin, Larissa Wahl, and Paolo Colombo. Direct ink writing of ceramic matrix composite structures. *Journal of the American Ceramic Society*, 100(10):4397–4401, oct 2017. ISSN 00027820. doi: 10.1111/jace.15045. URL http://doi.wiley.com/10.1111/jace.15045.

[25] Jennifer A. Lewis. Direct ink writing of 3D functional materials. *Advanced Functional Materials*, 2006. ISSN 1616301X. doi: 10.1002/adfm.200600434.

[26] Mukesh Agarwala, David Bourell, Joseph Beaman, Harris Marcus, and Joel Barlow. Direct selective laser sintering of metals. *Rapid Prototyping Journal*, 1995. ISSN 13552546. doi: 10.1108/13552549510078113.

[27] T. Vilaro, C. Colin, J. D. Bartout, L. Nazé, and M. Sennour. Microstructural and mechanical approaches of the selective laser melting process applied to a nickel-base superalloy. *Materials Science and Engineering A*, 2012. ISSN 09215093. doi: 10.1016/j.msea.2011.11.092.

[28] Paul F. Jacobs. *Rapid prototyping & manufacturing : fundamentals of stereolithography*. Society of Manufacturing Engineers in cooperation with the Computer and Automated Systems Association of SME, 1 edition, 1992. ISBN 9780872634251.

[29] Erika Zanchetta, Marco Cattaldo, Giorgia Franchin, Martin Schwentenwein, Johannes Homa, Giovanna Brusatin, and Paolo Colombo. Stereolithography of SiOC Ceramic Microcomponents. *Advanced Materials*, 28(2):370–376, jan 2016. ISSN 09359648. doi: 10.1002/adma.201503470. URL http://doi.wiley.com/10.1002/adma.201503470.

[30] Zak C Eckel, Chaoyin Zhou, John H Martin, Alan J Jacobsen, William B Carter, and Tobias A Schaedler. Additive manufacturing of polymer-derived ceramics. *Science (New York, N.Y.)*, 351(6268):58–62, jan 2016. ISSN 1095-9203. doi: 10.1126/science.aad2688. URL http://www.ncbi.nlm.nih.gov/pubmed/26721993.

[31] Johanna Schmidt and Paolo Colombo. Digital light processing of ceramic components from polysiloxanes. *Journal of the European Ceramic Society*, 38(1):57–66, jan 2018. ISSN 0955-2219. doi: 10.1016/J.JEURCERAMSOC.2017.07.033. URL https://www.sciencedirect.com/science/article/abs/pii/S0955221917305186.

[32] Martin Schwentenwein and Johannes Homa. Additive manufacturing of dense alumina ceramics. *International Journal of Applied Ceramic Technology*, 2015. ISSN 17447402. doi: 10.1111/ijac.12319.

[33] Vladislava Tomeckova and John W. Halloran. Critical energy for photopolymerization of ceramic suspensions in acrylate monomers. *Journal of the European Ceramic Society*, 30(16):3273–3282, 2010. ISSN 09552219. doi: 10.1016/j.jeurceramsoc.2010.08.003. URL http://dx.doi.org/10.1016/j.jeurceramsoc.2010.01.027.

[34] Vladislava Tomeckova and John W. Halloran. Cure depth for photopolymerization of ceramic suspensions. *Journal of the European Ceramic Society*, 30(15): 3023–3033, 2010. ISSN 09552219. doi: 10.1016/j.jeurceramsoc.2010.06.004. URL http://dx.doi.org/10.1016/j.jeurceramsoc.2010.06.004.

[35] V. Tomeckova and J. W. Halloran. Macroporous polyacrylates from terpene-acrylate thermoreversible photopolymerizable vehicle. *Journal of Materials Science*, 47(16):6166–6178, 2012. ISSN 00222461. doi: 10.1007/s10853-012-6537-5.

[36] Vladislava Tomeckova and John W. Halloran. Porous ceramics by photopolymerization with terpene-acrylate vehicles. *Journal of the American Ceramic Society*, 95(12):3763–3768, 2012. ISSN 00027820. doi: 10.1111/j.1551-2916.2012.05444.x.

[37] Vladislava Tomeckova, Steven J. Norton, Brian J. Love, and John W. Halloran. Photopolymerization of acrylate suspensions with visible dyes. *Journal of the European Ceramic Society*, 33(4):699–707, 2013. ISSN 09552219. doi: 10.1016/j.jeurceramsoc.2012.10.015. URL http://dx.doi.org/10.1016/j.jphotochem.2012.08.008.

[38] Lucas R. Meza, Satyajit Das, and Julia R. Greer. Strong, lightweight, and recoverable three-dimensional ceramic nanolattices. *Science*, 345(6202): 1322–1326, sep 2014. ISSN 0036-8075. doi: 10.1126/SCIENCE.1255908. URL http://science.sciencemag.org/content/345/6202/1322.

[39] Grace X. Gu, Chun Teh Chen, and Markus J. Buehler. De novo composite design based on machine learning algorithm. *Extreme Mechanics Letters*, 2018. ISSN 23524316. doi: 10.1016/j.eml.2017.10.001.

[40] G.A. Francfort and J.-J. Marigo. Revisiting brittle fracture as an energy minimization problem. *Journal of the Mechanics and Physics of Solids*, 46 (8):1319–1342, aug 1998. ISSN 0022-5096. doi: 10.1016/S0022-5096(98)00034-9. URL https://www.sciencedirect.com/science/article/pii/S0022509698000349.

[41] B. Bourdin, G.A. Francfort, and J-J. Marigo. Numerical experiments in revisited brittle fracture. *Journal of the Mechanics and Physics of Solids*, 48(4):797–826, apr 2000. ISSN 0022-5096. doi: 10.1016/S0022-5096(99)00028-9. URL https://www.sciencedirect.com/science/article/pii/S0022509699000289.

[42] Blaise Bourdin, Gilles A. Francfort, and Jean-Jacques Marigo. The Variational Approach to Fracture. *Journal of Elasticity*, 91(1-3):5–148, apr 2008. ISSN 0374-3535. doi: 10.1007/s10659-007-9107-3. URL http://link.springer.com/10.1007/s10659-007-9107-3.

[43] M. Z. Hossain, C. J. Hsueh, B. Bourdin, and K. Bhattacharya. Effective toughness of heterogeneous media. *Journal of the Mechanics and Physics of Solids*, 71(1):15–32, 2014. ISSN 00225096. doi: 10.1016/j.jmps.2014.06.002. URL http://dx.doi.org/10.1016/j.jmps.2014.06.002.

[44] C.-J. Hsueh. Effective toughness of heterogeneous materials. *PhD Thesis, California Institute of Technology*, 2017.

[45] E Tanné, T Li, B Bourdin, J J Marigo, and C Maurini. Crack nucleation in variational phase-field models of brittle fracture. *J Mech Phys Solids*, 110: 80–99, 2018.

[46] Neng Wang and Shuman Xia. Cohesive fracture of elastically heterogeneous materials: An integrative modeling and experimental study. *Journal of the Mechanics and Physics of Solids*, 98:87–105, jan 2017. ISSN 0022-5096. doi: 10.1016/J.JMPS.2016.09.004. URL https://www.sciencedirect.com/science/article/pii/S0022509616303313.

[47] C-J. Hsueh, L. Avellar, B. Bourdin, G. Ravichandran, and K. Bhattacharya. Stress fluctuation, crack renucleation and toughening in layered materials. *Journal of the Mechanics and Physics of Solids*, 120:68–78, nov 2018. ISSN 0022-5096. doi: 10.1016/J.JMPS.2018.04.011. URL https://www.sciencedirect.com/science/article/pii/S0022509617311407.

[48] M Y He and J W Hutchinson. Crack Deflection at an Interface Between Dissimilar Elastic-Materials. *Int J Solids Struct*, 25(9):1053–1067, 1989.

[49] AutoDesk. Autodesk Standard Clear PR48 Formulation. https://cdn-standard3.discourse.org/uploads/autodesk/original/1X/1b755fa09bb75aae7395f2ffccd444c68b06f3ba.pdf, 2017. [Online; accessed 10-June-2017].

[50] Owen Smithyman. Ember Standard Clear - Mechanical Properties. http://forum.ember.autodesk.com/t/ember-standard-clear-mechanical-properties/71/2, 2016. [Online; accessed 10-June-2017].

[51] H. Moulinec and P. Suquet. A fft-based numerical method for computing the mechanical properties of composites from images of their microstructures. In *IUTAM Symposium on Microstructure-Property Interactions in Composite Materials*, pages 235–246. Springer, 1995.

[52] H. Moulinec and P. Suquet. A numerical method for computing the overall response of nonlinear composites with complex microstructure. *Computer methods in applied mechanics and engineering*, 157(1-2):69–94, 1998.

[53] J.C. Michel, H. Moulinec, and P. Suquet. A computational scheme for linear and non-linear composites with arbitrary phase contrast. *International Journal for Numerical Methods in Engineering*, 52(1-2):139–160, 2001.

[54] Michel Grédiac. The use of full-field measurement methods in composite material characterization: interest and limitations. *Composites Part A: Applied Science and Manufacturing*, 35(7-8):751–761, jul 2004. ISSN 1359835X. doi: 10.1016/j.compositesa.2004.01.019. URL http://linkinghub.elsevier.com/retrieve/pii/S1359835X04000260.

[55] Frank C Demarest. High-resolution, high-speed, low data age uncertainty, heterodyne displacement measuring interferometer electronics. *Measurement Science and Technology*, 9(7):1024–1030, jul 1998. ISSN 0957-0233. doi: 10.1088/0957-0233/9/7/003. URL http://stacks.iop.org/0957-0233/9/i=7/a=003?key=crossref.7a9b270bed78db7ab79a4909ced2fcec.

[56] Hareesh V. Tippur, Sridhar Krishnaswamy, and Ares J. Rosakis. Optical mapping of crack tip deformations using the methods of transmission and reflection coherent gradient sensing: a study of crack tip K-dominance. *International Journal of Fracture*, 52(2):91–117, 1991. ISSN 0376-9429. doi: 10.1007/bf00032372. URL https://link.springer.com/article/10.1007{\%}2FBF00032372?LI=true.

[57] Vasco Ronchi. Forty Years of History of a Grating Interferometer. *Applied Optics*, 3(4):437, apr 1964. ISSN 0003-6935. doi: 10.1364/AO.3.000437. URL https://www.osapublishing.org/abstract.cfm?URI=ao-3-4-437.

[58] H. Lee and S. Krishnaswamy. A compact polariscope/shearing interferometer for mapping stress fields in bimaterial systems. *Experimental Mechanics*, 36 (4):404–411, dec 1996. ISSN 0014-4851. doi: 10.1007/BF02328585. URL http://link.springer.com/10.1007/BF02328585.

[59] T. C. Chu, W. F. Ranson, and M. A. Sutton. Applications of digital-image-correlation techniques to experimental mechanics. *Experimental Mechanics*, 25(3):232–244, sep 1985. ISSN 0014-4851. doi: 10.1007/BF02325092. URL http://link.springer.com/10.1007/BF02325092.

[60] H. A. Bruck, S. R. McNeill, M. A. Sutton, and W. H. Peters. Digital image correlation using Newton-Raphson method of partial differential correction. *Experimental Mechanics*, 29(3):261–267, sep 1989. ISSN 0014-4851. doi: 10.1007/BF02321405. URL http://link.springer.com/10.1007/BF02321405.

[61] Bing Pan, Kemao Qian, Huimin Xie, and Anand Asundi. Two-dimensional digital image correlation for in-plane displacement and strain measurement: a review. *Measurement Science and Technology*, 20 (6):062001, jun 2009. ISSN 0957-0233. doi: 10.1088/0957-0233/20/6/062001. URL http://stacks.iop.org/0957-0233/20/i=6/a=062001?key=crossref.37cf26a6947e54eb5498e67742a4e2ad.

[62] J. C. Wyant. Double Frequency Grating Lateral Shear Interferometer. *Applied Optics*, 12(9):2057, sep 1973. ISSN 0003-6935. doi: 10.1364/AO.12.

002057. URL https://www.osapublishing.org/abstract.cfm?URI=ao-12-9-2057.

[63] F. P. Chiang and A. Asundi. White light speckle method of experimental strain analysis. *Applied Optics*, 18(4):409, feb 1979. ISSN 0003-6935. doi: 10.1364/AO.18.000409. URL https://www.osapublishing.org/abstract.cfm?URI=ao-18-4-409.

[64] MA Sutton, WJ Wolters, WH Peters, WF Ranson, and SR McNeill. Determination of displacements using an improved digital correlation method. *Image and Vision Computing*, 1(3):133–139, aug 1983. ISSN 02628856. doi: 10.1016/0262-8856(83)90064-1. URL http://linkinghub.elsevier.com/retrieve/pii/0262885683900641.

[65] Sven Bossuyt. Optimized Patterns for Digital Image Correlation. pages 239–248. Springer, New York, NY, 2013. doi: 10.1007/978-1-4614-4235-6_34. URL http://link.springer.com/10.1007/978-1-4614-4235-6{_}34.

[66] G.F. Bomarito, J.D. Hochhalter, T.J. Ruggles, and A.H. Cannon. Increasing accuracy and precision of digital image correlation through pattern optimization. *Optics and Lasers in Engineering*, 91:73–85, apr 2017. ISSN 01438166. doi: 10.1016/j.optlaseng.2016.11.005. URL http://linkinghub.elsevier.com/retrieve/pii/S0143816616304110.

[67] M. Grédiac, F. Sur, and B. Blaysat. The Grid Method for In-plane Displacement and Strain Measurement: A Review and Analysis. *Strain*, 52(3):205–243, jun 2016. ISSN 00392103. doi: 10.1111/str.12182. URL http://doi.wiley.com/10.1111/str.12182.

[68] J Tracy, A Waas, and S Daly. Experimental assessment of toughness in ceramic matrix composites using the j-integral with digital image correlation part i: methodology and validation. *Journal of Materials Science*, 50(13): 4646–4658, 2015.

[69] Vincent J. Parks. The grid method. *Experimental Mechanics*, 9(7):27–33, jul 1969. ISSN 0014-4851. doi: 10.1007/BF02325141. URL http://link.springer.com/10.1007/BF02325141.

[70] Vincent J. Parks. Strain Measurement Using Grids. *Optical Engineering*, 21(4):633–639, aug 1982. ISSN 0091-3286. doi: 10.1117/12.7972958. URL http://opticalengineering.spiedigitallibrary.org/article.aspx?doi=10.1117/12.7972958.

[71] R Sowerby, E Chu, and J L Duncan. Determination of large strains in metalforming. *The Journal of Strain Analysis for Engineering Design*, 17(2): 95–101, apr 1982. ISSN 0309-3247. doi: 10.1243/03093247V172095. URL http://journals.sagepub.com/doi/10.1243/03093247V172095.

[72] D. W. Manthey and D. Lee. Recent developments in a vision-based surface strain measurement system. *JOM*, 47(7):46–49, jul 1995. ISSN 1047-4838. doi: 10.1007/BF03221231. URL http://link.springer.com/10.1007/BF03221231.

[73] Y. Morimoto, Y. Seguchi, and T. Higashi. Strain analysis by mismatch moire method and grid method using Fourier transform. *Computational Mechanics*, 6(1):1–10, 1990. ISSN 0178-7675. doi: 10.1007/BF00373795. URL http://link.springer.com/10.1007/BF00373795.

[74] Shengnan Sun, Michel Grédiac, Evelyne Toussaint, Jean-Denis Mathias, and Narimane Mati-Baouche. Applying a Full-Field Measurement Technique to Characterize the Mechanical Response of a Sunflower-Based Biocomposite. *Experimental Mechanics*, 55(5):917–934, jun 2015. ISSN 0014-4851. doi: 10.1007/s11340-015-9988-1. URL http://link.springer.com/10.1007/s11340-015-9988-1.

[75] M.J. Hÿtch, E. Snoeck, and R. Kilaas. Quantitative measurement of displacement and strain fields from HREM micrographs. *Ultramicroscopy*, 74 (3):131–146, aug 1998. ISSN 03043991. doi: 10.1016/S0304-3991(98)00035-7. URL http://linkinghub.elsevier.com/retrieve/pii/S0304399198000357.

[76] M.J. Hÿtch and T. Plamann. Imaging conditions for reliable measurement of displacement and strain in high-resolution electron microscopy. *Ultramicroscopy*, 87(4):199–212, may 2001. ISSN 03043991. doi: 10.1016/S0304-3991(00)00099-1. URL http://linkinghub.elsevier.com/retrieve/pii/S0304399100000991.

[77] Huimin Xie, Satoshi Kishimoto, Anand Asundi, Chai Gin Boay, Norio Shinya, Jin Yu, and Bryan K A Ngoi. In-plane deformation measurement using the atomic force microscope moiré method. *Nanotechnology*, 11 (1):24–29, mar 2000. ISSN 0957-4484. doi: 10.1088/0957-4484/11/1/305. URL http://stacks.iop.org/0957-4484/11/i=1/a=305?key=crossref.3625f95a7f67d2849060d7451d6024fe.

[78] Huimin Xie, Zhanwei Liu, Daining Fang, Fulong Dai, Hongjun Gao, and Yapu Zhao. A study on the digital nano-moiré method and its phase shifting technique. *Measurement Science and Technology*, 15(9):1716–1721, sep 2004. ISSN 0957-0233. doi: 10.1088/0957-0233/15/9/007. URL http://stacks.iop.org/0957-0233/15/i=9/a=007?key=crossref.e2b1ff934d20c903ad76a862dc315266.

[79] J.-L. Piro and M. Grediac. PRODUCING AND TRANSFERRING LOW-SPATIAL-FREQUENCY GRIDS FOR MEASURING DISPLACEMENT FIELDS WITH MOIRE AND GRID METHODS. *Experimental Techniques*, 28(4):23–26, jul 2004. ISSN 0732-8818. doi: 10.1111/j.1747-1567.2004.

tb00173.x. URL http://doi.wiley.com/10.1111/j.1747-1567.2004.tb00173.x.

[80] Rostand Moutou Pitti, Claudiu Badulescu, and Michel Grédiac. Characterization of a cracked specimen with full-field measurements: direct determination of the crack tip and energy release rate calculation. *International Journal of Fracture*, 187(1):109–121, may 2014. ISSN 0376-9429. doi: 10.1007/s10704-013-9921-5. URL http://link.springer.com/10.1007/s10704-013-9921-5.

[81] B Ribbens. Development and validation of a time-domain fringe pattern analysis technique for the measurement of object shape and deformation. *PhD Thesis, Vrije Universistat Brussel and Universitat Antwerpen*, 2015.

[82] Lorna J Gibson and Michael F Ashby. *Cellular Solids: Structure and Properties - Lorna J. Gibson, Michael F. Ashby - Google Books*. Cambridge University Press, 2 edition, 1997. ISBN 0 521 49911 9. URL https://books.google.com/books?hl=en{\&}lr={\&}id=rzVIBAAAQBAJ{\&}oi=fnd{\&}pg=PR7{\&}dq=gibson+ashby+cellular+solids+structure+and+properties+citation{\&}ots=gw5x9{_}7xBU{\&}sig=JBe66HXSx7{_}2pEbPAvsWC6rE0Fw{\#}v=onepage{\&}q{\&}f=false.

[83] Baikowski. Baikowski Malakoff HP DPM. http://www.baikowski.com/products, 2017. [Online; accessed 10-June-2017].

[84] G.P. Cherepanov. Crack propagation in continuous media: PMM vol. 31, no. 3, 1967, pp. 476–488. *Journal of Applied Mathematics and Mechanics*, 31(3):503–512, jan 1967. ISSN 0021-8928. doi: 10.1016/0021-8928(67)90034-2. URL https://www.sciencedirect.com/science/article/pii/0021892867900342.

[85] O. Chiantore, L. Trossarelli, and M. Lazzari. Photooxidative degradation of acrylic and methacrylic polymers. *Polymer*, 41(5):1657–1668, mar 2000. ISSN 00323861. doi: 10.1016/S0032-3861(99)00349-3. URL http://linkinghub.elsevier.com/retrieve/pii/S0032386199003493.

[86] Satish Balay, William D. Gropp, Lois Curfman McInnes, and Barry F. Smith. Efficient Management of Parallelism in Object-Oriented Numerical Software Libraries. In *Modern Software Tools for Scientific Computing*, pages 163–202. Birkhäuser Boston, Boston, MA, 1997. doi: 10.1007/978-1-4612-1986-6_8. URL http://link.springer.com/10.1007/978-1-4612-1986-6{_}8.

[87] S. Balay, S. Abhyankar, M. Adams, J. Brown, P. Brune, K. Buschelman, L. D. Dalcin, V. Eijkhout, W. Gropp, D. Kaushik, M. Knepley, D. May, L. Curfman McInnes, T. Munson, K. Rupp, P. Sanan, B. Smith, S. Zampini, H. Zhang, and H. Zhang. PETSc Users Manual Revision 3.8. Technical report, Argonne

National Laboratory (ANL), Argonne, IL (United States), sep 2013. URL http://www.osti.gov/servlets/purl/1409218/.

[88] S. Balay, J. Brown, K. Buschelman, W.D. Gropp, D. Kaushik, M. Knepley, L.C. McInnes, B. Smith, and H. Zhang. PETSc/Tao: Home Page, 2013. URL https://www.mcs.anl.gov/petsc/.

[89] J. W. Obreimoff. The Splitting Strength of Mica. *Proceedings of the Royal Society of London A*, 25:290–297, 1930. ISSN 1364-5021. doi: 10.1098/rspa.1933.0074.

[90] Lawn B. R. Roach, D. H., Hueckeroth, D. M. Crack Velocity Thresholds and Healing in Mica. *Journal of Colloid and Interface Science*, 114(1):292–294, 1986.

[91] Kai-tak Wan, Nicholas Aimard, S Lathabai, Roger G Horn, and Brian R. Lawn. Interfacial energy states of moisture-exposed cracks in mica. *Journal of Materials Research*, 5(1):172–182, 1990. ISSN 08842914. doi: 10.1557/JMR.1990.0172.

[92] Kai-Tak Wan, Douglas T. Smith, and Brain R. Lawn. Fracture and Contact Adhesion Energies of Mica-Mica, Silica-Silica, and Mica-Silica Interfaces in Dry and Moist Atmospheres. *Journal of the American Ceramic Society*, 75 (3):667–676, mar 1992. ISSN 0002-7820. doi: 10.1111/j.1151-2916.1992.tb07857.x. URL http://doi.wiley.com/10.1111/j.1151-2916.1992.tb07857.x.

[93] Hiroshi Okusa, Kazue Kurihara, and Toyoki Kunitake. Chemical Modification of Molecularly Smooth Mica Surface and Protein Attachment. Technical report, 1994. URL https://pubs.acs.org/sharingguidelines.

[94] Hong Yang, Alex Kuperman, Neil Coombs, Suzan Mamiche-Afara, and Geoffrey A. Ozin. Synthesis of oriented films of mesoporous silica on mica. *Nature*, 379(6567):703–705, feb 1996. ISSN 0028-0836. doi: 10.1038/379703a0. URL http://www.nature.com/articles/379703a0.

[95] Rivlin R. S. The Effective work of adhesion Experiments with Adhesive Tape. *Paint Technology*, IX(106):2611–2614, 1944.

[96] K Kendall. Thin-film peeling-the elastic term. *Journal of Physics D: Applied Physics*, 8(13):1449–1452, sep 1975. ISSN 0022-3727. doi: 10.1088/0022-3727/8/13/005. URL http://stacks.iop.org/0022-3727/8/i=13/a=005?key=crossref.1fe0609b9b564ad02f86ea972699bc29.

[97] S. Xia, L. Ponson, G. Ravichandran, and K. Bhattacharya. Toughening and Asymmetry in Peeling of Heterogeneous Adhesives. *Physical Review Letters*, 108(19):1–5, may 2012. ISSN 0031-9007. doi: 10.1103/PhysRevLett.108.196101. URL https://link.aps.org/doi/10.1103/PhysRevLett.108.196101.

[98] S.M. Xia, L. Ponson, G. Ravichandran, and K. Bhattacharya. Adhesion of heterogeneous thin films—I: Elastic heterogeneity. *Journal of the Mechanics and Physics of Solids*, 61(3):838–851, mar 2013. ISSN 0022-5096. doi: 10.1016/J.JMPS.2012.10.014. URL https://www.sciencedirect.com/science/article/pii/S0022509612002359.

[99] S.M. Xia, L. Ponson, G. Ravichandran, and K. Bhattacharya. Adhesion of heterogeneous thin films II: Adhesive heterogeneity. *Journal of the Mechanics and Physics of Solids*, 83:88–103, oct 2015. ISSN 0022-5096. doi: 10.1016/J.JMPS.2015.06.010. URL https://www.sciencedirect.com/science/article/pii/S0022509615001593.

[100] A Majumder, S Mondal, A K Tiwari, A Ghatak, and A Sharma. Direction specific adhesion induced by subsurface liquid filled microchannels. *Soft Matter*, 8(27):7228–7233, 2012. ISSN 1744683X (ISSN). doi: 10.1039/c2sm25507c. URL http://www.scopus.com/inward/record.url?eid=2-s2.0-84869594034{\&}partnerID=40{\&}md5=ff1ba1eafe4330c24c1a2f4598ac51d8.

[101] Animangsu Ghatak. Peeling off an adhesive layer with spatially varying topography and shear modulus. *Physical Review E - Statistical, Nonlinear, and Soft Matter Physics*, 89(3):1–6, 2014. ISSN 15502376. doi: 10.1103/PhysRevE.89.032407.

[102] J. Gonzalez and J. Lambros. Crack Path Selection in Microstructurally Tailored Inhomogeneous Polymers. *Experimental Mechanics*, 53(4):619–634, apr 2013. ISSN 0014-4851. doi: 10.1007/s11340-012-9668-3. URL http://link.springer.com/10.1007/s11340-012-9668-3.

[103] C. Kovalchick, A. Molinari, and G. Ravichandran. An experimental investigation of the stability of peeling for adhesive tapes. *Mechanics of Materials*, 66:69–78, nov 2013. ISSN 0167-6636. doi: 10.1016/J.MECHMAT.2013.07.012. URL https://www.sciencedirect.com/science/article/pii/S0167663613001415.

[104] J. G. Williams. Friction and plasticity effects in wedge splitting and cutting fracture tests. *Journal of Materials Science*, 33(22):5351–5357, November 1998. ISSN 1573-4803. doi: 10.1023/A:1004490015211. URL https://doi.org/10.1023/A:1004490015211.

[105] Brian R. Lawn. Indentation of Ceramics with Spheres: A Century after Hertz. *Journal of the American Ceramic Society*, 81(8):1977–1994, jan 1998. ISSN 00027820. doi: 10.1111/j.1151-2916.1998.tb02580.x. URL http://doi.wiley.com/10.1111/j.1151-2916.1998.tb02580.x.

[106] Haiyan Liu, Brian R. Lawn, and Stephen M. Hsu. Hertzian Contact Response of Tailored Silicon Nitride Multilayers. *Journal of the American Ceramic Society*, 79(4):1009–1014, apr 1996. ISSN 0002-7820. doi: 10.1111/j.1151-

2916.1996.tb08540.x. URL http://doi.wiley.com/10.1111/j.1151-2916.1996.tb08540.x.

[107] Antonia Pajares, Lanhua Wei, Brian R. Lawn, and Christopher C. Berndt. Contact Damage in Plasma-Sprayed Alumina-Based Coatings. *Journal of the American Ceramic Society*, 79(7):1907–1914, jul 1996. ISSN 0002-7820. doi: 10.1111/j.1151-2916.1996.tb08012.x. URL http://doi.wiley.com/10.1111/j.1151-2916.1996.tb08012.x.

[108] Antonia Pajares, Lanhua Wei, Brian R. Lawn, Nitin P. Padture, and Christopher C. Berndt. Mechanical characterization of plasma sprayed ceramic coatings on metal substrates by contact testing. *Materials Science and Engineering: A*, 208(2):158–165, apr 1996. ISSN 0921-5093. doi: 10.1016/0921-5093(95)10071-7. URL https://www.sciencedirect.com/science/article/pii/0921509395100717.

[109] A C Fischer-Cripps, B R Lawn, A Pajares, and L Wei. Stress Analysis of Elastic-Plastic Contact Damage in Ceramic Coatings on Metal Substrates. *Journal of the American Ceramic Society*, 79(10):2619–2625, aug 1996. ISSN 00027820. doi: 10.1111/j.1151-2916.1996.tb09024.x. URL http://dx.doi.org/10.1111/j.1151-2916.1996.tb09024.x.

[110] Linan An, Helen M. Chan, Nitin P. Padture, and Brian R. Lawn. Damage-resistant alumina-based layer composites. *Journal of Materials Research*, 11(01):204–210, jan 1996. ISSN 0884-2914. doi: 10.1557/JMR.1996.0025. URL http://www.journals.cambridge.org/abstract{_}S0884291400022214.

[111] Donald M. Baskin, Michael H. Zimmerman, K. T. Faber, and Edwin R. Fuller. Forming Single-Phase Laminates via the Gelcasting Technique. *Journal of the American Ceramic Society*, 80(11):2929–2932, nov 1997. ISSN 0002-7820. doi: 10.1111/j.1151-2916.1997.tb03213.x. URL http://doi.wiley.com/10.1111/j.1151-2916.1997.tb03213.x.

[112] Sataporn Wuttiphan, Antonia Pajares, Brian R. Lawn, and Christopher C. Berndt. Effect of substrate and bond coat on contact damage in zirconia-based plasma-sprayed coatings. *Thin Solid Films*, 293(1-2):251–260, jan 1997. ISSN 0040-6090. doi: 10.1016/S0040-6090(96)08992-4. URL https://www.sciencedirect.com/science/article/pii/S0040609096089924.

[113] John K. Montgomery and K. T. Faber. Processing and Surface Flaw Tolerance of Alumina Bilayers. *Journal of the American Ceramic Society*, 88(2):287–292, feb 2005. ISSN 0002-7820. doi: 10.1111/j.1551-2916.2005.00073.x. URL http://doi.wiley.com/10.1111/j.1551-2916.2005.00073.x.

[114] Sataporn Wuttiphan, Brian R. Lawn, and Nitin P. Padture. Crack Suppression in Strongly Bonded Homogeneous/Heterogeneous Laminates: A Study on Glass/Glass-Ceramic Bilayers. *Journal of the American Ceramic Society*, 79

(3):634–640, apr 1996. ISSN 00027820. doi: 10.1111/j.1151-2916.1996.tb07922.x. URL http://doi.wiley.com/10.1111/j.1151-2916.1996.tb07922.x.

[115] Johanna Schmidt and Paolo Colombo. Digital light processing of ceramic components from polysiloxanes. *Journal of the European Ceramic Society*, 38(1):57–66, jan 2018. ISSN 0955-2219. doi: 10.1016/J.JEURCERAMSOC.2017.07.033.

[116] Paolo Colombo, Johanna Schmidt, Giorgia Franchin, Andrea Zocca, and Jens Günster. Additive manufacturing techniques for fabricating complex ceramic components from preceramic polymers. *American Ceramic Society Bulletin*, pages 16–24, 2017.

[117] Zak C Eckel, Chaoyin Zhou, John H Martin, Alan J Jacobsen, William B Carter, and Tobias A Schaedler. Additive manufacturing of polymer-derived ceramics. *Science (New York, N.Y.)*, 351(6268):58–62, jan 2016. ISSN 1095-9203. doi: 10.1126/science.aad2688.

[118] Y. de Hazan and D. Penner. SiC and SiOC ceramic articles produced by stereolithography of acrylate modified polycarbosilane systems. *Journal of the European Ceramic Society*, 37(16):5205–5212, dec 2017. ISSN 0955-2219. doi: 10.1016/J.JEURCERAMSOC.2017.03.021.

[119] Erika Zanchetta, Marco Cattaldo, Giorgia Franchin, Martin Schwentenwein, Johannes Homa, Giovanna Brusatin, and Paolo Colombo. Stereolithography of SiOC Ceramic Microcomponents. *Advanced Materials*, 28(2):370–376, jan 2016. ISSN 09359648. doi: 10.1002/adma.201503470.

[120] T.-A. Pham, D.-P. Kim, T.-W. Lim, S.-H. Park, D.-Y. Yang, and K.-S. Lee. Three-Dimensional SiCN Ceramic Microstructures via Nano-Stereolithography of Inorganic Polymer Photoresists. *Advanced Functional Materials*, 16(9):1235–1241, jun 2006. ISSN 1616-301X. doi: 10.1002/adfm.200600009. URL http://doi.wiley.com/10.1002/adfm.200600009.

[121] Andrea Zocca, Cynthia M. Gomes, Andreas Staude, Enrico Bernardo, Jens Günster, and Paolo Colombo. SiOC ceramics with ordered porosity by 3D-printing of a preceramic polymer. *Journal of Materials Research*, 28(17):2243–2252, sep 2013. ISSN 0884-2914. doi: 10.1557/jmr.2013.129. URL https://www.cambridge.org/core/product/identifier/S0884291413001295/type/journal{_}article.

[122] Laura Brigo, Johanna Eva Maria Schmidt, Alessandro Gandin, Niccolò Michieli, Paolo Colombo, and Giovanna Brusatin. 3D Nanofabrication of SiOC Ceramic Structures. *Advanced Science*, 5(12):1800937, dec 2018. ISSN 21983844. doi: 10.1002/advs.201800937. URL http://doi.wiley.com/10.1002/advs.201800937.

[123] Xifan Wang, Franziska Schmidt, Dorian Hanaor, Paul H. Kamm, Shuang Li, and Aleksander Gurlo. Additive manufacturing of ceramics from preceramic polymers: A versatile stereolithographic approach assisted by thiol-ene click chemistry. *Additive Manufacturing*, 27:80–90, may 2019. ISSN 2214-8604. doi: 10.1016/J.ADDMA.2019.02.012. URL https://www.sciencedirect.com/science/article/pii/S2214860418310479.

[124] Giorgia Franchin, Halide Maden, Larissa Wahl, Andrea Baliello, Marco Pasetto, Paolo Colombo, Giorgia Franchin, Halide Selin Maden, Larissa Wahl, Andrea Baliello, Marco Pasetto, and Paolo Colombo. Optimization and Characterization of Preceramic Inks for Direct Ink Writing of Ceramic Matrix Composite Structures. *Materials*, 11(4):515, mar 2018. ISSN 1996-1944. doi: 10.3390/ma11040515. URL http://www.mdpi.com/1996-1944/11/4/515.

[125] Andrea Zocca, Giorgia Franchin, Hamada Elsayed, Emilia Gioffredi, Enrico Bernardo, and Paolo Colombo. Direct Ink Writing of a Preceramic Polymer and Fillers to Produce Hardystonite ($Ca_2ZnSi_2O_7$) Bioceramic Scaffolds. *Journal of the American Ceramic Society*, 99(6):1960–1967, jun 2016. ISSN 00027820. doi: 10.1111/jace.14213. URL http://doi.wiley.com/10.1111/jace.14213.

[126] Giovanni Pierin, Chiara Grotta, Paolo Colombo, and Cecilia Mattevi. Direct Ink Writing of micrometric SiOC ceramic structures using a preceramic polymer. *Journal of the European Ceramic Society*, 36(7):1589–1594, jun 2016. ISSN 0955-2219. doi: 10.1016/J.JEURCERAMSOC.2016.01.047. URL https://www.sciencedirect.com/science/article/abs/pii/S0955221916300474.

[127] A Zocca, H Elsayed, E Bernardo, C M Gomes, M A Lopez-Heredia, C Knabe, P Colombo, and J Günster. 3D-printed silicate porous bioceramics using a non-sacrificial preceramic polymer binder. *Biofabrication*, 7(2):025008, may 2015. ISSN 1758-5090. doi: 10.1088/1758-5090/7/2/025008. URL http://stacks.iop.org/1758-5090/7/i=2/a=025008?key=crossref.ad6c583046cb0f2af81ab1c2c8b34a48.

[128] Tiemo Bückmann, Nicolas Stenger, Muamer Kadic, Johannes Kaschke, Andreas Frölich, Tobias Kennerknecht, Christoph Eberl, Michael Thiel, and Martin Wegener. Tailored 3D mechanical metamaterials made by dip-in direct-laser-writing optical lithography. *Advanced Materials*, 24(20):2710–2714, 2012. ISSN 09359648. doi: 10.1002/adma.201200584.

[129] Julian Panetta, Qingnan Zhou, Luigi Malomo, Nico Pietroni, Paolo Cignoni, and Denis Zorin. Elastic textures for additive fabrication. *ACM Transactions on Graphics*, 34(4):1–12, jul 2015. ISSN 07300301. doi: 10.1145/2766937. URL http://dl.acm.org/citation.cfm?doid=2809654.2766937.

[130] Caroline A Schneider, Wayne S Rasband, and Kevin W Eliceiri. NIH Image to ImageJ: 25 years of image analysis. *Nature Methods*, 9(7):671–675, jul 2012. ISSN 1548-7091. doi: 10.1038/nmeth.2089. URL http://www.nature.com/articles/nmeth.2089.

[131] Rasto Brezny, David J. Green, and Chuong Quang Dam. Evaluation of Strut Strength in Open-Cell Ceramics. *Journal of the American Ceramic Society*, 72(6):885–889, jun 1989. ISSN 0002-7820. doi: 10.1111/j.1151-2916.1989.tb06239.x.

[132] ASTM C1684 - 18, Standard Test Method for Flexural Strength of Advanced Ceramics at Ambient Temperature Cylindrical Rod Strength, 2018.

[133] G. M. Pharr. An improved technique for determining hardness and elastic modulus using load and displacement sensing indentation experiments. *Journal of Materials Research*, 7(6):1564–1583, 1992. ISSN 20445326. doi: 10.1557/JMR.1992.1564.

[134] H.X. Zhu, J.F. Knott, and N.J. Mills. Analysis of the elastic properties of open-cell foams with tetrakaidecahedral cells. *Journal of the Mechanics and Physics of Solids*, 45(3):319–343, mar 1997. ISSN 0022-5096. doi: 10.1016/S0022-5096(96)00090-7.

[135] V.S. Deshpande, N.A. Fleck, and M.F. Ashby. Effective properties of the octet-truss lattice material. *Journal of the Mechanics and Physics of Solids*, 49(8):1747–1769, aug 2001. ISSN 0022-5096.

[136] Lorna J Gibson and Michael F Ashby. *Cellular Solids: Structure and Properties - Lorna J. Gibson, Michael F. Ashby - Google Books*. Cambridge University Press, 2 edition, 1997. ISBN 0 521 49911 9.

[137] Paolo Colombo, John R. Hellmann, and David L. Shelleman. Thermal Shock Behavior of Silicon Oxycarbide Foams. *Journal of the American Ceramic Society*, 85(9):2306–2312, sep 2002. ISSN 0002-7820. doi: 10.1111/j.1151-2916.2002.tb00452.x.

[138] Cekdar Vakifahmetoglu, Paolo Colombo, Alberto Pauletti, Cristina Fernandez Martin, and Florence Babonneau. SiOC Ceramic Monoliths with Hierarchical Porosity. *International Journal of Applied Ceramic Technology*, 7(4):528–535, mar 2009. ISSN 1546542X. doi: 10.1111/j.1744-7402.2009.02365.x. URL http://doi.wiley.com/10.1111/j.1744-7402.2009.02365.x.

[139] Noriaki Arai and Katherine T. Faber. Hierarchical porous ceramics via two-stage freeze casting of preceramic polymers. *Scripta Materialia*, 162:72–76, mar 2019. ISSN 1359-6462. doi: 10.1016/J.SCRIPTAMAT.2018.10.037. URL https://www.sciencedirect.com/science/article/pii/S1359646218306663.

[140] J. B. Wachtman, W. Roger. Cannon, and M. John. Matthewson. *Mechanical properties of ceramics*. Wiley, 2009. ISBN 9780470451502. URL https://www.wiley.com/en-us/Mechanical+Properties+of+Ceramics{\%}2C+2nd+Edition-p-9780470451502.

[141] Carlos M. Portela, Julia R. Greer, and Dennis M. Kochmann. Impact of node geometry on the effective stiffness of non-slender three-dimensional truss lattice architectures. *Extreme Mechanics Letters*, 22:138–148, jul 2018. ISSN 2352-4316. doi: 10.1016/J.EML.2018.06.004. URL https://www.sciencedirect.com/science/article/pii/S2352431618300725.

[142] N. A. Fleck, V. S. Deshpande, and M. F. Ashby. Micro-architectured materials: past, present and future. *Proceedings of the Royal Society A: Mathematical, Physical and Engineering Sciences*, 466(2121):2495–2516, sep 2010. ISSN 1364-5021. doi: 10.1098/rspa.2010.0215. URL http://www.royalsocietypublishing.org/doi/10.1098/rspa.2010.0215.

[143] Johan Christensen, Muamer Kadic, Oliver Kraft, and Martin Wegener. Vibrant times for mechanical metamaterials. *MRS Communications*, 5(03):453–462, sep 2015. ISSN 2159-6859. doi: 10.1557/mrc.2015.51. URL http://www.journals.cambridge.org/abstract{_}S2159685915000518.

[144] T A Schaedler, A J Jacobsen, A Torrents, A E Sorensen, J Lian, J R Greer, L Valdevit, and W B Carter. Ultralight metallic microlattices. *Science (New York, N.Y.)*, 334(6058):962–965, nov 2011. ISSN 1095-9203. doi: 10.1126/science.1211649. URL http://www.ncbi.nlm.nih.gov/pubmed/22096194.

[145] C. Janssen. Specimen for fracture mechanics studies on glass. *Proceedings of the 10th International Congress On Glass*, pages 10.23–10.30, 1974.

[146] M. Y. He, M. R. Turner, and A. G. Evans. Analysis of the double cleavage drilled compression specimen for interface fracture energy measurements over a range of mode mixities. *Acta Metallurgica Et Materialia*, 43(9):3453–3458, 1995. ISSN 09567151. doi: 10.1016/0956-7151(95)00036-U.